POLARIZATION-SENSITIVE OPTICAL COHERENCE TOMOGRAPHY USING POLARIZATION-MAINTAINING FIBERS

A dissertation submitted to the Faculty of the Graduate School of the
UNIVERSITY OF MINNESOTA
by

MUHAMMAD K. AL-QAISI

in partial fulfillment of the requirements for the degree of
DOCTOR OF PHILOSOPHY

Adviser: Taner Akkin

December 2010

December 2010

بسم الله الرحمن الرحيم

ACKNOWLEDGEMENTS

I want to start by thanking my adviser Prof. Taner Akkin for his valuable guidance. Working in his lab was an insightful experience, from which I learned a lot. I started with Prof. Akkin in the early stages of the lab, and I am delighted to see the progress that we have collectively accomplished. In every event I choose to thank Prof. James Leger, a distinguished researcher with outstanding teaching skills; thanks Dr. Leger for being always helpful, and for reading my dissertation. I appreciate Prof. Robert Tranquillo's service on my committee, and his dedication heading the department; I will always remember the department's summer parties in your backyard! Thanks to Prof. Shai Ashkenazi for the interesting ultrasound class, and for being a reader of my thesis and a committee member on my final defense.

I want to thank my labmates: John Becker, Aarthi Sivaprakasm, Hui Wang and Adam Black; I wish every one of you the best in his/her endeavors. The discussions I had with you have helped me improving the content of this dissertation, and elevating the level of my understanding of the topic. I want to also thank Prof. Victor Barocas and his lab members: Rouzbeh Amini, Julie Whitecomb, and Sara Jouzdani; collaborating with you was fun and indeed productive. Thanks for the good neighbors and the caffeine suppliers, thanks to everyone in Lori's coffee. I must thank Mahmoud Shahin for the valuable advice he always offered, and my writing comrade, Omar Tesdell, for the good times at Saint Paul library and for reading this manuscript and commenting on it.

I strongly appreciate the scholarship from the Jordan University of Science and Technology. Without their support, I may not have been able to come to Minnesota. I would also like to acknowledge the National Institute of Health for supporting this research, and the Graduate School at the University of Minnesota for supporting me in the last semester at the university through the Doctoral Dissertation Fellowship.

I must thank my parents and siblings for their constant support and availability to help; the good environment they created is always cherished. Thank you father and mother for, well, everything! I learned from you patience and dedication; and I promise to grasp onto the values you exemplified. I can not express my appreciation to my wife's support; thanks Mysoon for being always the best despite the long days I have spent away working on this manuscript, and thanks for always understanding and endorsing me. It is now your turn to come back to school, Mysoon! And you, little Khaled, you may not yet understand, but I must thank you for the pleasure your smiles has brought to my heart!

DEDICATION

ABSTRACT

Optical Coherence Tomography (OCT) is a sensitive imaging technique that generates cross-sectional images of turbid tissues with a micrometer-scale resolution. Polarization-Sensitive (PS) OCT adds additional contrast to OCT by detecting polarization alterations within tissues, and provides accurate OCT images in polarization-altering tissues. Common approaches to build PSOCT are either: simple but difficult to incorporate in clinics and laboratories, or fiber-based and flexible but expensive, sophisticated, and computationally demanding.

We have developed a new approach to build PSOCT using Polarization-Maintaining Fibers (PMF). A single depth scan is sufficient to calculate reflectivity, retardance, and axis orientation information using computationally-inexpensive algorithms. We present novel PMF-based PSOCT systems and demonstrate sensitivity figures larger than 100 dB, equivalent to common approaches. The developed PMF-based interferometers are used to measure minute Faraday rotations in tissue-mimicking phantoms, and the polarization properties of unmyelinated nerves. A novel algorithm is also developed to correct for errors calculating the birefringence of samples, and generate interpretable PSOCT images.

TABLE OF CONTENTS

LIST OF FIGURES

LIST OF ABBREVIATIONS

AP	Action potential
$B\mathbf{d}$	The product of the magnetic field component parallel to the axis of light propagation by the magneto-optical interaction path length
C	Collimator
EOM	Electro-optic modulator
FD	Fourier domain
FSI	Free-space isolator
FWHM	Full-width at half-maximum
GM	Glavanometer-mounted mirror
L	Lens
LCI	Low-Coherence Interferometry
M	Mirror
OCT	Optical coherence tomography
OFDI	Optical frequency domain imaging
PD	Photodetector
PM	Polarization-maintaining
PMF	Polarization-maintaining fibers
PSC	Polarization splitter/combiner
PSOCT	Polarization-sensitive OCT
QWP	Quarter-wave plate

RSOD	Rapid scanning optical delay
SD	Spectral domain
SLD	Super-luminescent diode
SMF	Single-mode fiber (non-PMF)
SNR	Signal to noise ratio
SS	Swept source
TD	Time domain
VR	Variable retarder

NOTATIONS

$\hat{\theta}$	Relative optical axis orientation
σ_θ	Standard deviation of the phase noise
A	Attenuation in the reference arm
B	Magnetic field component parallel to the axis of light propagation
$C_{L,}\, C_R$	Left and right circular polarization states
d	The magneto-optical interaction path length
d	The depth index within the sample
Ɗ	Depth of the birefringent cube
d_g	Displacement between a ghost line and a main line
d_{max}	Imaging range in SS OCT
$E(t)$	Electric field of a low-coherence light wave
E_{in}	Jones vector of light transmitted into the interferometer
E_r	Jones vector of light reflected from the reference arm
E_s	Jones vector of light reflected from the sample arm
E_x, E_y	The components of the electric field of light propagating in the z direction
f	Modulation frequency of the coherence function in TD OCT
$\mathcal{F}$	Fourier transform operator
h	Lateral displacement of the birefringent wedge
$\mathcal{H}$	Hilbert transform operator
I_d	Light intensity detected on the output of the interferometer

I_{DC}	Proportionality constant of the interference term in I_d
I_i	The interference term in I_d
I_r, I_s	DC components from the reference and sample in I_d
I_s, I_f	Coherence functions on the slow and fast channels of the PMF of the detection arm in PSOCT
I_{ss}, I_{ff}	Interference patterns detected on the original channels of the PSLCI
I_{xs}, I_{xf}	Interference patterns detected on the cross-coupled channels of the PSLCI
J	Jones matrix of a retarder
k_r	the split ratio of the beam splitter into the reference arm
l	Displacement between the coherence functions of PMF-based TD PSOCT
L	Linear polarization state parallel to x
L_B	Beat length of PMF
l_{PMF}	The length of the PMF in the sample (or reference) arm
L_Θ	Linear polarization state rotated by Θ with respect to x
n	Refractive index
n_{ex}	Source's excess noise
n_{sh}	Shot noise
n_T	Detector's thermal noise
P_r	Light power coupled from the reference arm into the coupler
R	Reflectivity of the sample
$\mathbb{R}$	Rotation matrix
$S(v)$	Power spectral density of a light source
t	Time index
U_s, U_f	The amplitudes of I_s, I_f

V	Verdet constant
w	The cut angle of the birefringent wedges
α	A constant related to the coherence length of the light source
$\gamma(\tau)$	The complex degree of coherence of the light source
δ	Retardance
$\boldsymbol{\delta}$	Retardance of a linear retarder
$\Delta I/I$	Relative light intensity change in crossed-polarizers setups
Δn	The difference in the refractive index of a birefringent medium
δ_{xs}, δ_{xf}	Single pass phase delays in nanometers
$\Delta\delta$	Retardance change
$\Delta\lambda$	FWHM bandwidth of a broadband light source
Δv	Frequency bandwidth of a broadband light source
$\Delta\varphi$	The phase difference between E_x and E_y
θ	Optical axis orientation
$\boldsymbol{\theta}$	Axis orientation of a linear retarder
Θ	Faraday rotation angle
λ_o	Central wavelength of a broadband light source
v_o	Central frequency of a broadband light source
ρ_a	OCT axial resolution
τ	The time delay between the sample and reference arms
φ	The phase of the interference I_i
φ_o	Arbitrary phase bias between I_s, I_f
φ_s, φ_f	The arguments of I_s, I_f
φ_{xs}, φ_{xf}	Arguments of I_{xs}, I_{xf}

CHAPTER 1
INTRODUCTION

1.1 MOTIVATION

Optical systems are unique because light exhibits various measureable properties, such as intensity and polarization. The applications of optical imaging and detection methods span almost every field of study. In biology, however, there is an essential need to image deeper layers of tissues. Conventional optical imaging techniques are limited to surface imaging, such as in endoscopy, or imaging of thin fixed samples, as in transmission microscopy. Detection of photons scattered from within nontransparent tissues is possible using Optical Coherence Tomography (OCT), a low-coherence interferometry (LCI) technique.

Light polarization describes the orientation of the field of a light wave along its propagation axis. Polarization measurements have been employed to study materials with heterogeneous refractive index. Arranged nanostructures in tissues induce refractive index heterogeneity known as form-birefringence, or simply birefringence. Tissue birefringence arises in many tissues including nerve fiber bundles, tissues of the eye, muscle fibers, and tissues with arranged collagen fibers (collagen is the most abundant protein in mammals). In addition to the reflectivity images introduced by OCT, Polarization-Sensitive (PS) OCT provides birefringence images of tissues and reveals structural and functional information. In contrast to conventional OCT, PSOCT provides reflectivity images that are not altered by tissue birefringence.

Two major approaches are usually taken to implement PSOCT: the bulk optics approach that guarantees simple mathematical algorithms but lacks the flexibility required in medical setups; and the conventional fiber optics setups that are flexible to use but require sophisticated setups, complex algorithms, and multiple measurements. In this work, we have developed a third approach to build PSOCT systems using a special type of optical fibers known as polarization-maintaining fibers (PMF), and introduced the first PMF-based PSOCT capable of generating images of biological tissue. PMF preserves two independent polarizations states with high immunity to external perturbations. PMF-based PSOCT retain the flexibility of conventional fiber-based systems, and recovers reflectivity and birefringence information in a single measurement using computationally-inexpensive algorithms. The benefits of using PMF-based PSOCT are depicted in Figure 1.1. Herein, we introduce the novel systems and some of their applications, and we present a new algorithm to correct for errors in the representation of PSOCT images.

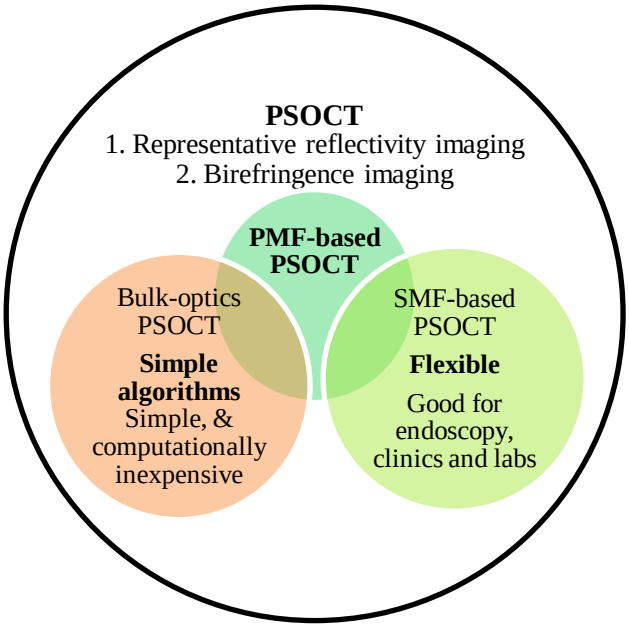

Figure 1.1 PMF-based PSOCT systems retain the flexibility exhibited by conventional fiber systems, and employ the compensation-free algorithms used in bulk optics systems.

1.2 ORGANIZATION OF THE DISSERTATION

The first two chapters of this eight-chapter dissertation are introductory materials. Chapters 3 through 7 contain the contribution of this work. Despite slight organizational differences due to content, a general theme is followed to make the manuscript more readable. Each chapter begins with an abstract that briefly introduces the reader to the purpose of the chapter. Background information unique to each chapter is delivered in the introduction section, which also brings the significance of the work to the reader's attention. The concept of the approach is described, if possible, before the method. The hardware setup and/or method are presented in detail, either preceding or following the theoretical analysis. Characterization data and results are then demonstrated. The discussion section in each chapter could contain in-depth analysis, future directions, and special design considerations that may not be understood if presented earlier. Each chapter concludes with a paragraph that briefly describes the accomplished work. All the sections are divided into subsections that are consistently titled to assist browsing the manuscript, and self-referencing. A brief summary of the contribution of this work is presented in Chapter 8.

Polarization-Sensitive Optical Coherence Tomography is based on a broad background in physics and engineering. Therefore, four appendices are added to the manuscript. The appendices contain inclusive and descriptive derivations and discussions that will considerably assist the non-expert reader. Appendixes A, B, C, and D are recalled whenever needed.

Chapter 2 presents essential and brief background for the major topics in this dissertation. We start with the choice of the wavelength window in OCT. We also present the basics of LCI and OCT, and the Time-Domain and Fourier-Domain operation modes. The chapter concludes by presenting light polarization, form-birefringence, and the benefits of using PSOCT over conventional OCT imaging.

In Chapter 3, the first PMF-based PSOCT system to demonstrate imaging of tissues at the theoretical resolution is presented. The time-domain system operates at the 850 nm range, and utilizes frequency multiplexing to enable single-detector operation. Using PMF, two complex measurements are acquired in a single depth-scan, sufficient to calculate tissue reflectivity and birefringence. The sample is illuminated by circularly-polarized light, yielding retardance measurement insensitive to the lateral sample orientation, and enabling the measurement of the axis orientation of the sample. Characterization results of the system are presented, and tissue images with transform-limited resolution and high dynamic range are demonstrated. Implementation details and important design considerations are disclosed.

In Chapter 4, the PMF-based system introduced in Chapter 3 is slightly modified to operate as an LCI. The superior sensitivity of the interferometer made the measurement of minute Faraday rotations possible. Instead of direct measurement of the angle of rotation of a linear polarization state, Faraday rotation is calculated from the phase shift between two oppositely polarized states reflected from the sample. Compared to common techniques, this approach enables the measurement in considerably smaller sample sizes, and under the influence of weaker magnetic fields. The measurement of the magneto-optical interaction is demonstrated possible using light reflected from tissue-mimicking phantoms.

In Chapter 5 another slight modification is applied to the system to study the birefringence properties of unmyelinated nerves. The sensitivity of the differential-phase measurement of the system approaches the theoretical value. The extremely small birefringence is measured as the phase difference between two orthogonal linear polarizations aligned with nerve axis. Resting retardance of crayfish and lobster nerves is imaged, and transient retardance of activate nerves is calculated. In attempts to measure the transient retardance during neural activity, a method to optimize the system to provide long term stability is presented.

Another PMF-based PSOCT system designed for tissue imaging is presented in Chapter 6. The system operates in Fourier-domain enabling video-rate and fast volume imaging. The laser source, implemented in-house, is centered at 1280 nm to provide maximal imaging depth OCT can offer. Balanced detection yields an energy-efficient system, and rejection of the source noise. System characterization and tissue images are presented, and the possibility to compensate for the offset in axis orientation images is demonstrated. In this chapter, we establish that PMF-based PSOCT provides sensitivity figures comparable to equivalent conventional PSOCT.

Chapter 7 treats common errors in the representation of birefringence PSOCT images. PSOCT measures the cumulative polarization properties of tissues, yielding errors and distracting banding patterns. We present detailed analysis of the origin of this error, and a novel algorithm to correct PSOCT images. Bands in PSOCT images are detected using Canny edge detector, and the correct mathematical formulas are applied to the corresponding bands. Local retardance is calculated, and regions with inadequate accuracy in the axis orientation images are masked. A method to automatically detect features of birefringence images and appropriately adjust the edge detector is presented. Images of various tissues demonstrate improved differentiation of structures in the corrected images.

Chapter 8 summarizes the contributions of this dissertation to the field, and gives the future directions to build on this work.

CHAPTER 2
BACKGROUND

2.1 LIGHT EXTINCTION IN TISSUES

The opacity of most tissues in the visible spectrum is largely dominated by light scattering. Turbidity is the inability to see through a material due to light scattering. Light energy in a turbid medium scatters in all directions, and some of this light is back-scattered along the axis of light incidence. Insightful examples are shown in Figure 2.1. Milk is usually used to emulate the scattering properties of tissues. In Figure 2.1 (a), a cup of milk is illuminated from the bottom; scattered light is viewed from any angle. In Figure 2.1 (b), a turbid bead of glass looks blue under white light; red light is transmitted. Rayleigh scattering is stronger at shorter wavelengths, and the blue light is scattered towards the viewer. This example demonstrates that, under Rayleigh scattering regime, light with longer wavelength travels deeper into turbid media.

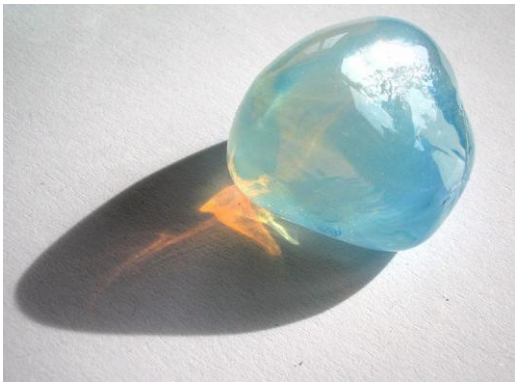

(a) **(b)**

Figure 2.1[1] (a) Milk is commonly used to emulate the scattering behavior of tissues. When a cup of milk is illuminated from the bottom, the scattered light can be viewed from any angle. (b) Under Rayleigh scattering regime, the scattering coefficient is inversely proportional to wavelength, and a piece of turbid glass looks blue under white light. Red light, which has a longer wavelength, penetrates deeper in scattering media.

Figure 2.2 shows important optical characteristics of tissues. Rayleigh scattering dominates tissue scattering, its scattering coefficient[2] decreases proportional to the fourth power of the wavelength and reaches a low level in the IR region. Water constitutes a significant fraction of the mass of tissues. Water absorption[3] of light increases dramatically as the wavelength goes deeper in the IR. The optimal wavelength window to image deep layers of tissue using light is between 800 nm and 1500 nm.

---

[1] The pictures are adapted from WebExhibits. http://www.webexhibits.org/causesofcolor/14B.html

[2] Curve source: Steven L. Jacques, Oregon Medical Laser Center News, Jan 1998. http://omlc.ogi.edu/news/jan98/skinoptics.html

[3] Data source: G. M. Hale and M. R. Querry, "Optical constants of water in the 200nm to 200μm wavelength region," Applied Optics, 12, 555-563, (1973). http://omlc.ogi.edu/spectra/water/abs/index.html

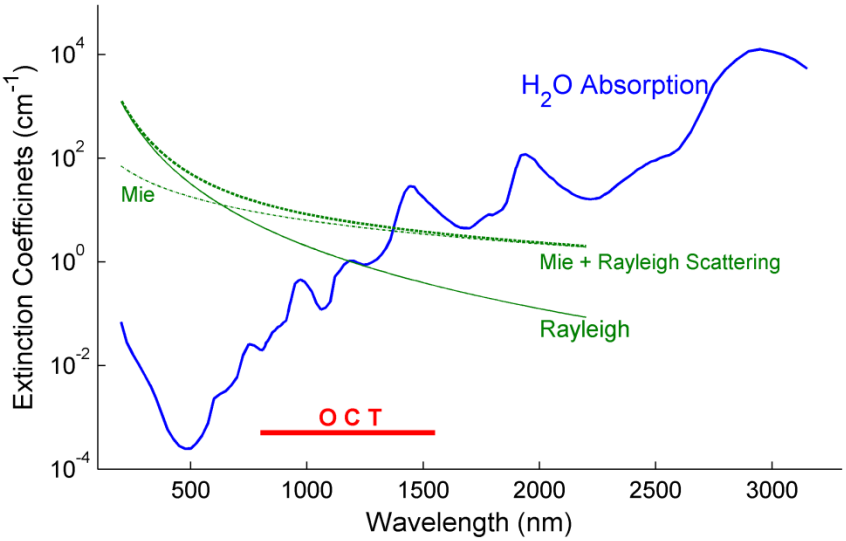

Figure 2.2 Extinction of the light wave in tissue occurs due to a number of factors. The scattering coefficient decreases at longer wavelengths, while water absorption dramatically increases. OCT is operated in the range when light extinction in the target tissue is minimal.

OCT systems illuminate a sample with low-coherence light. Light back-scattered from within the sample is detected to recover its depth-resolved reflectivity. OCT systems designed to image the retina usually operate in the range of 800 nm to 1050 nm. In this range water absorption is lower, and the vitreous humor is less absorbing. When there is no water mass between the imaged tissue and OCT system, tissue scattering plays the major role in light extinction, and OCT systems are operated around 1300 nm. In rare cases, systems at 1500 nm were presented.

2.2 Low-Coherence Interferometry

Interferometry is an optical technique that has been commonly employed to measure the amplitude and phase of an unknown light wave in various applications. Interferometers primarily add two mutually coherent waves, one of them with known amplitude and phase. The interference pattern of the two waves carries complex information about the unknown signal, i.e. its amplitude

and phase. It is common to refer to the unknown and the known waves as “sample” and “reference”, respectively.

It is important to mention that Low Coherence Interferometry (LCI) is based on temporal not spatial interferometry. Because most of the detailed mathematical treatments in literature describe the spatial coherence phenomenon, detailed derivation of the LCI and OCT equations is attached in Appendix A. All the interferometers presented in this dissertation are based on Michelson configuration illuminated with a low-coherence source, and the following description is therefore limited to this fundamental configuration. The mathematical treatment of temporal coherence introduced in Appendix A can apply to other configurations like Mach-Zehndar interferometer.

Figure 2.3 shows the basic setup of a Michelson interferometer with low-coherence illumination. LCI is used to refer to this basic configuration. In LCI, a beam splitter transmits part of the source light onto the reference mirror, and the rest illuminates the sample. Light waves reflected from the two ends interfere at the beam splitter. The beam splitter directs a portion of the interference onto the detector. The portion that is redirected towards the source (indicated with a light color arrow in Figure 2.3) is blocked by an optical isolator or circulator. The term “sample arm” means the sample, the propagation path between the sample and the beam splitter, and the optics that may be added to the path. Similarly, the terms “reference arm”, “source arm”, and “detection arm” are defined.

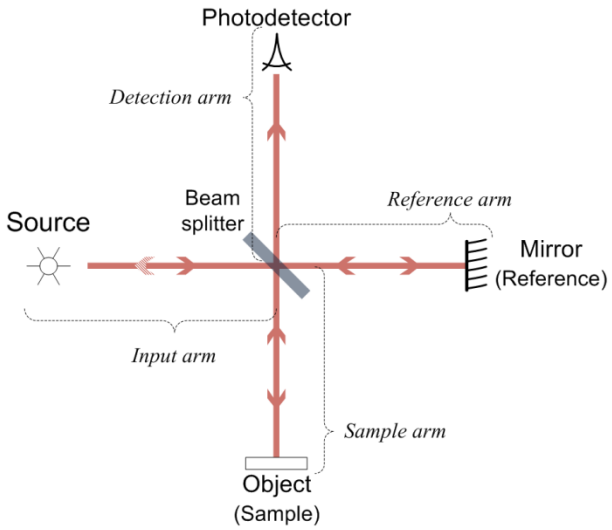

Figure 2.3 Schematic of Michelson interferometer. The beam splitter splits the light of the source into the sample and reference arms. Light reflected from the known reference and unknown sample interfere at the beam splitter, and the interference pattern is recorded on the photodetector.

Let $E_{in}(t)$ be the electric field of a low-coherence light source with a central frequency v_o, and a bandwidth Δv, where $\Delta v \ll v_o$, the intensity of the time-averaged electrical field detected using the photodetector can be written as (Equation A.17)

$$I_d = I_r + I_s + 2I_{DC}\sqrt{A}\sqrt{R}\,\mathcal{R}e\{\gamma(\tau)\} \qquad \textbf{2.1}$$

where I_s, I_r, and I_{DC} are DC light intensities. I_{DC} is proportional to the source intensity and the split ratio of the beam splitter, while I_s and I_r are proportional to I_{DC} and light attenuation in the sample and the reference arms, respectively. A is the attenuation in the reference arm, and R is the attenuation in the sample, known as the sample reflectivity. The complex degree of coherence function $\gamma(\tau)$ is solely dependent on the light source. And τ is the time delay due to the difference between the optical path lengths of the sample and reference arms.

2.3 Optical Coherence Tomography (OCT)

In OCT, turbid tissues are illuminated with a broadband near infrared light source. The highly-sensitive technique (> 90 dB) captures photons back-scattered from within the tissue, and discriminates between photons coming from different layers with a resolution on order of a few micrometers. OCT images map the reflectivity profile along the depth of the sample. Two and three dimensional images are attained by laterally scanning the laser beam on the surface of the sample. The infrared light used in OCT is non-ionizing and therefore safe at the used power levels.

The first two terms in Equation 2.1 do not carry information that are resolvable across the depth of the sample; and the DC signals is therefore blocked. When a light source with Gaussian-shaped power spectral density illuminates the interferometer, the third term of Equation 2.1 can be written as (see Equation A.27)

$$I_i(\tau) = 2I_{DC}\sqrt{A}\sqrt{R}\exp[-(\alpha\tau)^2]\cos[2\pi\nu_o\tau] \qquad \textbf{2.2}$$

where $\alpha = \pi\Delta\nu/2\sqrt{\ln 2}$.

Equation 2.2 shows that the interference pattern is proportional to the square root of the reflectivity of the sample. The function I_i is modulated at ν_o, and enveloped by a Gaussian function characterized by the bandwidth of the source. This Gaussian function is known as the coherence function. Figure 2.4 shows the coherence function for a Gaussian source, and its cosinusoidal modulation. The width of the coherence function is finite, usually on the order of a few micrometers, and the intensity I_i diminishes when τ is larger than this width.

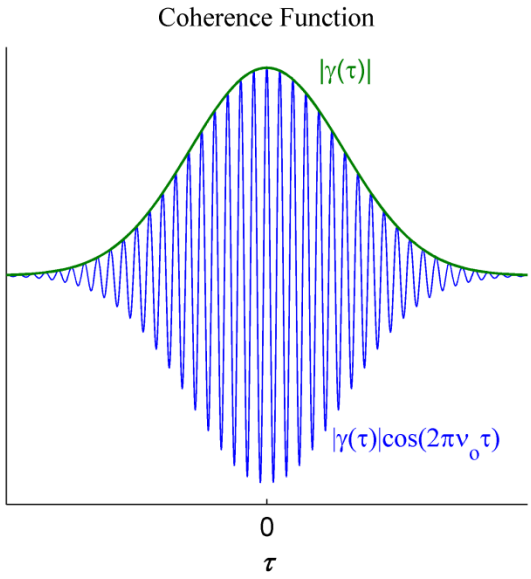

Figure 2.4 The coherence function of a Gaussian light source centered at τ = 0. The coherence function with the cosinusoidal modulation is shown in blue, and the coherence function envelope is shown in green.

2.3.1. TIME-DOMAIN (TD) OCT

If the time delay τ is increased by increasing the length of the reference arm, and another reflection came from a deeper layer in the sample arm, the detector reads a non-zero I_i. The A-line is defined as the reflectivity profile along the depth of the sample. Setups that change the time delay in the reference arm to image the A-line are known as Time-Domain (TD) OCT.

As discussed in Appendix C, the interference pattern recorded on the output of TD OCT is modulated at a frequency f. When multiple reflections $R(\tau)$ come from different layers in the sample, Equation 2.2 can be rewritten as

$$I_i(\tau) = I_o\sqrt{R(\tau)} \otimes \exp[-(\alpha\tau)^2]\cos[2\pi f\tau] \qquad \textbf{2.3}$$

where $I_o = 2\, I_{DC}\sqrt{A}$, and $\otimes$ is the convolution operator.

Figure 2.5 shows a sample of three reflectors and the corresponding A-line. The reflectivities of the three reflectors from top to down are 0.5, 0.5, and 0.8. Because $I_i\ \alpha\sqrt{R}$, and because light intensity after each reflector is attenuated, the maximum intensities measured at the same location of the reflectors are 0.25, 0.125, and 0.16, respectively.

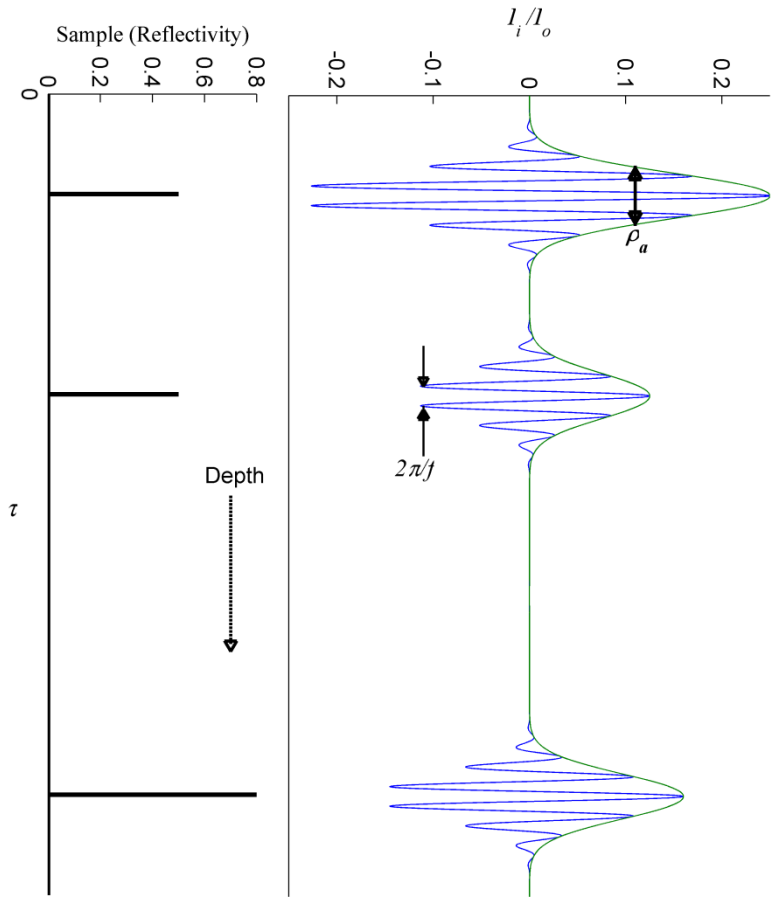

Figure 2.5 (a) Illustration of a sample of three reflecting surfaces, where τ = 0 is at the top of the sample. (b) The A-line of the sample shows a coherence function corresponding to each reflector in the sample. The axial resolution ρ_a, and the modulation interval $2\pi/f$ are indicated.

The two reflectors are not resolvable if closer than the width of the coherence function. The axial resolution ρ_a is defined as the FWHM coherence length in a medium with a refractive index *n*. OCT axial resolution is expressed as (see Appendix B)

$$\rho_a = \frac{0.44}{n}\frac{\lambda_o^2}{\Delta\lambda} \quad \textbf{2.4}$$

where λ_o is the central wavelength of the source, and $\Delta\lambda$ is its FWHM bandwidth. Better axial resolution is achieved at broader source bandwidth $\Delta\lambda$. Under monochromatic illumination the axial resolution is infinity and depth-resolved imaging is not possible.

Since TD OCT was first introduced [1], advanced mechanical scanning mechanisms were presented to increase imaging speed [2]. Faster scanning, however, means broader bandwidth of the modulation frequency due to Doppler shift, which results in degraded sensitivity [3]. The degraded sensitivity at higher acquisition speeds was observed in [4]. The following subsection shows that OCT imaging is possible without mechanical scanning of the reference arm.

2.3.2. FOURIER-DOMAIN (FD) OCT

For a light source, the coherence function $|\gamma(\tau)|$, and the source's normalized power spectral density $\hat{S}(\nu)$, are Fourier pair (see Appendix A, Equation A.22). As an alternative to changing τ, the power spectral density $S(\nu)$ can be recorded and the amplitude U of I_i and its phase φ across the entire A-line are calculated at once using Fourier transform.

$$S(\nu) \xrightarrow{\mathcal{F}} U \text{ and } \varphi \text{ for all } \tau \quad \textbf{2.5}$$

FD OCT is realized either by placing a spectrometer in the detection arm, in this case called Spectral-Domain (SD) OCT [5-7], or scanning the source spectra in the input arm and called Swept-Source (SS) OCT[8-10], or sometimes Optical Frequency Domain Imaging (OFDI). The speed of FD OCT is limited by the detection speed of the spectrometer in SD OCT, or by the source scanning speed in the SS OCT. Ordinary FD OCT systems are an order of magnitude faster

than the state of the art TD OCT, and typically more sensitive than equivalent TD systems [11-13]. Details about FD OCT and specific design consideration are attached in Appendix D.

2.3.3. SIGNAL TO NOISE RATIO

In most biological application for OCT and LCI, light power returning from the sample arm is very small, and the noise model presented in [14] applies. The main noise sources on the OCT reflectivity measurement are the detector thermal noise n_T, the source excess noise n_{ex}, and the shot noise n_{sh}. Thermal noise is independent from the power from the reference arm P_r, but $n_{excess} \ \alpha \ P_r^2$ and $n_{shot} \ \alpha \ P_r$. The detected intensity on the output of OCT systems is squared to calculate R, see Equation 2.2. The signal $I_i^2 \propto I_{DC}^2 \propto P_r$ (see Appendix A) and the Signal to Noise Ration (SNR) can be written as [14]

$$\text{SNR} = \frac{I_i^2}{n_T + n_{sh} + n_{ex}} \qquad \textbf{2.6}$$

At extremely low P_r, excess noise is small and the SNR is dominated by the detector noise. As P_r increases, the signal power and SNR increase. After the point when $n_T = n_{ex}$, excess noise, which is quadratically proportional to P_r, dominates and SNR degrades again. The optimal SNR is reached when $n_T = n_{ex}$. The reference arm of OCT is typically equipped with an attenuator to achieve this condition. One can calculate the optimal attenuation from the equations for n_T and n_{ex} in [14], and the fact that $P_r = P_{in} k_r A^2$ as

$$A = a \frac{1}{\sqrt{P_{in} R}} \qquad \textbf{2.7}$$

Where a is a constant equal to $(2kT/R_{eff}\Delta\nu)^{1/4}(1/k_r)^{1/2}$, k is Helmholtz constant, T is the detector temperature, R_{eff} is the detector's effective noise resistance, P_{in} is the power of the laser source, and k_r is the split ratio of the beam splitter into the reference arm.

To further improve SNR, light from the input arm can be collected and subtracted from light in the detection arm, which doubles the signal and eliminates the excess noise. This approach is known as balanced detection and is presented in the system in CHAPTER 6.

2.3.4. PHASE NOISE

Noise on the phase of the interference pattern is related to the intensity SNR [15]. Standard deviation of phase noise, σ_θ, in radians is inversely proportional to the linear SNR of the intensity I_i

$$\sigma_\theta = \sqrt{\frac{1}{2\mathrm{SNR}}} \qquad \textbf{2.8}$$

Phase noise is largely influenced by mechanical and thermal vibrations too; Equation 2.8 does not account for these environmental perturbations.

2.4 POLARIZATION OF LIGHT

Light polarization describes the orientation of electrical field oscillation of the light wave along the propagation axis. The light wave that propagates in the *z*-direction oscillates in the *x*-*y* plane; and the electric field of any polarization state can be described by the *x* and *y* components. For a low-coherence light wave with $\Delta v \ll v_o$, the electric field of the wave can be written as

$$E(t) = E_x(t)\hat{x} + E_y(t)\hat{y} \qquad \textbf{2.9}$$

where $E_x(t) = |E_x(t)|\cos[2\pi v_o t]$, $E_y(t) = \left|E_y(t)\right|\cos[2\pi v_o t - \Delta\varphi]$, and $\Delta\varphi$ is the phase difference between the electric field components in the *x* and *y* directions.

When either of $|E_x|$ or $|E_y|$ is equal to zero, light is said to be linearly polarized in the *y* or *x* direction, respectively. When $|E_x|$ and $|E_y| \neq 0$, the polarization state can be more complex. If $|E_x|$

and $|E_y|$ are in phase, that is $\Delta\varphi = 0$, the polarization is linear and oriented on *x*-*y* plane with an angle that depends on the ratio between $|E_x|$ and $|E_y|$. When $\Delta\varphi \neq 0$, the polarization state is elliptical. When $\Delta\varphi = \pm\pi/2$, and $|E_x| = |E_y|$, the quantity $|E(t)| = \sqrt{|E_x(t)|^2 + |E_y(t)|^2}$ and the polarization state is clearly circular. If an optical medium alter the polarization state of propagating light, information about the heterogeneity of the media and its geometry can be incurred by studying these polarization alterations.

2.5 BIREFRINGENCE

An optical medium is isotropic when E_x and E_y experience the same refractive index *n*. Birefringent or double refraction is when the optical media has a difference, Δn, in the orthogonal refractive indexes. Intrinsic stresses in the medium can give rise to geometrical anisotropy that causes intrinsic birefringence. External stresses on an intrinsically isotropic media can also cause birefringence; this is evident in the design of polarization-maintaining fibers presented in CHAPTER 3. Another type of birefringence common to tissues is known as form-birefringence, which arises due to aligned nanostructures in the tissue.

2.6 FORM-BIREFRINGENCE[4]

Interaction between light and the propagation medium is complex in heterogeneous media. The optical characteristics of a heterogeneous medium are not necessarily similar to, or derived from the individual constituents. Interestingly, this is demonstrated in gemstones. While neither of chromium nor vanadium is green, trace amounts of them in transparent glass makes up the green emerald.

[4] Most tissues exhibit form-birefringence (excluding a few cases like the teeth enamel). In PSOCT, for convenience, form-birefringence in tissues is usually called birefringence.

When a medium is intervened with aligned structures like fibers, form-birefringence can rise in heterogeneous media that does not necessarily contain a birefringent constituent. When the period of the aligned structure is smaller than the wavelength of light[5], an induced electric field arises across the radii of the fibers, see Figure 2.6. As a result, the index of refraction parallel to the axes of the fibers takes a different value than that perpendicular to them. Because this difference is not due intrinsic geometrical anisotropies, it is known as form-birefringence[6].

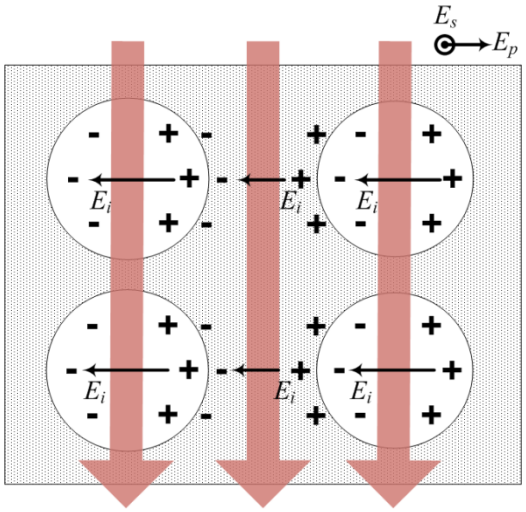

Figure 2.6 Light propagation in a medium with aligned inclusions generates an induced electrical field E_i. The induced field alters the propagation speed of the polarization state parallel to it, resulting in form-birefringence.

In most biological tissues, the observed birefringence is due to aligned fibers; which means it is form-birefringent. Collagen is probably the most abundant protein in mammals [16,

[5] If the period is larger than the wavelength of the light, the structure is a diffraction grating. The wavelength of the light divided by the period of the grating is equal to the sine of the diffraction angle. When the wavelength is larger than the period, the sine does not exist, and only the zeroth order propagates influenced by the form-birefringence.

[6] The Effective Medium Theory (EMT), and Rigorous Coupled-Wave Analysis (RCWA) are used to describe this phenomenon, and to calculate the effective properties for a medium with aligned inclusions [19].

17]. Its molecules are long, stiff, triple-stranded helical structures with typical diameter of 1.5 nm. They assemble into collagen fibrils which are thin cables 10-300 nm in diameter and many micrometers long. Collagen fibrils in turn bundle into collagen fibers [18]. Collagen fibers have high tensile strength that plays an essential role in the mechanical properties of bone, ligaments, and tendons. They give the skin its shape, and maintain the function of heart valves.

Form-birefringence is also evident in skeletal muscles, tissues of the eye (the retina, the cornea, and the iris), parts of the gastrointestinal system, the vocal cords, blood vessels, nerve bundles, and other tissues. In all of these cases, the alignment of structures is important for the tissue to perform its mechanical or functional role. Measuring the birefringence of tissue is therefore significant in clinical and laboratory setups to evaluate the health and function of tissues.

2.7 POLARIZATION-SENSITIVE (PS) OCT

2.7.1. POLARIZATION-DIVERSITY REFLECTIVITY

It is assumed in the derivation of the OCT equation, Appendix A, that light beams from the sample and reference arms have the same polarization. In practice, the polarization states in the two arms do not necessarily match. In this case, only a fraction of the light energies from the sample and reference arms interfere, and the sensitivity of OCT measurement is degraded. If the sample does not exhibit birefringence, the polarization state in the reference arm is matched to that in the sample arm by adding a polarization controller.

In birefringent samples, however, the polarization state of light changes as light propagates deeper in the sample, resulting in intensity variation in the image and potentially false interpretation. Figure 2.7 (a) illustrates tissue reflectivity of a non-birefringent and a birefringent sample as mapped using OCT. The strength of the variation in the A-line of the birefringent sample depends on the degree of polarization in light in the two arms. In PSOCT, two orthogonal

polarization channels are recorded and all light from the sample is captured, see Figure 2.7 (b). A polarization-independent, or polarization-diversity, reflectivity mapping is therefore possible. The basis of the birefringence effect shown in Figure 2.7 is described in Section 3.5.

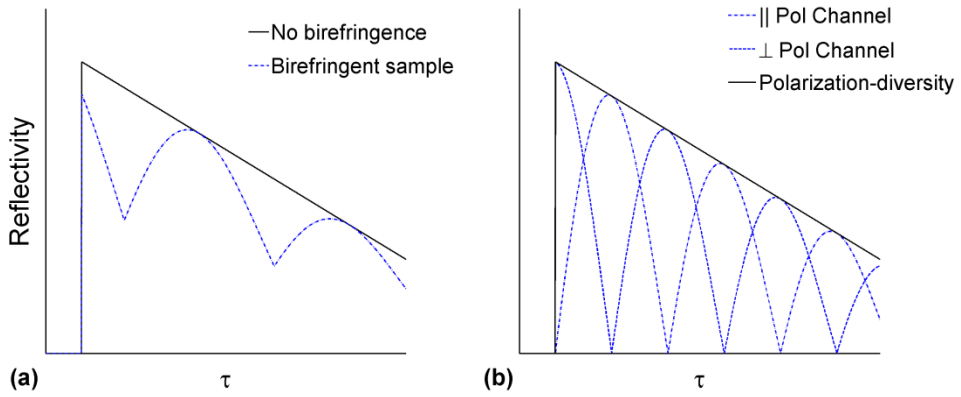

Figure 2.7 (a) Illustration of the reflectivity profiles mapped using OCT of two samples with the same reflectivity, but one of them is birefringent. The variations in reflectivity due sample birefringent are misleading. (b) When two orthogonal polarization states are recorded, a representative polarization-diversity reflectivity profile of the birefringent sample can be calculated.

Polarization-diversity reflectivity images are insensitive to polarization transformations within the sample; hence, they are stable and representative. This is an important advantage of PSOCT over OCT. Figure 2.8 shows a comparison of porcine iris images acquired using a conventional fiber-based OCT system in (a) and (b), and a PSOCT system in (c). The two systems are presented in CHAPTER 6. PSOCT generates representative images of the birefringent iris tissue. OCT images show that sample birefringence degrades the reflectivity image. The two frames are acquired under different settings of the polarization controller to show how applying different stresses on the optical fiber influences the reflectivity images. The polarization-diversity advantage of PSOCT was discussed in [20-22].

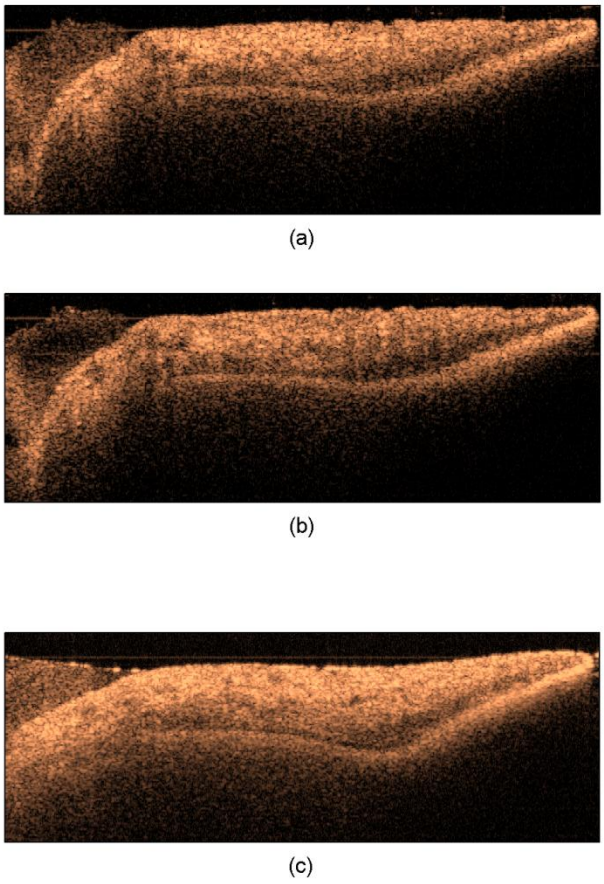

Figure 2.8 Reflectivity images of the birefringent porcine iris tissue. OCT images are shown in (a) and (b), and PSOCT polarization-diversity reflectivity image shown in (c). When (a) and (b) are compared to (c), regions with lower reflectivities can be observed. OCT reflectivity images are misleadingly altered by the birefringence of the tissue, whereas PSOCT provides more accurate representation of the iris reflectivity. The differences between (a) and (b) are due to different stresses applied to the fiber.

In conventional OCT systems, the polarization mismatch between the sample and reference arms degrades the axial resolution as we image deeper into the sample [23]. In many PSOCT configurations, like the ones presented in this dissertation, the interfering sample and reference beams have the same polarization state, and the axial resolution degradation is therefore not expected.

2.7.2. IMAGING RETARDANCE AND OPTICAL AXIS ORIENTATION

Retardance, δ, is defined as the delay between two orthogonal polarization states propagating in a birefringent medium. The amount of the induced form-birefringence depends on the dimension of the fibers and their density [19]. The optical axis orientation, θ, is measured as the orientation of the fibers with respect to a reference. By recording two orthogonally-polarized interference patterns, PSOCT images the retardance and axis orientation of a sample, in addition to its reflectivity. In the rest of this dissertation, the term birefringence is used refer to both of the quantities, δ and θ.

CHAPTER 3
PMF-BASED PS-OCT IN TIME-DOMAIN USING FREQUENCY-MULTIPLEXING [7]

The first PMF-based TD PSOCT capable of imaging tissues is demonstrated. A single depth scan is sufficient to measure reflectivity, retardance, and optical axis orientation information along the A-line. The orthogonal polarization channels are frequency-multiplexed to enable a single-detector measurement of reflectivity and retardance. The design eliminates ghost images due to the cross coupling in polarization-maintaining components within the OCT imaging range. Reflectivity and birefringence images of biological tissues with an axial resolution of 7.9 μm, and reflectivity dynamic range of 60 dB are demonstrated.

---

[7] Parts of the content of this chapter were published in the following peer-reviewed manuscripts:

- Muhammad K. Al-Qaisi and Taner Akkin, "Polarization-sensitive optical coherence tomography based on polarization-maintaining fibers and frequency multiplexing," Optics Express 16, 13032-13041 (2008).
- Muhammad K. Al-Kaisi and Taner Akkin, "Polarization-maintaining fiber based optical coherence tomography for polarization-sensitive measurements", proceedings of SPIE volume 7168 (2009).

3.1 INTRODUCTION

Conventional OCT generates depth-resolved, high-resolution, noninvasive reflectivity images of turbid tissues [1]. PSOCT is a variant that was introduced to measure polarization alterations in birefringent tissues, and obtain an additional contrast to the technique [24, 25]. Birefringence imaging reveals additional structural and functional information of tissues. Equally significant, PSOCT provides polarization-diversity images, which are insensitive to image degradations caused by tissue birefringence in conventional OCT setups.

By measuring the polarization state of light back-scattered from within the tissue, PSOCT quantitatively images depth-resolved birefringence. Demonstrated applications of PSOCT include detection and diagnosis of pathologies [26, 27], investigation of alteration in the collagen content of tissues due to thermal damage [28] or burn [29], early detection of osteoarthritis [30], differentiation of atherosclerotic plaques [31], and mapping birefringence in keratoconus corneas [32]. Birefringence exhibited by nerve fibers bundled in parallel in retinal nerve fiber layer has been suggested for glaucoma diagnosis [33].

3.2 COMMON TD PSOCT IMPLEMENTATIONS

The complexity of polarization measurements and the emerging clinical and scientific needs has resulted in a variety of approaches since PSOCT was first proposed. Several hardware setups in bulk were demonstrated sufficient to characterize polarization properties of tissues. Dual-detector TD systems with circularly polarized light incident on the sample measures retardance [21, 22] and fast axis orientation [34] in a single A-scan. Another dual-detector system has been demonstrated to calculate Stokes parameters of the sample [35]. In this system, three measurements were required to verify the optical axis orientation of the sample. A single-detector

bulk system has been proposed to generate the Mueller matrix of birefringent samples by using four consecutive A-scans with independent polarization states [36].

Unlike bulk systems, PSOCT implementations based on single mode fibers (SMF) offer flexibility and ease of alignment. In SMF, however, the polarization state of the propagating light can be altered by fiber imperfections, environmental perturbations, and stresses on the freely moving waveguide that induce static and dynamic birefringence within the fiber. SMF-based PSOCT systems were demonstrated by compensating polarization transformations in the fiber. A system with two detectors has been reported for generating the Stokes parameters [37]. Four fast consecutive A-scans were acquired while light in the input arm was modulated by a polarization modulator. A single-detector SMF-based based interferometer [38] has been designed to obtain retardance and optical axis orientation of birefringent samples. In this design, A-lines with at least three different polarization states incident on the sample had to be sequentially acquired. Using SMF, compensation algorithms are always required, and multiple measurements could be only abandoned by sophisticated implementations.

Polarization-maintaining fibers (PMF) have been used to implement LCI [39-41]. None of the reported systems, however, has demonstrated PSOCT images. PMF are described in the following subsections, followed by the hardware design of the first PMF-based PSOCT capable of imaging tissues with high resolution.

3.3 POLARIZATION-MAINTAINING FIBER (PMF)

PMF is a special type of SMF that has two stress elements inserted parallel to the fiber core along the cladding, see Figure 3.1. The resulting unidirectional stress renders a difference in the refractive index between two orthogonal axes, the fast axis and the slow axis. Light in the fast axis experience a lower index of refraction and propagates faster than the slow axis. PMF

maintains two orthogonal linear polarization states despite external perturbations. Typical polarization isolation in PMF is 40 dB per 4 m for PANDA fibers[8].

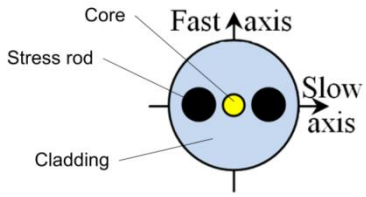

Figure 3.1 Cross section of the PMF[9]. The two stress elements create a uniaxial stress on the core and generate constant birefringence in the fiber. Two orthogonal and independent linear polarization states propagate simultaneously in PMF.

PMF segments can be spliced so that light in one polarization channel in a fiber is coupled into the same channel in the other fiber at a 0º splice angle, see Figure 3.2 (a). A 90º splices couples all the light from one channel into the other. At any other angle, light is split between the two polarization channels. In PMF-based PSOCT, inaccurate splicing of PMF results in cross-couplings between the polarization channels, and consequently disturbing ghost images.

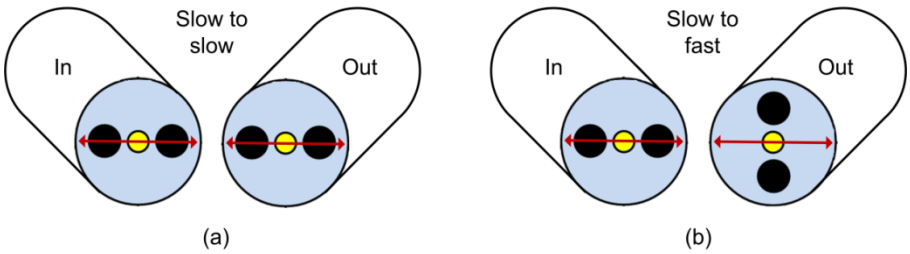

Figure 3.2 (a) Splicing the PMF at 0° couples the polarization state in the first fiber into the same polarization channel of the second fiber (slow to slow in the figure). (b) A 90° splice couples light from one channel in the first fiber into the other channel of the second fiber (shown slow to fast).

[8] From Corning datasheet

[9] Although PMF is a type of SMF, it is common in literature to use SMF for non-PMF fibers. We also use PMF for polarization-maintaining fibers and SMF for conventional fibers.

3.4 HARDWARE SETUP OF THE PMF-BASED INTERFEROMETER

Figure 3.3 illustrates a schematic diagram of the TD PMF-based setup. The interferometer is illuminated by a 5 mW superluminescent diode (SLD) (Exalos, Switzerland). The SLD has a quasi-Gaussian spectrum centered at λ_o = 856 nm, and a FWHM bandwidth $\Delta\lambda$ = 32 nm. Using Equation 2.4, the theoretical axial resolution is calculated as 10.1 μm in air (n = 1). To prevent light reflected from the interferometer from re-entering the SLD cavity, a free-space isolator is inserted between the light source and the PMF of the input arm. The isolator transmits linearly polarized light coupled into the slow channel of the PMF.

A 2×2 PM coupler (Canadian Instruments & Research Ltd, Canada) directs 30% of the light into the sample arm. A quarter-wave plate (QWP) inserted at 45º with respect to the slow axis of the fiber transmits circularly polarized light onto the sample. When the sample is interrogated with circular polarization state, retardance measurement is insensitive to the lateral rotation of the sample, and optical axis orientation measurement is possible. The birefringence of the sample alters the polarization state; therefore, light reflected from the sample has an arbitrary polarization state. The sample light couples into the slow and fast axes of the PM fiber. Hereafter, the mode that propagates both ways in the slow axis is denoted by **S**, and the mode cross-coupled into the fast axis is denoted by **X**. Similar denotation in small letters (**s** and **x**) is used for modes in the reference arm.

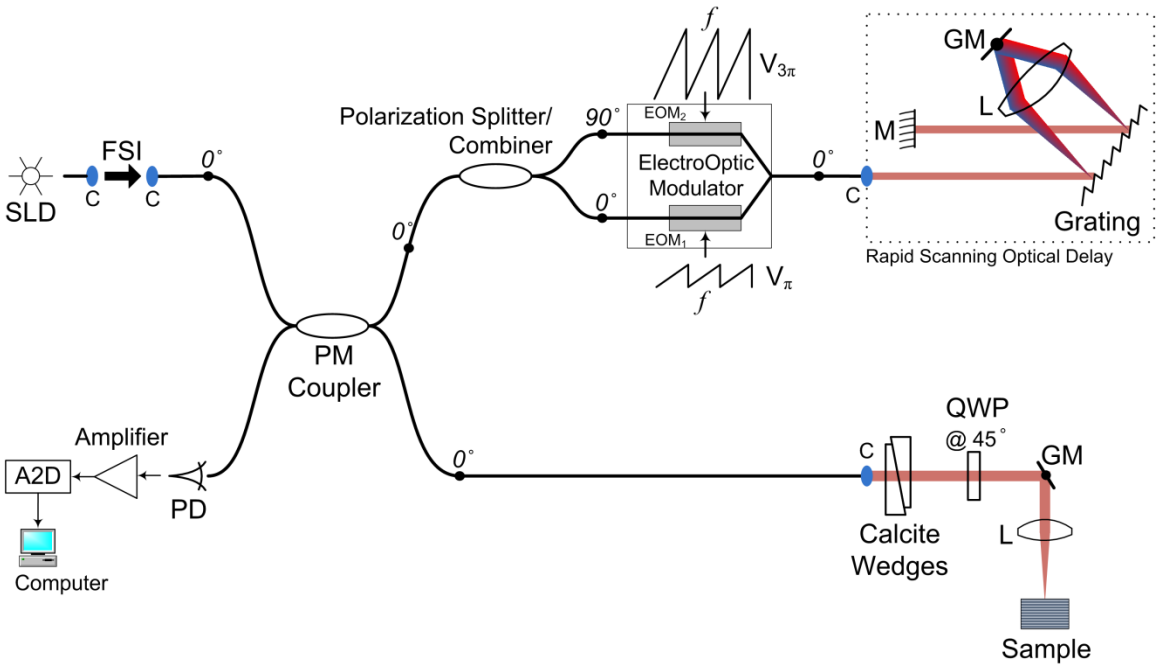

Figure 3.3 Schematic diagram of the PMF-based PSOCT. SLD – Superluminscent diode, FSI – free-space isolator, C – collimator, EO – Phase Modulator – electro-optic $LiNbO_3$ modulator, L – lens, GM – mirror mounted on a galvanometer, M – mirror, QWP – quarter-wave plate, PD – photodetector, and A2D – analog to digital converter. All fibers are PMF.

In the reference arm, a fiber-based polarization splitter/combiner (PSC) (Canadian Instruments & Research Ltd, Canada) directs the light to a Y-waveguide $LiNbO_3$ electro-optic modulator (EOM) (JDS Uniphase Corporation, California) through a 0º splice. After modulated, light in the slow channel enters a galvanometer-equipped rapid scanning optical delay line (RSOD) [2, 42, 43] that is implemented in the bulk portion of the reference arm. The RSOD provides high-speed axial scanning (up to 500 scans/s), and compensates for dispersion imbalance in the interferometer. The fringes are formed at the desired frequencies by means of the $LiNbO_3$ phase modulator[10].

[10] Phase modulation here means modulating the phase of light in the reference arm, not the phase of the interference pattern. The phase modulator here acts as a phase retarder, and, in fact, modulates the

3.4.1. FREQUENCY MULTIPLEXING

Light returning from the RSOD is equally split at the Y-connection of the EOM. In order to modulate the polarization components, EOM_1 and EOM_2 are driven by synchronized sawtooth signals oscillating at the same frequency *f*. The driving signals applied to EOM_1 and EOM_2 have amplitudes V_π and $V_{3\pi}$, respectively. Therefore, double-pass optical pathlength changes as a result of this modulation scheme are one wavelength (2π) for **s**, and two wavelengths (4π) for **x**. The interference pattern corresponding to **s** is therefore modulated at frequency *f* (see Appendix B), and because **x** is scanned two wavelengths in each cycle *f*, the corresponding coherence function is modulated at 2*f*.

The x-cut y-propagating modulator only transmits the polarization channel aligned with the slow channel of the PMF. Therefore, in the second pass, the **x** component is coupled into the fast channel of the PMF by a 90˚ splice between the modulator and the PSC. Consequently, two equal and orthogonal linear polarization states reenter PM coupler from the reference arm. These two components interfere at the PM coupler with the corresponding components in the sample arm, generating two orthogonally-polarized and frequency-multiplexed interference patterns carrying the sample information.

3.4.2. ALIGNING THE COHERENCE FUNCTIONS

Light propagates faster in the fast channel of the PMF than in the slow channel, resulting in delay between the two orthogonal states. In contrast to the component **X** in the sample arm, the component **x** in the reference arm propagates in the slow channel in the segment between the 90º splice and the collimator. Therefore the delay l_2 between **x** and **s** is smaller than the delay l_1

---

amplitude of the interference pattern. See Section 4.3. A similar modulation scheme is presented in [44 (pp 840-841)].

between **X** and **S**. Figure 3.4 depicts the polarization components returning into the PM coupler, and the delays between the components. Sample signal and reference signal refer to light reentering the PM coupler from the sample and reference arms, respectively. At the PM coupler, **s** interferes with **S**, and **x** interferes **X**. Because $l_1 \neq l_2$, the coherence functions **S-s** and **X-x** are displaced by $l = l_2 - l_1$.

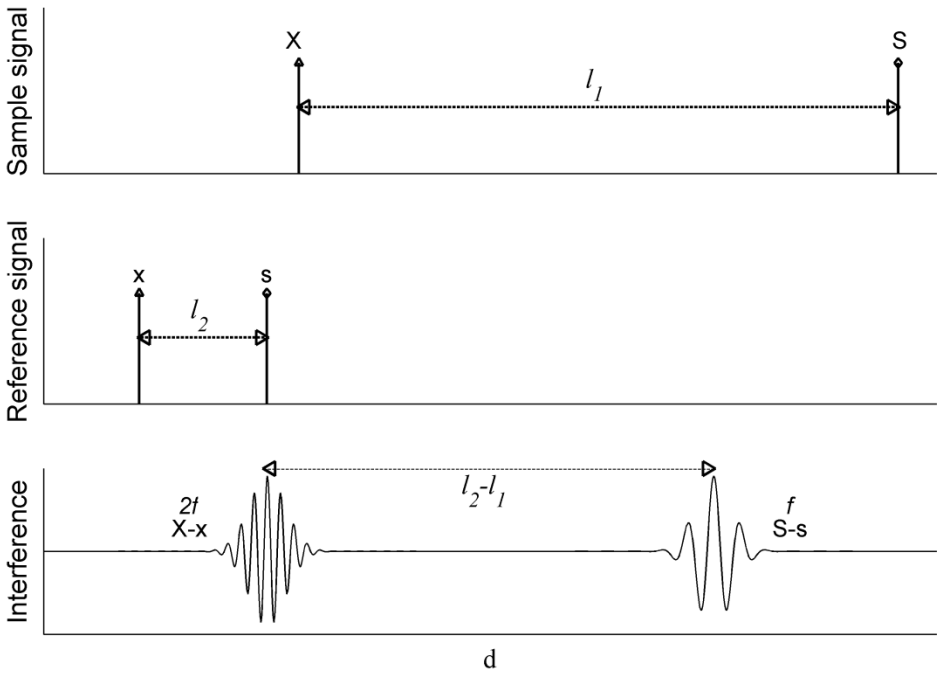

Figure 3.4 The delay l_1 and l_2 between the orthogonal channels in the sample and reference beams, respectively, are unequal, resulting in $l_2 - l_1$ displacement between the coherence functions.

In order to position the coherence functions at a same location, a birefringent cube is inserted in the sample arm to increase l_2. The axis of anisotropy of the cube is aligned with that of the PMF. For a birefringence Δn, the cube depth along the propagation axis, Ɗ, is calculated as

$$Ɗ = \frac{l}{\Delta n} \qquad \textbf{3.1}$$

The adjustable cube is shown in Figure 3.5. The two wedges cuts are made by cutting the birefringent cube at an angle *w*. By shifting one the wedges a lateral distance, *h*, the depth Ɗ is increased by

$$\Delta Ɗ = h \tan w \qquad \textbf{3.2}$$

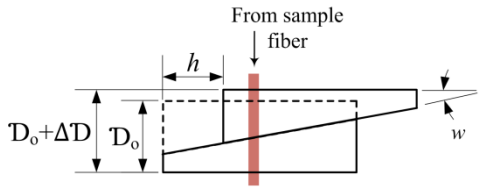

Figure 3.5 The adjustable birefringent cube inserted in the sample arm to align the coherence functions.

The wedges used here (Carl Lambrecht Corporation, Chicago) are made from calcite ($\Delta n \cong 0.17$) with $w = 7.5^{\circ}$. The shift between the coherence functions was measured as $l \approx 2.5$ mm; and the thickness of the cube when $h = 0$ is chosen based on Equations 3.1 as $Ɗ_o = 12$ mm. The induced shift between the coherence function Δl is calculated as $\Delta n h \tan w$. For $h = 100$ μm, $\Delta l = 2.2$ μm, which is a few times smaller than the axial resolution. This shows that precise alignment of the coherence functions is possible. It is difficult, however, to match the phases of the two coherence functions, resulting in a residual phase term discussed in Section 3.5.

3.4.3. Dispersion Compensation

The RSOD compensates for dispersion mismatch between the sample and reference arms. Dispersion mismatch results in chirped modulation of the coherence function and degrades the axial resolution, see Appendix B. A gold-plated[11] diffraction grating with 830 groove/mm (NT43-849, Edmund Optics, USA) is employed in the RSOD. Two-inch diameter achromatic lens with 75

[11] Light spectrum was severely degraded when aluminum-plated gratings were used. Gold-plating yields somewhat flat efficiency curve in the 850 nm wavelength range.

mm focal length (AC508-075-B, Thorlabs, USA) is used to focus the light on the galvanometer mirror. To avoid inducing fringe modulation, the mirror is laterally centered with the optical axis of the lens [2].

Group-delay dispersion (GDD) and second-order GDD can be compensated in the RSOD by changing the lens-grating distance, and the angle between the grating normal and the optical axis of the lens [42, 43]. The collimator and the grating are together mounted on a precision linear stage, and the grating angle is independently changed by a precision angular stage. The A-line is scanned and displayed in real-time while the two translational stages are retroactively aligned to achieve the shortest possible coherence length, minimal chirping, and symmetric coherence functions. Compensating the dispersion in OCT systems with $LiNbO_3$ modulator is challenging [43]; the best dispersion compensation is accomplished when the grating is between 85 - 90 mm away from the lens, and the grating angle is around 33º.

3.4.4. AXIAL SCANNING

Axial scanning is accomplished by rotating the galvanometer mirror in the RSOD [2]. Scanning the time delay, τ, in RSOD is based on the shift theorem of Fourier transform [45-47], which states that a constant shift in one domain is equivalent to a linear phase delay in the other domain, that is $\mathcal{F}\{g(t-\tau)\} = G(\upsilon)exp(-i\upsilon\tau)$. The linear phase delay in the spectral domain does not distort the shape of the coherence function [46].

The spectral components of light transmitted on the grating are dispersed onto the lens. The lens converts the diverging beams into parallel ones and focuses them in its back focal plane as a line. The spectral distribution in the lens's back focal plane is actually the Fourier transform of the input light. Therefore, slight rotation of the flat mirror applies linear phase delay in the spectrum of the light. The sample depth is linearly-scanned by applying a triangular wave to the

galvanometer. A-lines are acquired only during unidirectional slopes (rising or falling) of the wave.

3.4.5. DATA ACQUISITION

The frequency-multiplexed interference pattern is recorded in the detection arm. The coherence function **S-s** propagates in the slow axis of the reference arm's PMF, hence called I_s. Because the coherence function **X-x** is carried on the fast axis of the PMF of the reference arm, it is called I_f. When f is set to 40 kHz, the component I_s is modulated at 40 kHz whereas I_f is modulated at 80 kHz. An analog amplifier incorporated within the photodetector's (2001, New Focus, California) circuitry amplifies the recorded signal 3×10^3 times. The images demonstrated later in this chapter are acquired at RSOD scanning speed of 100 Hz. The analog bandwidth of 1 kHz to 120 kHz was found convenient at the mentioned settings. Using a 12-bit, 5 MS/s analog to digital converter (PCI 6110, National Instruments, Texas), the analog signal is acquired to a computer for demultiplexing, data processing, and image display.

For optical axis orientation measurements, the polarization channels are modulated at the same frequency f, by driving the EOM_1 and EOM_2 with sawtooth signals of amplitude of V_π. Since frequency multiplexing is disabled, a dual-detector configuration is utilized. In this configuration, a Wollaston prism in the detection arm splits the orthogonal polarization channels and diverts them onto the detectors. This setup is described in details in the phase-sensitive setups presented in the following two chapters.

3.5 THEORY

3.5.1. JONES CALCULUS

Two orthogonal linear polarizations can serve as the basis functions to describe any polarization state. Jones vector is defined as

$$E = E_s e^{-i\varphi_s}\begin{bmatrix}1\\0\end{bmatrix} + E_f e^{-i\varphi_f}\begin{bmatrix}0\\1\end{bmatrix} = \begin{bmatrix}E_s e^{-i\varphi_s}\\E_f e^{-i\varphi_f}\end{bmatrix} \quad \textbf{3.3}$$

where E_s and E_f are orthogonal polarization components parallel to the slow and fast channels of the PMF, consecutively, and $e^{-i\varphi_s}$ and $e^{-i\varphi_f}$ are the corresponding phase delays. The input polarization state can therefore be written as

$$E_{in} = \begin{bmatrix}1\\0\end{bmatrix} \quad \textbf{3.4}$$

The phase shift between the fast and slow components of the reference beam can be ideally matched in the sample arm and will be neglected. The polarization state of the reference light can be written as

$$E_r = \begin{bmatrix}1\\1\end{bmatrix} \quad \textbf{3.5}$$

For a retarder with phase retardance $\boldsymbol{\delta}$, oriented at the angle $\boldsymbol{\theta}$ with respect the slow axis of the fiber, Jones matrix can be written as [48]

$$J(\boldsymbol{\delta}, \boldsymbol{\theta}) = \begin{bmatrix}\cos^2\boldsymbol{\theta}\,.\,e^{i\boldsymbol{\delta}/2} + \sin^2\boldsymbol{\theta}\,.\,e^{-i\boldsymbol{\delta}/2} & 2i\sin\boldsymbol{\theta}\cos\boldsymbol{\theta}\sin(\boldsymbol{\delta}/2)\\ 2i\sin\boldsymbol{\theta}\cos\boldsymbol{\theta}\sin(\boldsymbol{\delta}/2) & \cos^2\boldsymbol{\theta}\,.\,e^{-i\boldsymbol{\delta}/2} + \sin^2\boldsymbol{\theta}\,.\,e^{i\boldsymbol{\delta}/2}\end{bmatrix} \quad \textbf{3.6}$$

The Jones vector of light transmitted from the fiber of the sample arm is a fraction of that in Equation 3.4. The proportionality constant is equal to the split ration of the coupler, and it is considered in the derivation in Appendix A. Therefore, it will not be considered here and light transmitted from the fiber of the sample arm can be described as E_{in}. If the sample was treated as a linear retarder with $\boldsymbol{\delta} = \delta$ and $\boldsymbol{\theta} = \theta$, and a Jones matrix J_{sample}, Jones vector of the sample light can be written as

$$E_{sample} = J(\lambda/4, 45^{\circ}).J(\delta,\theta).\sqrt{R}.J(\delta,\theta).J(\lambda/4, 45^{\circ})E_{in} \quad \textbf{3.7}$$

Solving Equation 3.7 yields

$$E_{sample} = \sqrt{R}\begin{bmatrix} \sin\delta \\ \cos\delta \, . \, e^{i(2\theta+\pi)} \end{bmatrix} \quad \textbf{3.8}$$

Equation 3.8 shows that the sample light carries information about reflectivity, retardance and the slow axis orientation of the sample. All the variables in Equation 3.8 are depth-dependent. Similar analyses were shown in [28, 34]. The constant phase delay, π, is due to double-passing the QWP in the sample arm.

3.5.2. SIGNAL PROCESSING

Equation 3.8 shows that the actual sample reflectivity is modulated by the birefringence of the sample. Reconsidering the derivation in Appendix A, light intensity recorded using the detectors can be expressed as

$$I_i = I_o\sqrt{R} \otimes \exp[-(\alpha\tau)^2][\sin\delta\cos(2\pi f_1\tau) + \cos\delta\cos(2\pi f_2\tau + \pi + \varphi_o + 2\theta)] \quad \textbf{3.9}$$

where $f_1 = f$, $f_2 = 2f$, and φ_o is an arbitrary phase bias. In this system, φ_o results from imperfect matching between the sample and reference arm as discussed Section 3.4.2, and a phase shift introduced by the analog detector. Digital bandpass filters centered at f_1 and f_2 with similar bandwidths separate the two bracketed terms. The coherence functions I_s and I_f detected on the slow and fast channels of the PMF of the detection arm, respectively, can therefore be written as

$$I_s = I_o\sqrt{R} \otimes \exp[-(\alpha\tau)^2]\sin\delta\cos(2\pi f_1\tau) \quad \textbf{3.10}$$

$$I_f = I_o\sqrt{R} \otimes \exp[-(\alpha\tau)^2]\cos\delta\cos(2\pi f_2\tau + \varphi_o + \pi + 2\theta) \quad \textbf{3.11}$$

To calculate the envelopes of the demultiplexed intensities, U_s and U_f, the signals I_s and I_f are demodulated using Hilbert transform. The output of applying Hilbert-transform to a real sinusoidal/cosinusoidal signal tracks the input with a constant 90° and a unity gain at all frequencies [49, 50]. For a cosine signal, this yields a sine output, and for sine signal, Hilbert transform yields a negative cosine. Hence, the following expressions can be written

$$\mathcal{H}\{I_s\} = I_o\sqrt{R} \otimes \exp[-(\alpha\tau)^2] \sin\delta \sin(2\pi f_1 \tau) \quad \textbf{3.12}$$

$$\mathcal{H}\{I_f\} = I_o\sqrt{R} \otimes \exp[-(\alpha\tau)^2] \cos\delta \sin(2\pi f_2 \tau + \varphi_o + 2\theta) \quad \textbf{3.13}$$

where $\mathcal{H}$ is the Hilbert transform operator. Note that in derivation of Equation 3.13, the negative sign of the cosine has complemented the constant phase π to 2π, hence both were dropped. U_s and U_f can now be calculated as

$$U_s = |I_s + i\mathcal{H}\{I_s\}| = I_o\sqrt{R} \sin\delta \otimes \exp[-(\alpha\tau)^2] \quad \textbf{3.14}$$

$$U_f = |I_f + i\mathcal{H}\{I_f\}| = I_o\sqrt{R} \cos\delta \otimes \exp[-(\alpha\tau)^2] \quad \textbf{3.15}$$

Equations 3.14 and 3.15 show that the square root of R is modulated with $\sin(\delta)$ in U_s, and $\cos(\delta)$ in U_f. This modulation was graphically demonstrated in Figure 2.7 (b). Using the two equations, and dropping the Gaussian envelope to simplify the equations, we can write

$$U^2 = U_s^2 + U_f^2 \propto [R\sin^2\delta + R\cos^2\delta] \otimes \exp[-(\alpha\tau)^2] \propto R \otimes \exp[-(\alpha\tau)^2] \quad \textbf{3.16}$$

and the polarization-diversity reflectivity can be calculated as

$$R \propto U_s^2 + U_f^2 \quad \textbf{3.17}$$

Phase retardance can be expressed as

$$\delta = \text{atan}\left(\frac{U_s}{U_f}\right) \quad \textbf{3.18}$$

The sensitivity of reflectivity imaging using OCT typically exceeds 90 dB [11-13]. It is therefore convenient to display reflectivity images on a logarithmic scale to give rise to smaller reflectivities. Because $R \alpha U^2$, the reflectivity image is displayed as

$$R^{log} = 10\log_{10} R = 20\log_{10} U \quad \textbf{3.19}$$

The slow axis orientation is modulated on the phase difference between I_s and I_f, see Equations 3.10 and 3.11. For axis orientation imaging, the polarization channels are modulated at the same frequency, $f_1 = f_2 = f$, and the dual-detector setup is employed. Using Hilbert transform, the arguments φ_s and φ_x are calculated as

$$\varphi_s = \text{atan}\left[\frac{\mathcal{H}\{I_s\}}{I_s}\right] = 2\pi f\tau \quad \textbf{3.20}$$

$$\varphi_f = \text{atan}\left[\frac{\mathcal{H}\{I_f\}}{I_f}\right] = 2\pi f\tau + \varphi_o + 2\theta \quad \textbf{3.21}$$

And the optical axis orientation of the sample with respect to the slow axis of the PMF is given by

$$\theta = \frac{\varphi_f - \varphi_s - \varphi_o}{2} \quad \textbf{3.22}$$

Because φ_o can be only measured experimentally, and because it is altered by environmental fluctuations, it is useful to define the relative axis orientation, $\hat{\theta}$, when the absolute measurement is not crucial. Compensation of φ_o is discussed in Section 6.5.2.

$$\hat{\theta} = \theta - \frac{\varphi_o}{2} = \frac{\varphi_f - \varphi_s}{2} \qquad \textbf{3.23}$$

The differential phase operation in Equations 3.22 and 3.23 provides common mode noise rejection; and therefore, the axis orientation measurements demonstrate low noise levels.

3.6 System Characterization

3.6.1. Axial Resolution

A glass wedge is placed in the sample arm as a single reflector. With a non-birefringent sample, double passing the QWP at 45º rotates the linear polarization state a 90º. Therefore, the QWP is aligned at 45º by coupling the entire sample light in the fast channel of the PMF; or in other words, by maximizing I_f. Because of practical concerns described in [51], the QWP is slightly tilted in plane perpendicular to the optical axis. A liquid crystal variable retarder (VR) is inserted in the sample arm between the QWP and the lens to simulate a birefringent sample. The recorded signal, and recovered coherence functions are shown in Figure 3.6.

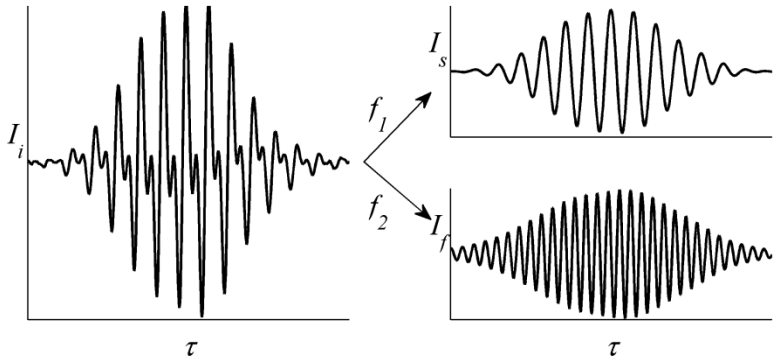

Figure 3.6 The frequency-multiplexed coherence function, and the coherence functions on I_s and I_f after demultiplexing.

The axial resolution is measured at the FWHM the coherence function. The measured resolution is 11.1 μm in air. Considering the refractive index in tissue as 1.4, the axial resolution is

equal to 7.9 μm in tissue. The deviation from the theoretical value is partially attributed to the possible spectral reshaping in the reference arm - the reference arm is complex, and the wavelength-dependent efficiency of its components reshapes the spectrum of the source.

Residual dispersion mismatch also contributes in the slight deviation from the theoretical resolution value. The RSOD can only compensate dispersion mismatch on I_s and I_f by the same value. The reference paths **s** and **x** are not similar; see Section 3.4.2, and the best dispersion compensation for one channel is achieved when the other is not best-compensated. The RSOD is therefore set to make the two coherence functions as identical as possible. Unequal dispersion compensation can be observed on the coherence functions in Figure 3.6, where I_f is slightly broader than I_s. Because the source bandwidth is relatively small, the difference here is acceptable. At larger $\Delta\lambda$, however, additional design considerations must be taken.

3.6.2. BIREFRINGENCE MEASUREMENTS

To characterize the birefringence measurement using the system, the VR is used as a standard. The retardance measurement was launched using the single- and dual-detector setups for comparison. Figure 3.7 shows the retardance measurement versus the VR's driving voltage. Because the amplitude ratio in Equation 3.18 is always positive, the phase retardance calculated using the arctangent function is bounded between zero and 90˚ as shown in Figure 3.7 (a). The unwrapped retardance curves are plotted in Figure 3.7 (b) against the manufacturer's test data of the VR. The slight difference between the measured curves and manufacturer's is mainly attributed to the fact that the manufacturer data was acquired at 848.7 nm; slightly different than λ_o. Other factors like misalignments, imperfect circular polarization due to the mismatch between the wavelength of the QWP (830 nm) and λ_o, and/or the temperature dependence of the VR can emerge into errors, too. The results show that, for retardance measurement, the single-detector system is comparable to the equivalent dual-detector system.

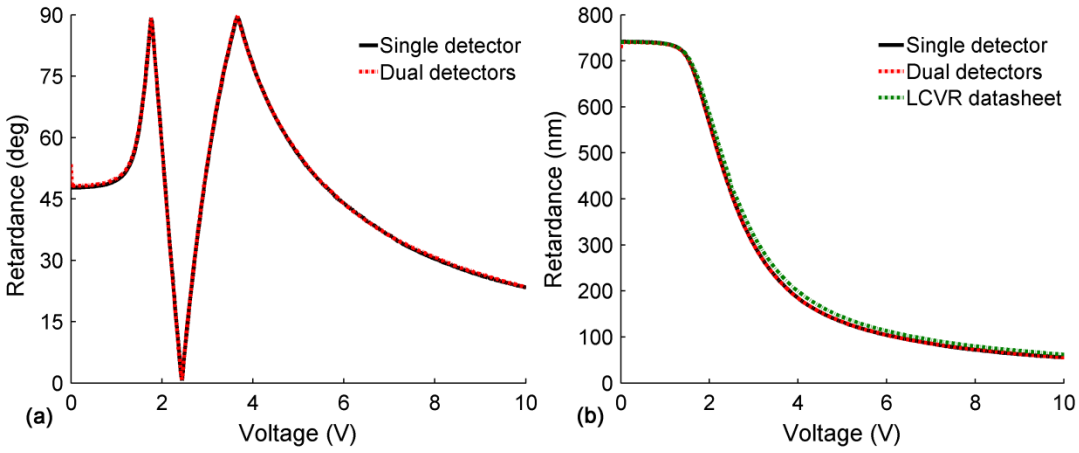

Figure 3.7 (a) Retardance measurement of a voltage-controlled VR using single and dual detector setups. (b) Retardance after unwrapping plotted against the manufacturer's test data.

Figure 3.8 shows the measurement of the axis orientation with dual-detector setup. Retardance of the VR is fixed at about 42˚ (≈ 7 V), and the VR is rotated 180˚ with 5˚ incremental steps. Figure 3.8 (a) shows the relative axis orientation. The slope of the data set is 1.08. The absolute axis orientation measurement is calculated by subtracting the constant phase offset in Equation 3.22, $\varphi_o/2$, from all the measurements. The retardance measurement is insensitive to sample rotation as shown in Figure 3.8 (b). The mean and standard deviation of the phase retardance measurement are 43.65˚ and 0.79˚, respectively. Errors in the measurements are attributed to imperfect polarization components, and temperature dependence of the VR.

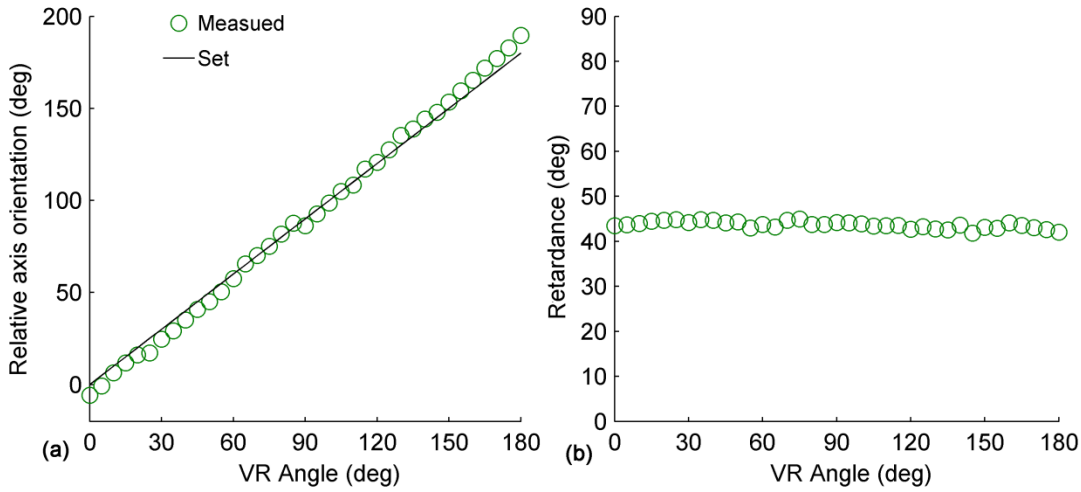

Figure 3.8 (a) Measurement of the relative axis orientation of the VRs. (b) Phase retardance measurement is insensitive to the axis orientation of the sample.

3.7 TISSUE IMAGING

A mouse tail with the tendons exposed is placed under the sample arm of the PMF-based TD PSOCT. The axial scans are performed in the RSOD. Each frame consists of 400 A-lines, and is recorded in 4 seconds. If a photodetector with higher bandwidth was used (currently 150 kHz), the axial scanning speed (currently 100 Hz) can be increased. The optical power incident on the tissue is approximately 1 mW. The interference signal consisting of 60 kHz and 120 kHz modulations is digitized at 3 MS/s.

To demonstrate that the single-detector setup produces image quality similar to the dual-detector setup, the same section of the mouse tail was imaged using the two configurations. Images shown in Figure 3.9 (a) and (b) are acquired with the single-detector system. Figure 3.9 (c) and (d) shows the dual-detector images. The reflectivity images, (a) and (c), are displayed with 60 dB dynamic range. The lateral resolution, calculated using Equation B.2 with f_{obj} = 40 mm and d_b = 1.2 mm, is equal to 26 μm. The image shows the tendons (bright structures on the sides), and an artery in the middle.

The polarization-diversity reflectivity images are not intervened by the birefringence of the tendons. Separate retardance images are instead shown in Figure 3.9 (b) and (d). The polarization state of light changes as it propagates in a birefringent tissues. Retardance measurement wraps around 0º and 90º, see Equation 3.9; and tissue birefringence results in banding patterns[12] as shown in the retardance images. The frequency of the banding pattern along the depth of the sample is proportional to the retardance. A constant systematic error in the retardance measurement increases at lower reflectivity levels [28]; regions with large errors are masked when the reflectivity SNR drops below a threshold, 6 dB here.

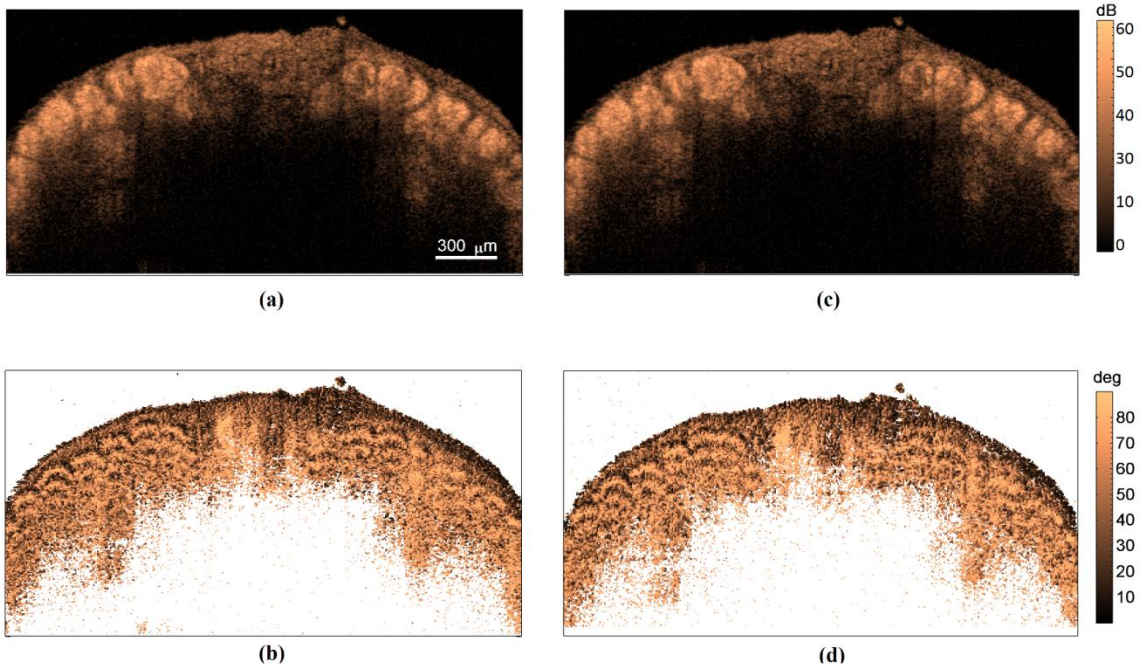

Figure 3.9 Images of the same section of a mouse tail acquired using dual-detector (a) and (b), and single-detector (c) and (d) setups. Polarization-diversity reflectivity images (a) and (c) exhibit the same dynamic range, and retardance images (b) and (d) are comparable.

[12] Although this representation of retardance images is common to all PSOCT systems in literature, the representation is incorrect. Errors in retardance representation and a method to correct them are presented in CHAPTER 7.

To test the PMF-based TD PSOCT using a different light source, we used mode-locked Ti-Sapphire laser with 45 nm bandwidth centered at 835 μm. A mouse foot was imaged by the dual-detector setup after removing the skin. The optical power now incident on the tissue is 3 mW. Figure 3.10 (a) shows the reflectivity image with 6.8 μm × 25.5 μm theoretical axial × lateral resolution, and 52 dB dynamic range. The extensor tendons are not easily distinguished in the reflectivity image. However, the banding patterns due to the tissue birefringence clearly indicate the location of the tendons in the retardance image in (b). The relative angular divergence of the tendons is obtained from the relative axis orientation image shown in Figure 3.10 (c). Regions with reflectivity SNR below 16 dB are masked in the birefringence images[13]. In this experiment, the interference channels modulated at 80 kHz are sampled at 2 MS/s.

[13] The current masking scheme is appropriate for retardance images, but it does not necessarily mask all high-noise regions in the axis orientation image. Another scheme is presented in CHAPTER 7

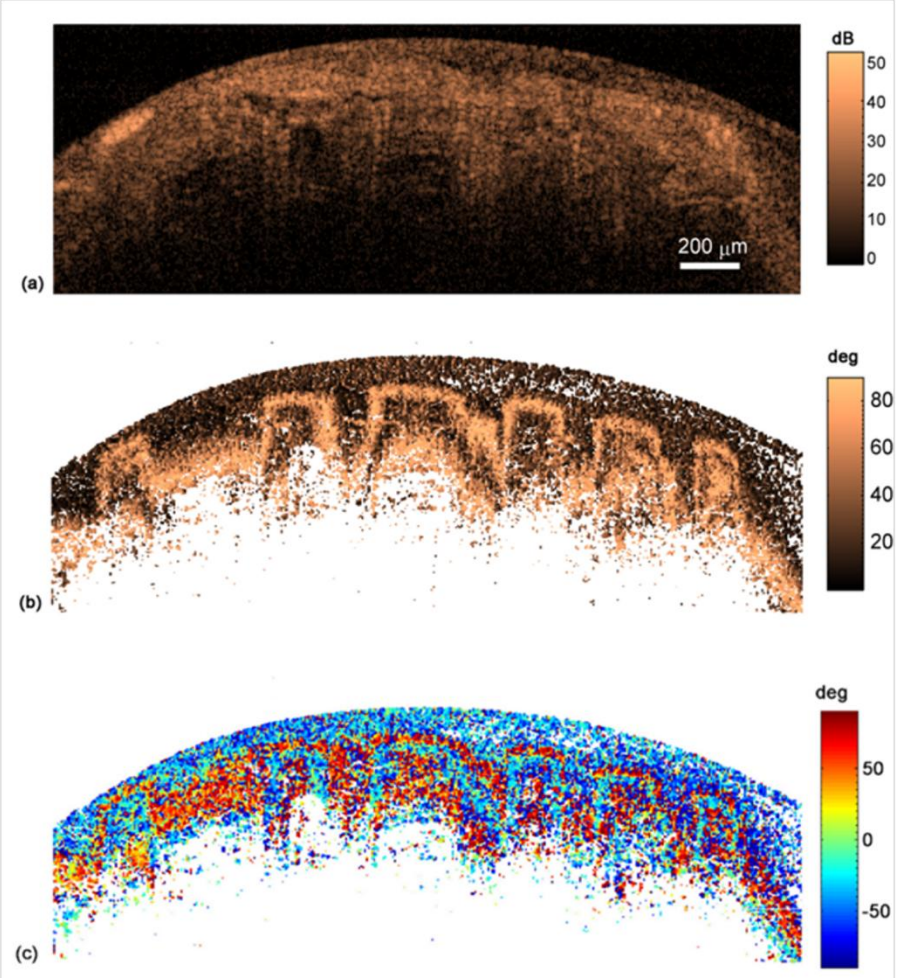

Figure 3.10 Dual-detector images of a mouse foot. (a) Polarization-diversity reflectivity, (b) retardance, and (c) relative axis orientation images. The birefringence images clearly show the extensor tendons that are not easily recognized in the reflectivity image.

3.8 DISCUSSION

3.8.1. GHOST IMAGES

The major challenge in PMF-based PSOCT design is ghost images. Leakage between the orthogonal polarization channels yields undesired components that interfere with other polarization components generating ghost images. The PMF-based TD PSOCT design eliminates ghost lines within the OCT imaging range (2 mm). PMF splices can induce leakage (sometimes

known as mode-mixing) if the segments are not precisely oriented; resulting in ghost images. Accurate splicing of PMF is described in the following subsection.

Polarization leakage can also result from imprecise coupling of the input polarization state in the slow channel of the PMF, which yields a fixed line in the image. Precise alignment was accomplished by rotating the free-space isolator while the A-line is displayed in real time. The isolator was fixed in the position that minimized the corresponding fixed line. We have also observed that the grating in the RSOD produces polarization leakage when the incident polarization state is not aligned parallel or perpendicular to its grooves. The polarization state of light illuminating the grating in the RSOD is aligned with the grooves by finely rotating the RSOD collimator while the A-line is scanned.

Polarization leakage in fabricated components, like the PM coupler and the PSC, is unavoidable. In optimized OCT systems, the reference light has much larger intensity than the sample light (see Section 2.3.3). Therefore, leakage in the reference arm has more significant contribution to the amplitude of the ghost lines. When light is transmitted into the reference arm, leakage into the fast channel in the PM coupler and PSC is eliminated by the EOM. In the returning light, leakage due to the EOM is eliminated by the PSC.

3.8.2. ACCURATE SPLICING OF THE PMF

Initial alignment is performed by taping each PMF segment to a rod extending from a rotational stage. Each stage was mounted on an upright microscope so that the tip of the fiber is against the microscope objective. An external visible light source was placed in proximity to the fiber axis away from the fiber tip to couple light in the fiber, and enable seeing the fiber section. Figure 3.11 shows the tip of a PMF viewed using the microscope.

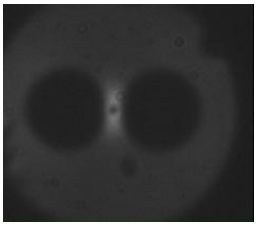

Figure 3.11 The tip of PMF as viewed under the microscope.

Accurate PMF splicing is usually accomplished by special PMF splicer with built-in rotational stages to align the splice angel. Due to availability, we used a SMF splicer (FSM-40S, Fujikura) and built an external apparatus with manually-rotated stages, see Figure 3.12. Fine alignment is performed by briefly lifting one of the splicer's internal fasteners, and slightly rotating the corresponding fiber segment.

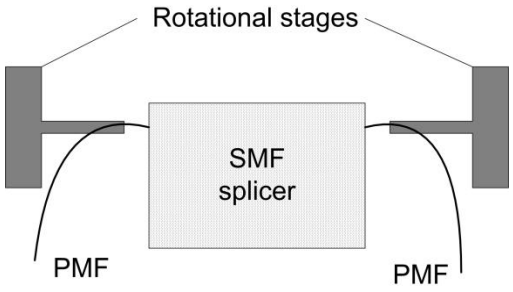

Figure 3.12 The apparatus used for accurate PMF splicing.

Fine alignment of the splice angle was accomplished by two to four rounds of splicing. PMF segments were first roughly spliced as described above. While the A-line is scanned and displayed in real-time, the splices were then broken and re-spliced one at a time. The broken segments were placed in the splicer after rough microscope alignment; and the two fiber tips were brought together until the A-line appears. One of the fiber segments was finely rotated, and the segments were re-spliced when the corresponding ghost line(s) diminish. These steps were repeated for every splice until all ghost lines are minimized. We measured splices loss between 0.1

and 1.2 dB, regardless of the splice angle and the fiber types (Panda to Panda, or Panda to the EOM's Bowtie).

3.8.3. Unequal Losses in the Reference Arm

Another design concern is the unequal transmission loss of the orthogonal modes in the reference arm. Losses in the PSC and EOM for the polarization channels can be unequal. The ratio of the fringe amplitudes when the sample light is equally split between the **S** and **X** channels was measured 0.88. To avoid pertaining errors, the interference signals I_s and I_f were rescaled accordingly.

3.8.4. External Effects

PMF maintains the polarization state of light in its fast and slow channels. Reflectivity and retardance images are therefore insensitive to external perturbations. The phase offset between the channels, however, changes with temperature or stress. As a result, the offset in the relative optical axis orientation image, φ_o, can be disturbed due to external effects. To minimize this influence, the EOM, PM coupler, PSC, and most of the PMF are insulated in a polystyrene enclosure. One can see that the image in Figure 3.10 (c) does not suffer a change in φ_o during the four-second acquisition time while the sample arm fiber is not disturbed. Since light between the reference arm's 0º and 90º splices, and the RSOD propagates in the slow axis, perturbations on the exposed fiber of the reference arm do not alter φ_o.

3.9 Conclusion

We presented the first PMF-based PSOCT system capable of imaging biological tissues. Simultaneous acquisition of two channels yields two complex measurements, sufficient to reconstruct polarization-diversity reflectivity, retardance, and optical axis orientation information with a single depth scan. Single detector imaging is enabled by frequency multiplexing the

orthogonal channels. Accuracy and imaging characteristics of the new single detector TD system were demonstrated similar to equivalent dual detector detection. The design eliminates ghost images in the imaging range, and allows imaging sample reflectivity with high dynamic range. The PMF-based interferometer maintains a circularly-polarized illumination of the sample, which enables imaging the retardance of the sample regardless of its angular orientation, and mapping of the optical axis orientation.

CHAPTER 4
SENSITIVE MEASUREMENT OF FARADAY ROTATION IN REFLECTION MODE[14]

The interferometer presented in the previous chapter exhibits very low differential-phase noise level for the cross-coupled channels. In this chapter, the system is slightly modified to measure Faraday rotation in clear media and tissue-mimicking phantoms. The PMF-based PSLCI illuminates the sample with two decorrelated and oppositely-polarized circular polarizations, and calculates Faraday rotation from the phase difference of light reflected from the sample. This approach is capable of measuring Faraday rotation in reflection mode with a single measurement and a small field-depth factor, making the system potentially applicable for biological measurements. We demonstrate system sensitivity of 0.31 minutes of arc, and measurements of Faraday rotation in clear and turbid liquids.

---

[14] Parts of the content of this chapter was published in the following peer-reviewed article:

- Muhammad K. Al-Qaisi, Hui Wang, and Taner Akkin, "Measurement of Faraday rotation using phase-sensitive low-coherence interferometry," Applied Optics 48, 5829-5833 (2009)

4.1 INTRODUCTION

Faraday Effect is a magneto-optical phenomenon that implies rotation of a plane of light polarization in a medium influenced by a magnetic field parallel to the propagation axis. Faraday rotation (Θ) is proportional to the magnetic field intensity (*B*) along the propagation axis, the length of the magneto-optical interaction path (**d**), and Verdet constant (*V*) of the material.

$$\Theta = VB\mathbf{d} \qquad \textbf{4.1}$$

Faraday effect has been employed in manufacturing optical isolators, and was proposed for making high-speed fiber polarization controllers [52], glucose sensors [53], electrical current sensors [54, 55], and real-time position sensor for interventional MRI [56]. Faraday rotation is a nonreciprocal phenomenon. This means that the angle of rotation is independent from the direction of the magnetic field along the propagation axis. A theoretical study has proposed that larger Faraday rotations will be measured in tissues when photons are trapped in multiple scattering events [57]; this would yields accurate measurement of the increase of the propagation path due to scattering.

Verdet constant is wavelength and temperature dependent. The constant is empirically-determined by a direct measurement of the angle of rotation of a linear polarization state in a medium with known **d** and *B*. Since Verdet constant is usually a small quantity, a high field-depth factor (*B***d**) [57-61], or extensive averaging [62], is required to accomplish a measurable rotation. In [60, 61], a very strong magnetic field (7 to 41 T) was applied to measure the rotation in samples on the order of a few centimeters. In a study to measure Verdet constant in gases and vapors [58], twenty meters of sample length was employed. Thus, design complications emerge from the large sample size, the stray effect of high magnetic field intensities generated by large electro-magnets, and from the hysteresis exhibited by electromagnetic circuitry [63].

In the following sections, we utilize the PMF-based PS interferometer presented in the previous chapter for sensitive measurement of Faraday rotation in small samples, and under the influence of small magnetic field. The PSLCI calculates Faraday rotation from the differential-phase between two decorrelated and oppositely-polarized circular polarization states. Because the cross-coupled polarization states simultaneously travel the same round-trip in each of the sample and reference arms, the technique exhibits a superior phase sensitivity to detect minute amounts of Faraday rotation. Verdet constant is measured of various clear and turbid liquids at 857 nm with a small $B\mathbf{d}$ factor.

4.2 CONCEPT OF THE MEASUREMENT

A linear polarization state can be represented by two oppositely-polarized circular polarizations; and the rotation of the linear state is equivalent to half of the phase shift between the circular states. Under the influence of a magnetic field, the difference between dextrorotary and levorotary refractive indices changes due to Faraday rotation.

This relation is clarified in the following discussion. Any linear polarization state can be describes as

$$\mathrm{L} = \begin{bmatrix} 1 \\ 0 \end{bmatrix} \tag{4.2}$$

If the reference axes *x* and *y*, described in Section 2.4, are rotated so that *x* is parallel to the polarization state. Using the rotation matrix $\mathbb{R}(\Theta)$ where Θ is the angle of rotation, the rotated vector can be written as

$$\mathrm{L}_{\Theta} = \mathbb{R}(\Theta)\begin{bmatrix} 1 \\ 0 \end{bmatrix} = \begin{bmatrix} \cos(\Theta) & -\sin(\Theta) \\ \sin(\Theta) & \cos(\Theta) \end{bmatrix}\begin{bmatrix} 1 \\ 0 \end{bmatrix} \tag{4.3}$$

$$\mathrm{L}_\Theta = \begin{bmatrix}\cos(\Theta)\\ \sin(\Theta)\end{bmatrix} = \frac{1}{2}\begin{bmatrix} e^{i\Theta} + e^{-i\Theta} \\ -ie^{i\Theta} + ie^{-i\Theta}\end{bmatrix} \quad \textbf{4.4}$$

And finally

$$\mathrm{L}_\Theta = \frac{1}{\sqrt{2}}\left(e^{i\Theta}\frac{1}{\sqrt{2}}\begin{bmatrix}1\\ -i\end{bmatrix} + e^{-i\Theta}\frac{1}{\sqrt{2}}\begin{bmatrix}1\\ i\end{bmatrix}\right) = \frac{1}{\sqrt{2}}\left(e^{i\Theta}\mathrm{C}_\mathrm{L} + e^{-i\Theta}\mathrm{C}_\mathrm{R}\right) \quad \textbf{4.5}$$

where C_L and C_R are left and right circular polarization states, respectively. This shows that Faraday rotation is expressed as a rotation of a linear polarization state, or a phase shift between two oppositely-polarized circular states. The phase difference between the two circular states, $\Delta\varphi$, is in fact twice the value of Faraday rotation

$$\Theta = \frac{\Delta\varphi}{2} \quad \textbf{4.6}$$

An alternative approach to describe this relation can be found in [64 (pp 26-30)]. Phase-based measurements are usually more sensitive than intensity-based ones. Thus, a more sensitive way of measuring Faraday rotation is attained by a differential-phase technique utilizing oppositely-polarized states.

Similar to Faraday rotation, the circular polarization state is nonreciprocal. The direction of circular polarization inverts when light is reflected. In other words, light with right circular polarization has left circular polarization after reflection, and vice versa. Therefore, the phase shift between two oppositely polarized states due to Faraday rotation doubles after propagating the same path in the opposite direction. In contrast, circular birefringence due to optical activity cancels out in the second pass. This enables measuring Faraday rotation in reflection mode, without interference from the optical activity.

4.3 METHOD

4.3.1. HARDWARE SETUP

The PMF-based system described in CHAPTER 3 is modified for the measurement, see Figure 4.1. A 1 mW SLD with $\Delta\lambda$ = 20 nm, and λ_o = 857 nm illuminates the interferometer (Superlum, Ireland). Unlike the system in CHAPTER 3, the linearly-polarized light transmitted through the free-space isolator is aligned at 45° with respect to the orthogonal channels of the PMF. The PM fiber segment in the input, due to its birefringence, unequally delays the polarization components propagating in its fast and slow channels. One beat length of propagation in the PMF introduces a full wavelength lag between the channels. The beat length for Corning's PM850 is about 2 mm; therefore, after passing a few centimeters of the fiber, the lag becomes longer than the coherence length of the source making the light in PMF channels decorrelated. The 2×2 PM coupler directs 30% and 70% of the incoming light into the sample and reference arms, respectively.

In the sample arm, a quarter-wave plate oriented at 45˚ with respect to the slow channel of the PMF transmits oppositely polarized circular polarization states. A 30 mm achromatic lens focuses the beam of 200 μW onto a sample. Permanent magnets with opposite polarizations pointing up are fastened to the disk underneath the sample. When the disk rotates, the alteration of the magnetic field results in an alternating phase shift between the oppositely-polarized states due to Faraday effect. In non-birefringent samples, light returning from the sample passes through the quarter-wave plate a second time, and the original polarization states are cross-coupled into the orthogonal channels of the PMF. The cross-coupled terms in the sample arm are denoted $\mathbf{X_f}$ for light cross-coupled in the fast channels of the PMF, and $\mathbf{X_s}$ for light at the slow channel. Because the cross-coupled terms propagate the same round-trip paths, there is no time delay between $\mathbf{X_f}$ and $\mathbf{X_s}$ at the PM coupler.

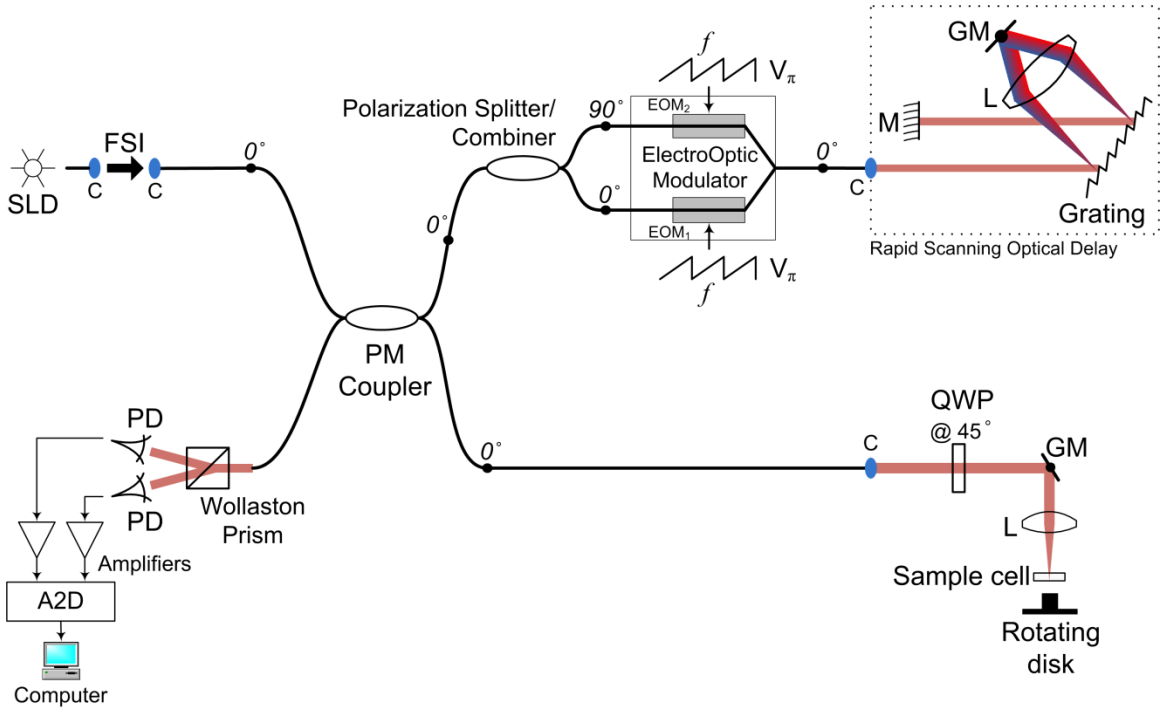

Figure 4.1 Schematic diagram of the PMF-based PSLCI configured for measuring minute Faraday rotation. SLD – superluminscent diode, FSI – free-space isolator, PM – polarization maintaining, PSC – polarization splitter/combiner, EOM – electrooptics modulator, L – lens, GM – galvanometer mirror, M – mirror, QWP – quarter-wave plate, PD – photodetector (the amplifiers are built-in), and A2D – analog to digital converter. All fibers are PMF.

In the reference arm, the polarization states are separated by means of the PSC. The modulating axis of the EOM is aligned with the slow channel of the PM fiber; therefore, light in the fast channel is coupled into the slow channel by a 90˚ splice. The two channels are modulated by a sawtooth waveform with voltage amplitude V_π and frequency f, then combined in the Y-connection of the modulator. Between the modulator and the RSOD, light continues propagating in the slow channel. The RSOD compensates for the dispersion mismatch between the reference and sample arms, and it can be scanned to locate the structures of a sample along a depth profile (see Sections 3.4.3 and 3.4.4). In the return path, light indiscriminately split at the Y-connection of the modulator. As a result, cross-coupled components are created at the same weight of the original ones, and all are modulated once more resulting in a full wave (2π) modulation. After

modulation, light from the two fibers recombines in the PSC. On the reference arm's end of the PM coupler, two original term **f** and **s**, and two cross-coupled terms, $\mathbf{x_f}$ and $\mathbf{x_s}$ are observed. Similar to the sample arm, the there is no time delay between $\mathbf{x_f}$ and $\mathbf{x_s}$. Because **f** and **s** travel different optical paths, **f** arrives to the PM coupler earlier than **s**.

In the PM coupler, the cross-coupled polarization states in the sample arm interfere with the corresponding modes of the reference arm. In contrast to the frequency modulation scheme for PSOCT imaging in CHAPTER 3, all polarization modes are modulated at the same frequency. Therefore, a dual-detector setup is utilized. A Wollaston prism (Karl Lambrecht Corp., Illinois) in the detection arm separates the two orthogonally polarized interference patterns, and diverts them onto two photodetectors.

Figure 4.2 illustrates the polarization components at the sample and reference beams, and the corresponding interference patterns. The coherence functions of the cross-coupled terms, I_{xs} and I_{xf}, occur simultaneously. The cross-coupled components travel the same round-trip paths; therefore, better common-mode noise rejection is expected when using the cross-coupled terms instead of the original, I_{ss} and I_{ff}. The original coherence functions can be used by realigning the coherence functions (as in Section 3.4.2), and inverting one of the modulating sawtooth signals to modulate I_{xs} and I_{xf} at zero Hz. Experimental noise analysis (similar to the one introduced Section 4.4) shows that the cross-coupled terms yield an order of magnitude improved SNR, therefore, the cross-coupled terms are used for measurement.

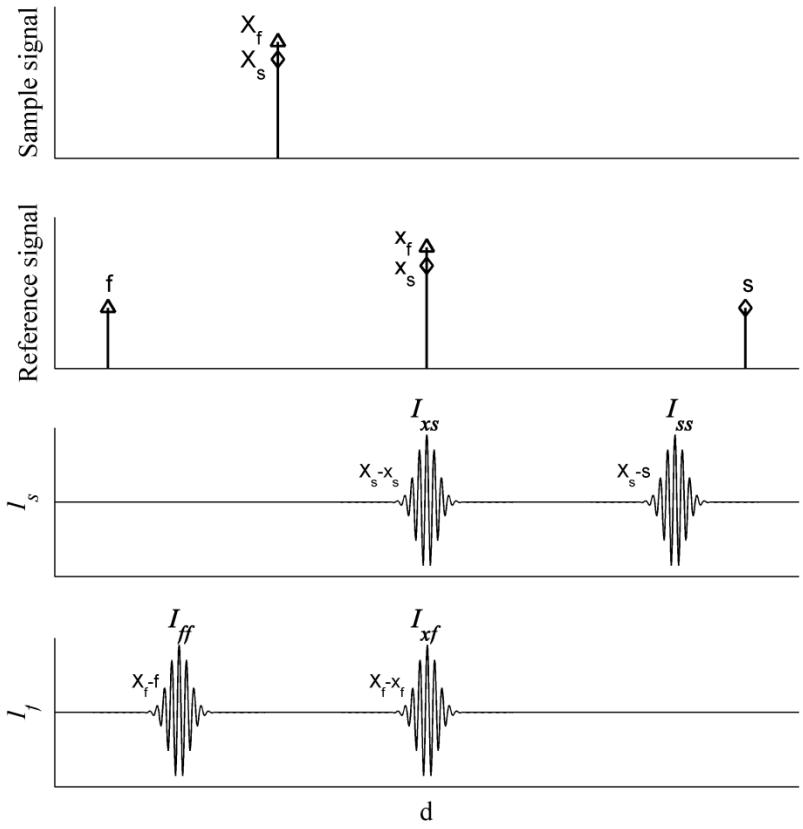

Figure 4.2 The sample beam only has cross-coupled terms, whereas the reference beam has four components, two cross-coupled and two original. The coherence functions detected on the slow and fast channels of the detection arm are shown, and the cross-coupled terms are inherently aligned.

The QWP is aligned at 45º by maximizing I_{xs} and I_{xf} when a non-birefringent reflector is placed as a sample (similar to Section 3.6.1). Dispersion compensation is performed as described in Section 3.4.3. Contrary to the case therein, the cross-coupled channels are similar, and dispersion difference is compensated for both of them at the same RSOD setup.

4.3.2. MATHEMATICAL FORMULATION

To describe polarization transformations in the sample path using Jones calculus, we consider the definition in Equation 3.3 where the slow and fast axes of the PMF are parallel to the

first and second elements in Jones vector, respectively. The polarization state of light coupled into the sample arm, E_{sample}, for any polarization state transmitted from the sample fiber, E_{in}, can be written as

$$E_{sample} = J(\lambda/4, 45^{\circ}).J_{sample}.J(\lambda/4, 45^{\circ}).E_{in} \quad \textbf{4.7}$$

where J_{sample} stands for the Jones matrix of the sample.

Using Equation 3.6, Jones matrix of a QWP oriented at 45˚ with respect to the slow axis of the fiber can be written as

$$J(\lambda/4, 45^{\circ}) = \frac{1}{\sqrt{2}}\begin{bmatrix} 1 & i \\ i & 1 \end{bmatrix} \quad \textbf{4.8}$$

Two equal and orthogonal components are transmitted from the sample arm fiber. The two decorrelated components can be treated individually. Therefore, light transmitted into the free-space of the sample arm is written as

$$E_{in} = \left[\!\!\left[\begin{matrix} 1 \\ 0 \end{matrix}\right]\!\!\right] + \left[\!\!\left[\begin{matrix} 0 \\ 1 \end{matrix}\right]\!\!\right] \quad \textbf{4.9}$$

where the double-lined brackets indicate that the two channels are decorrelated.

Using Equations 4.8 and 4.9, the term $J(\lambda/4, 45^{\circ}).E_{in}$ in Equation 4.7 can be written as

$$J(\lambda/4, 45^{\circ}).E_{in} = \frac{1}{\sqrt{2}}\left[\!\!\left[\begin{matrix} 1 \\ i \end{matrix}\right]\!\!\right] + \frac{1}{\sqrt{2}}\left[\!\!\left[\begin{matrix} i \\ 1 \end{matrix}\right]\!\!\right] \quad \textbf{4.10}$$

which are right-hand and left-hand decorrelated circular polarization states. The second term is leading the first by 90º; hence, Equation 4.10 can be written as

$$J(\lambda/4\,,45^{\circ}).E_{in} = \frac{1}{\sqrt{2}}\begin{bmatrix}1\\ i\end{bmatrix} + \frac{1}{\sqrt{2}}\begin{bmatrix}1\\ -i\end{bmatrix} e^{i\frac{\pi}{2}} \quad \textbf{4.11}$$

Due to Faraday rotation, each of the two terms in Equation 4.11 arephase-shifted by -Θ and Θ respectively. Thus, J_{sample} is an identity matrix multiplied by exp(-*i*Θ) for the first term in Equation 4.11, and exp(*i*Θ) for the second term of the equation. Now solving Equation 4.7 yields

$$E_{in} = \begin{bmatrix}0\\ 1\end{bmatrix}\exp(-i\Theta) + \begin{bmatrix}1\\ 0\end{bmatrix}\exp\big(i(\Theta+\pi)\big) \quad \textbf{4.12}$$

This mean that the original polarization states transmitted from the sample PMF are cross-coupled, and Faraday rotation is modulated on the phase difference between the two channels. The 180º phase shift is due to double-passing the QWP.

Considering a single reflector in the sample arm, Equation 2.3 can be used to describe the signals captured by the photodetectors. Because we are only interested in the cross coupled terms, the following expressions will be limited to describing them

$$I_{xs}(\tau) = I_o\sqrt{R}\cos[2\pi f\tau - \Theta].\exp[-(\alpha\tau)^2] \quad \textbf{4.13}$$

$$I_{xf}(\tau) = I_o\sqrt{R}\cos[2\pi f\tau + \Theta + \varphi_o + \pi].\exp[-(\alpha\tau)^2] \quad \textbf{4.14}$$

where I_{xs} and I_{xf} are the cross-coupled interference patterns detected on the slow and the fast channels of the detection arm, respectively. I_o is a constant, R is the reflectivity of the sample surface, α is a constant related to the source coherence function, f is the modulation frequency, τ is the time delay mismatch between the sample and reference arm, Θ is the phase delay due to Faraday rotation, and φ_o is a constant phase offset described in Section 3.5.2.

4.3.3. LCI MEASUREMENT

In LCI measurements, the signal of interest is limited to the cosinusoidal fringes. The envelope of the coherence functions, $\exp[-(\alpha\tau)^2]$, does not carry important information. The system is however aligned to maximize the signal by operating at $\tau \approx 0$. This is accomplished by manually aligning the length of the reference arm to match the sample arm.

The scanning mechanism of one of the channels is illustrated in Figure 4.3. With a stationary RSOD mirror, the reference arm length is scanned by the periodic phase delay introduced by the EOM. Figure 4.3 (a) shows the double-pass equivalent of the sawtooth EOM drive, $2V_{EOM}$, which has a maximum of $2V_{\pi}$. Now recall Equation 2.2, the modulation of the original coherence function are described by $\cos(2\pi\upsilon_o\tau)$, which means that the 2π phase delay introduced by the EOM scans one cycle of the term $\cos(2\pi\upsilon_o\tau)$. Figure 4.3 (b) shows the coherence function centered at $\tau = 0$ and scanned by the sawtooth signal with a period $1/f$. The interference pattern on the detection arm of the interferometer is shown in Figure 4.3 (c).

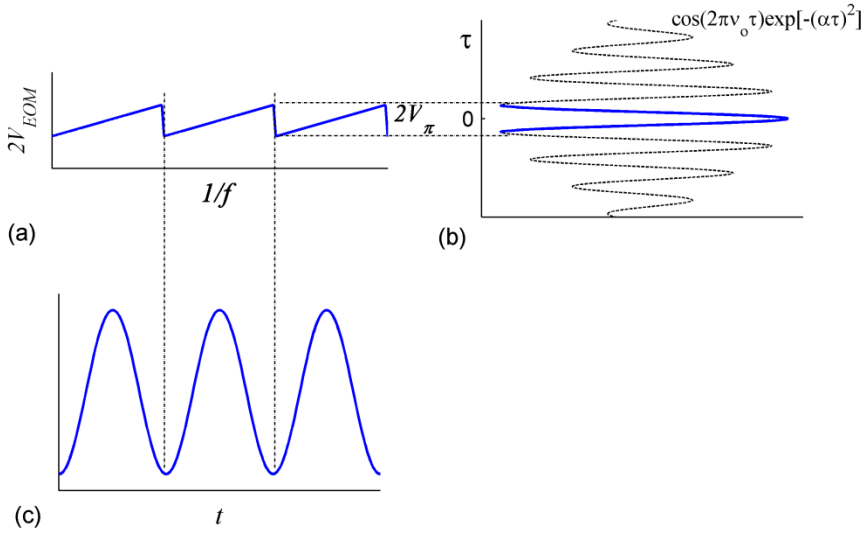

Figure 4.3 Illustration of the modulation scheme in the PMF-based PSLCI. (a) The EOM drive in double-pass, (b) one wavelength is scanned in every drive period $1/f$, and (c) the interference pattern on one output of the PSLCI.

According to the discussion above, the detected signals in Equations 4.13 and 4.14 can be rewritten as

$$I_{xs}(t) = I_o\sqrt{R}\cos[2\pi ft - \Theta] \quad \textbf{4.15}$$

$$I_{xf}(t) = I_o\sqrt{R}\cos[2\pi ft + \Theta + \varphi_o + \pi] = -I_o\sqrt{R}\cos[2\pi ft + \Theta + \varphi_o] \quad \textbf{4.16}$$

Note that the time index t has replaced the time delay τ, and that the two cosine functions, when $\varphi_o = 0$ and no Faraday rotation is induced, are a 180° out of phase.

4.3.4. Data Acquisition and Signal Processing

The signals are modulated at f = 2 kHz. The fringes on each channel are captured, amplified and band-pass filtered in the analog domain (2001, New Focus, California). The amplifier gain is set to 3×10^3 for each channel. The modulation frequency is Doppler-shifted due to vibrations while the magnets are rotating. Therefore, the analog bandwidth was set wide at 10 Hz to 10 kHz to avoid distorting the signal. The analog signals are digitized by a 12-bit analog to digital converter (PCI 6110, National Instruments, Texas) at a rate of 100 kS/s. This yields 50 points/fringe, enough for accurate Hilbert transform-based demodulation. The fringe signals are then band-pass filtered at 250 Hz bandwidth in the digital domain using forward and reverse filtering to avoid phase distortions.

Phase information on each channel is calculated as the angle between the fringe signal and its Hilbert transform as

$$\varphi_{xs} = \text{atan}\left[\frac{\mathcal{H}\{I_{xs}\}}{I_s}\right] = 2\pi ft - \Theta \quad \textbf{4.17}$$

$$\varphi_{xf} = \text{atan}\left[\frac{\mathcal{H}\{I_{xf}\}}{I_x}\right] = 2\pi ft + \Theta \quad \textbf{4.18}$$

And Faraday rotation in the sample is

$$\Theta = \frac{\varphi_{xf} - \varphi_{xs}}{2} = \frac{\Delta\varphi}{2} \qquad \textbf{4.19}$$

4.4 RESULTS

4.4.1. PHASE SENSITIVITY

In order to evaluate the interferometer's common-mode noise rejection, interferometric fringes created by the phase modulator were recorded when a glass wedge is placed in the sample arm, and without scanning the galvanometer mirror in the RSOD. Figure 4.4 (a) shows a large common-mode noise present on the phases, φ_{xs} and φ_{xf}, with noise standard deviation of 950 minutes of arc. The $2\pi ft$ terms are subtracted from the data shown in Figure 4.4 (a). The differential-phase measurement $\Delta\varphi$ is overlaid on the same plot and multiplied by 100 for scaling. The standard deviation $\Delta\varphi$ is 0.62 minutes of arc; yielding a common-mode noise rejection of 32 dB. According to Equation 4.19, this corresponds to 0.31 minutes of arc sensitivity to Faraday rotation. The histogram in Figure 4.4 (b) shows the probability distribution of $\Delta\varphi$ in (a).

4.4.2. FARADAY ROTATION IN CLEAR LIQUIDS

To measure the Faraday rotation in small volumes of liquids, we made a sample cell from two parallel microscope slides separated by 3 mm spacers. The cell was filled with a sample fluid and data was recorded from the reflection of the top surface of the bottom glass. Three rods were fastened to a rotating disk with 120˚ angular separation and placed underneath the sample, see Figure 4.5. One of the rods is unmagnetized, and two are cylindrical sintered NdFeB magnets (B_r = 12.6 kG, 1" thickness, 0.25" diameter) (K&J Magnetics Inc., Pennsylvania) with opposite poles pointing upward. The disk rotates at a controlled speed of 30 rotations/second.

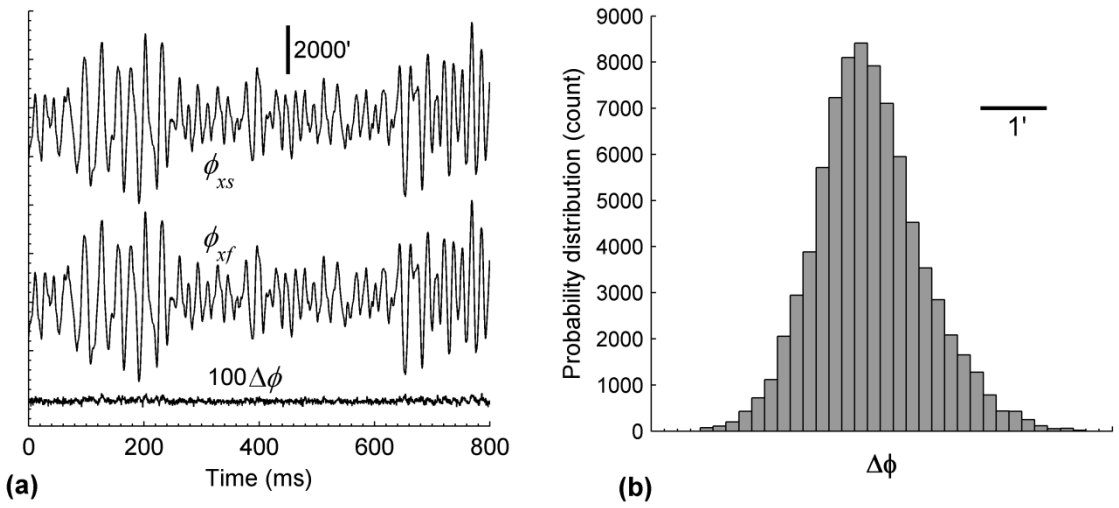

Figure 4.4 (a) Phase information on the two channels calculated for a glass reflector as a sample. The phase terms have large common-mode noise component which is largely rejected in the differential-phase measurement. The differential phase is multiplied by 100 for comparison. (b) The probability distribution of $\Delta\varphi$.

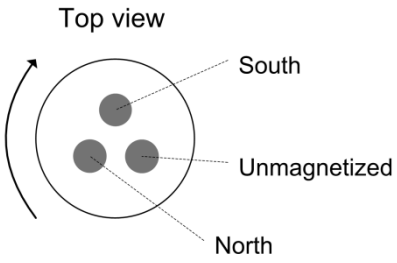

Figure 4.5 Two magnets with opposite poles pointing up are placed in on top of the rotating disk. An unmagnetized rod is added for balance.

Figure 4.6 (a) shows the measured Faraday rotation when the cell is filled with pure de-ionized (DI) water for three consecutive cycles of the disk rotation. The upward and downward deflections of Θ are due to the alternating magnetic field. The measurement shows Faraday rotation due to DI water in the sample cell, and the top glass of the cell. To remove the stray effect of the top glass, we interrogated the bottom surface of the upper glass slide and found that the stray rotation accounts for 22% of the total rotation shown in Figure 4.6 (a), equivalent to 3.45'.

Θ_{pp} is defined as the peak to peak Faraday rotation in each cycle. With DI water filling the sample cell, Θ_{pp} was obtained from 75 consecutive rotations. The probability distribution of the measurements is shown in Figure 4.6 (b). Contrary to the distribution in Figure 4.4 (b), data in this distribution were collected while the disk is rotating. The standard deviation for the two data sets is similar, indicating the efficient rejection of the mechanical vibrations common to the two channels.

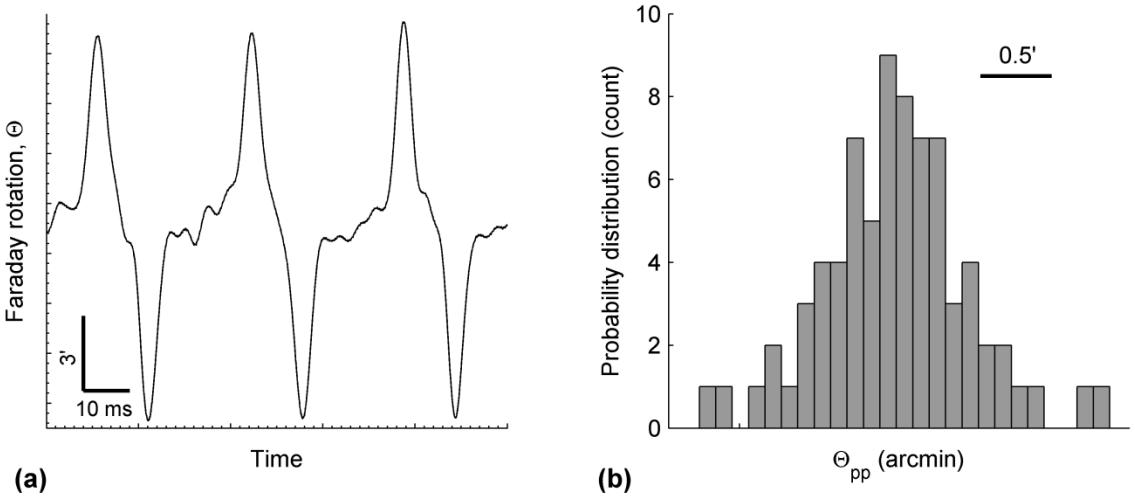

Figure 4.6 (a) Faraday rotation in pure DI water for three cycles of disk rotation. The stray effect of the top glass is not subtracted. (b) The probability distribution for 75 consecutive measurements.

The same measurement was repeated for acetone, isopropyl alcohol (IPA) and methanol. Residuals of the old fluid in the cell were flushed with the new sample. Figure 4.7 shows the mean values (dots) and standard deviations (bars) of the measurements. The figure shows that PMF-based PSLCI can differentiate between the samples based on Faraday rotation.

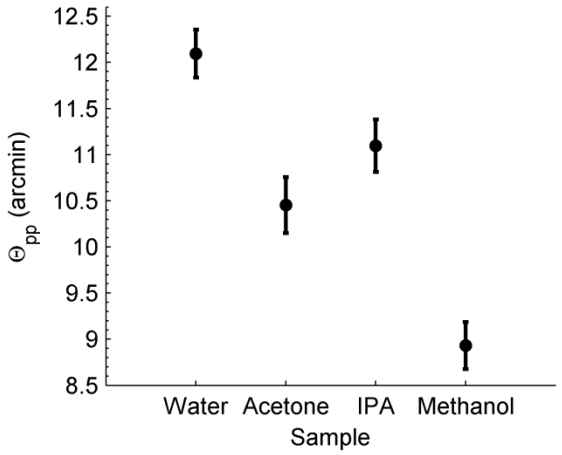

Figure 4.7 Means (dots) and standard deviations (bars) of seventy five measurements of Faraday rotation in various liquids.

Verdet constant for the samples is calculated from the measured Θ_{pp}. For this purpose, the magnetic field intensity was measured at multiple locations along the axis of the magnet. For each magnet, the average magnetic field intensity in the cell was measured as 2.07 kG. Considering that Θ_{pp} is evoked due to two magnets with opposite polarities, and light double-passing the inner cell thickness, values of Verdet constant of the sample liquids are calculated and listed in Table 4.1. for 857 nm at room temperature (22.7 ˚C).

Table 4.1 Verdet constant of various liquids measured at 857 nm at room temperature (22.7 °C)

Liquid	*Verdet constant*	
	$min.kG^{-1}.cm^{-1}$	$deg.kG^{-1}.cm^{-1}$
H_2O	4.8697	0.0812
Acetone	4.2081	0.0701
Isopropyl alcohol	4.4674	0.0745
Methanol	3.5952	0.0599

Verdet constant decays in an inverse power relation with the wavelength [61, 65]; it is usually reported at wavelengths lower than 800 nm. Curve fitting coefficients were however presented in [65] for DI water, acetone, and methanol; and results in Table 4.1 are in good agreement with the extrapolated values. Because Verdet constant is wavelength dependent, achromatic dispersion may influence the measurement. In this study, the spectrum of light source is narrow and falls within a low-slope region, achromatic dispersion is therefore neglected.

4.4.3. FARADAY ROTATION IN TURBID PHANTOMS

In this Section we demonstrate that Faraday rotation can be measured in scattering phantoms. Fat emulsion solutions of different concentrations are used to mimic the optical behavior of scattering samples [62, 66, 67]. Tissue phantoms are prepared by diluting intralipid solution in DI water; 0.2%, 0.4%, and 0.6% solution were prepared.

The setup was slightly modified for this measurement. Another light source (λ_o = 856 nm, $\Delta\lambda$ = 32 nm) (Exalos, Switzerland) now illuminates the sample with a maximum power of 1.1 mW. The depth of the sample cell is now 2.15 mm with a gold mirror placed in the bottom of the cell. An attenuator is now inserted in the sample arm to attenuate light reflected from low-scattering samples (DI water and 0.2% intralipid). And finally, because it is easier to process data with sinusoidal modulation, Faraday rotation is now sinusoidally-modulated by placing four magnets (B_r = 12.6 kG, 0.25" thickness, 0.75" diameter) (K&J Magnetics Inc., Pennsylvania) on the rotating disk with 90˚ angular spacing. See Figure 4.8.

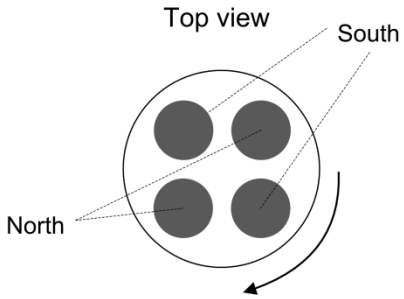

Figure 4.8 Sinusoidal modulation of Faraday rotation is accomplished by fastening four magnets with larger diameter on the rotating disk.

Faraday rotation is modulated at 30 Hz. The signal Θ is therefore band-pass filtered at 6 Hz to 140 Hz, and its amplitude, |Θ|, is calculated as

$$|\Theta| = \sqrt{\Theta^2 + (\mathcal{H}\{\Theta\})^2} \qquad \textbf{4.20}$$

Figure 4.9 illustrates the demodulation scheme using data collected from the 0.2% intralipid phantom. Because the scheme is based on Hilbert transform, the measurement is inherently insensitive to variations in the rotating disk speed. Fluctuations on |Θ| are due differences between the magnetic fields from the different magnets. Because the fluctuation pattern is repeatable, the peak Faraday rotation per cycle, Θ_p, is calculated as the average per cycle to avoid subsequent error.

One hundred and forty Θ_p measurements are acquired from DI water and the scattering phantoms. Figure 4.10 shows the means (dots) and standard deviations (bars) of the measurements after accounting for the stray effect of the cell. Since noise on the phase signal is inversely proportional with the SNR of the interferometric signal, see Section 2.3.4, lower light level reflected from the sample caused larger standard deviations for 0.4% and 0.6% Intralipid solutions. Data suggests that Faraday rotation in the given range of turbidity is not influenced by the number

of scattering events. After measuring the magnetic field, average Verdet constant for this data set is calculated as 4.95 $min.kG^{-1}.cm^{-1}$.

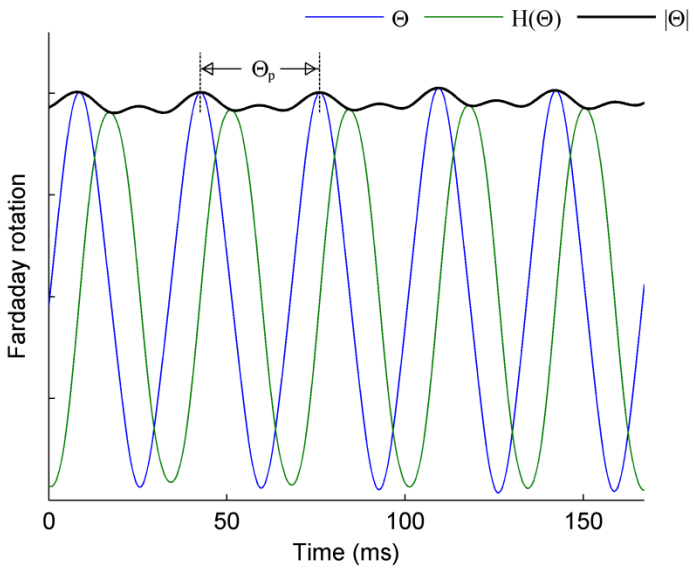

Figure 4.9 When Faraday rotation, Θ, is sinusoidally-modulated, Hilbert transform is used to calculate the amplitude |Θ|. The measurement Θ_p is averaged across each cycle to avoid errors pertaining to the variability in the magnetic field.

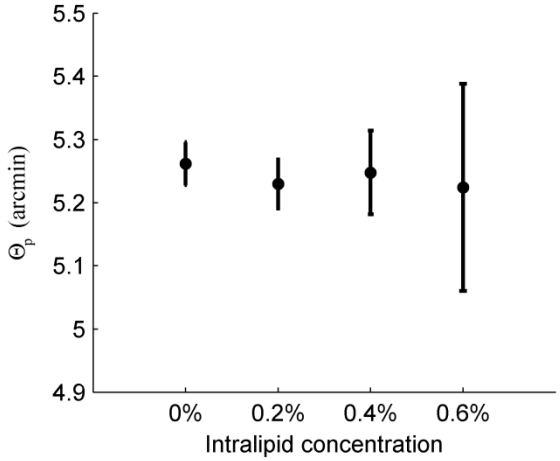

Figure 4.10 Means (dots) and standard deviations (bars) of 140 measurements of Faraday rotation in scattering phantoms.

4.5 Discussion and Future Guidelines

The new approach to measure Faraday rotation as the phase difference between two oppositely-polarized states demonstrates sensitivity levels superior to other methods in literature. Faraday rotation is measured with two orders of magnitude smaller $V\mathbf{d}$ factors. The technique can be employed to measure Verdet constant in the fields of material science and optical devices manufacturing. Opposed to conventional techniques, the new approach has the potential to be utilized in biomedical applications.

We are aware of one other study that measured Faraday rotation in scattering media based on direct measurement of the angle of rotation [62]. An average of thousand consecutive measurements was required to slightly resolve the rotation. Because the system indiscriminately measures all the light reflected from the sample, alterations on the incident linear polarization will falsely influence the measurement.

In contrast to the system in [62], the PMF-based PSLCI discriminates between the polarization states reflected from the sample, and only uses the signal on the cross-coupled channels to measure Faraday rotation. In birefringent samples, the components of the circular polarization states are altered, and only the cross-coupled components are used for the measurement. This means that the demonstrated measurement is immune to slight birefringence in the sample.

Little is reported about the magneto-optical properties of tissues. Because the common measurement techniques were not applicable to tissue imaging, one can not find information about Verdet constant in tissues. The reflection-mode measurement demonstrated here is potentially applicable to biomedical imaging. We have presented measurements in tissue mimicking

phantoms at 857 nm; and it is important to do future studies on the feasibility of using Faraday rotation for biological imaging or measurements.

Verdet constant is larger at lower wavelengths; therefore, working in the 800 nm imaging range is a good starting point for tissue imaging. Because FD OCT provides faster imaging, the PMF-based SD PS-OCT[15] we implemented will be utilized in future attempts to build on the outcome of this work. The measurement time is currently limited by the speed of alternating the magnetic field; faster modulation of Faraday rotation can be achieved by using electromagnets.

4.6 CONCLUSION

We have demonstrated a novel approach to measure Faraday rotation at two orders of magnitude lower $\boldsymbol{Bd}$ factors than common techniques. The differential-phase technique utilizes light reflected from the sample for the measurement. Using the PMF-based PSLCI, a single measurement is sufficient to measure Verdet constant in clear and turbid samples. The presented work demonstrates the feasibility to further investigate imaging of Faraday rotation in tissues.

[15] Hui Wang, Muhammad K. Al-Qaisi, and Taner Akkin, "Polarization-maintaining fiber based polarization-sensitive optical coherence tomography in spectral domain," Optics Letters 35, 154-156 (2010)

CHAPTER 5
BIREFRINGENCE IN UNMYELINATED NERVES[16]

A variety of optical properties, including birefringence, have been shown to exhibit transient changes associated with action potential propagation. Different optical properties, like intensity and birefringence, can be misinterpreted using the techniques currently in use. Better differentiation between the signals and understanding of its origin can be accomplished by employing new measurement approaches. We propose a differential-phase measurement of the retardance of nerves; the PMF-based PSLCI is modified to measure the phase shift between two orthogonal polarization states. The system demonstrates superior sensitivity of 10 pm, which is employed in attempts to achieve a non-contact optical measurement of neural activity in reflection mode by measuring transient retardance changes during action potential propagation.

---

[16] Parts of the content of this Chapter were published in the following peer-reviewed articles:

- Muhammad K. Al-Kaisi, David Landowne, and Taner Akkin, "Low coherence interferometer for sensing retardance change during neural activity," proceedings of IEEE EMBS 6318-6320, (2009)

5.1 INTRODUCTION

Action Potential (AP) propagation in nerve fibers is accompanied by temporary alterations in structural and optical properties of the fiber. The signs of neural activity, i.e. AP propagation, can be detected optically through changes in absorption, birefringence, optical rotation, fluorescence, light scattering, and volume changes [68]. Biochemical and structural changes contributing to these signals may include molecular reorientations in the membrane, influx and outflux of ions, and change in axon diameter.

Light scattering and birefringence changes during neural activity in nerve bundles from walking legs of crabs and squid giant axons were demonstrated [69]. Fluorescence, scattering and birefringence changes with nerve trunks from the legs of lobsters and spider crabs, and with squid fin nerve were also presented [70]. Most measurements reported in literature are based on crossed-polarizers setup. The optical setup employed for the measurement consist of a polarizer that transmits linearly polarized light at 45° with the nerve axis; and an analyzer that minimizes light transmitted on a detector. Crossed-polarizers setups measure relative light intensity change $\Delta I/I$ during AP propagation in transmission mode. Retardance change $\Delta\delta$ in nerves with low retardance δ can be calculated as [71]

$$\Delta\delta = 0.5\delta\frac{\Delta I}{I} \qquad \textbf{5.1}$$

From the data in [71], $\Delta\delta$ in the crab leg nerve is in the range 5.9 – 8.5 pm, and 0.2 – 0.25 pm at the edge of squid giant axon. Higher $\Delta\delta$ value, 37 pm, have been reported for pike olfactory nerve containing about 4 million axons with average diameter of 0.2 μm [72].

The measured signals indicate optical and structural changes in the functioning nerve; the techniques utilized for the studies, however, do not produce depth-resolved information about

neural activity. Further studies of the optical properties of activated nerves using new optical techniques are expected to enhance understanding of the underlying biochemical processes during neural activity.

Optical interferometry exhibits high sensitivity and operate in reflection-mode. It offers depth-resolved information with the use of low-coherent light sources. Because the light source and the detector are on the same side of the nerve, the interferometric techniques have the additional advantage of being less invasive than many other optical techniques.

In this chapter, we slightly modify the interferometer in CHAPTER 4 to measure minute amounts of linear birefringence to study the static and dynamic retardance of nerves. The differential phase measurement between simultaneously recorded orthogonal polarization channels yields superior sensitivity. Static retardance of various unmyelinated nerve models is imaged. Retardance change during nerve activity is calculated a little larger than the detection limit of the optimized system.

5.2 NERVE PREPARATION

5.2.1. DISSECTION AND RINGER SOLUTIONS

Different nerve models are used according to the season. $\Delta\delta$ for pike olfactory nerve is calculated from data in literature to be a few times larger than noise level of the interferometer (see Section 5.5.1). Fresh pikes are not available in cold seasons, and crustacean models are therefore used. Pike olfactory nerve is dissected from a freshly sacrificed northern pike under a dissection microscope as described in [72]; and the crustacean nerves are dissected using the pulling technique described in [73]. The two ends of the dissected nerve were tied with silk threads.

Ringer solutions are prepared to provide the appropriate environment for the nerves *ex vivo*. The solutions for pike [72], lobster [74], and crayfish nerve [75], were prepared by dissolving

the solutes listed in Table 5.1 water. The solutions were buffered at pH 6.8, 8, and 7.4, respectively.

Table 5.1 The solutes and their molar concentration in the species-specific Ringer solutions.

Solute	*Molar Concentration (mM)*		
	Pike	*Lobster*	*Crayfish*
NaCl	120	470	205.3
KCl	4	10	5.3
$CaCl_2$	11	10	13.5
$NaHCO_3$	3	--	--
Glucose	5	--	--
$MgCl_2$	--	350	2.5

In each experiment, the solution was oxygenated using an aerator with a bubbling tip, and the dissected nerve was conditioned by immersing it in the solution in the refrigerator. The nerve is then laid in the groove of the nerve chamber shown in Figure 5.1. We have found that about ten minutes of air bubbling and an hour of conditioning in the refrigerator are sufficient to extend the nerve life to up to a few hundred stimulations within one or two hours; similar lifetime was reported in [76].

5.2.2. THE NERVE CHAMBER AND ELECTRICAL STIMULATION

The chamber body is made from acrylic glass. Platinum electrodes are fixed to the body for electrical stimulation and recording. Based on experimental observations, the large reservoirs around the groove were made large to keep the nerve in contact with enough Ringer solution to

maintain its activity. Petroleum jelly is used to form an electrical insulator between the stimulating and the recording electrodes. A small amount of petroleum jelly was also added around the nerve between every electrode and the other. A microscope slide is laid on the chamber making sure there are no air bubbles in contact with the nerve. The optical measurement is taken from the nerve portion above the region labeled as optical window.

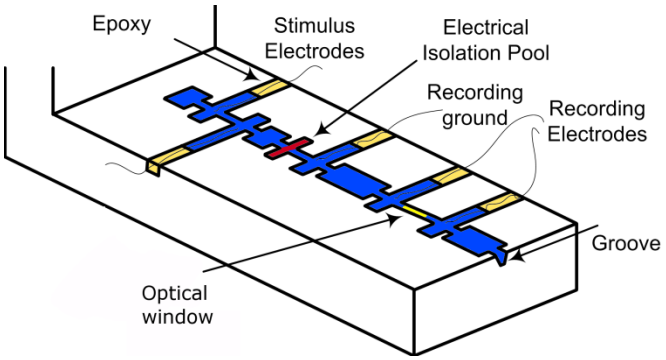

Figure 5.1 The nerve chamber. The dissected nerve is laid along the groove. The grove is filled with the appropriate solution. Direct conduction of the stimulating signal is prevented by filling the isolation pool with petroleum jelly. The preparation is covered with a microscope slide.

An isolated pulse stimulator was used to apply electrical pulses to stimulate the AP. The externally recorded compound AP was amplified by an AC differential amplifier, and recorded by a 12-bit data acquisition card simultaneously with the optical signals.

5.3 Evaluating the Nerve Preparation

5.3.1. Crossed-Polarizers Setup

To evaluate the process of nerve preparation[17], experiments to measure retardance changes in activated nerves both in transmission and reflection modes were launched using the crossed-

[17]The pike olfactory nerve preparation is most difficult amongst the preparations presented in this chapter. Preparations of the crustacean nerves are evaluated by the minimum stimulation current enough to initiate AP [76].

polarizers setup. Figure 5.2 shows the optical setup used in the experiment. A piece of glass is glued underneath the groove as the optical window indicated in Figure 5.1. The setup is illuminated by a 2 mW from a SLD with λ_o = 856 nm and $\Delta\lambda$ = 32 nm. Light enters a Wollaston prism at the prism's output angle; the prism transmits the light beam orthogonal to its facet with a linear polarization state. An achromatic lens with a focal length of 35 mm focuses the beam to a minimum spot size of 36 μm (see Equation B.2) on the glass window underneath the nerve. The nerve is placed at 45˚ with respect to the incoming polarization state. An analyzer is aligned behind the nerve to minimize the light intensity detected by a large area detector, D_T. Light backscattered/reflected from the nerve is collected by the same focusing lens and split into two orthogonal linear components by the Wollaston prism. The reflected cross-polarized component is detected by the detector D_R.

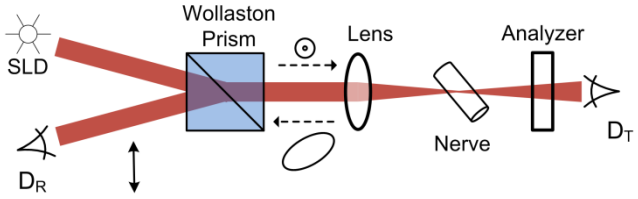

Figure 5.2 Optical setup used to measure cross-polarized light intensities during AP propagation. SLD: superluminescent diode, D_T: transmitted light detector, D_R: reflected light detector. Dotted arrows show the direction of light propagation labeled with the polarization state of light.

5.3.2. RESULTS

Figure 5.3 shows the compound AP (a), and $\Delta I/I$ in transmission (b) and reflection (c) geometries. A 5 ms, 2 mA electrical pulse is presented at the beginning of the recording. Fifty records are averaged in each trace to improve the signal to noise ratio. The traces have a bandwidth of 150 Hz. The minute intensity changes clearly correspond to the AP arrival to the optical measurement area. The transmission mode intensity change we measured is comparable to the value 1.7×10^{-3} reported in [72]. The $\Delta I/I$ measurement in reflection geometry, Figure 5.3 (c), is

smaller than that in transmission mode because the denominator *I* is larger. This is partially attributed to the fact that in reflection mode measurement, the analyzer (the Wollaston prism itself) does not eliminate the major axis of the ellipse reflected from the nerve. Reflection of the source light from the front surface of the Wollaston prism also increases *I*. The measurement shows that birefringence change during AP propagation can be measured even in reflection mode, and that the nerve is prepared appropriately.

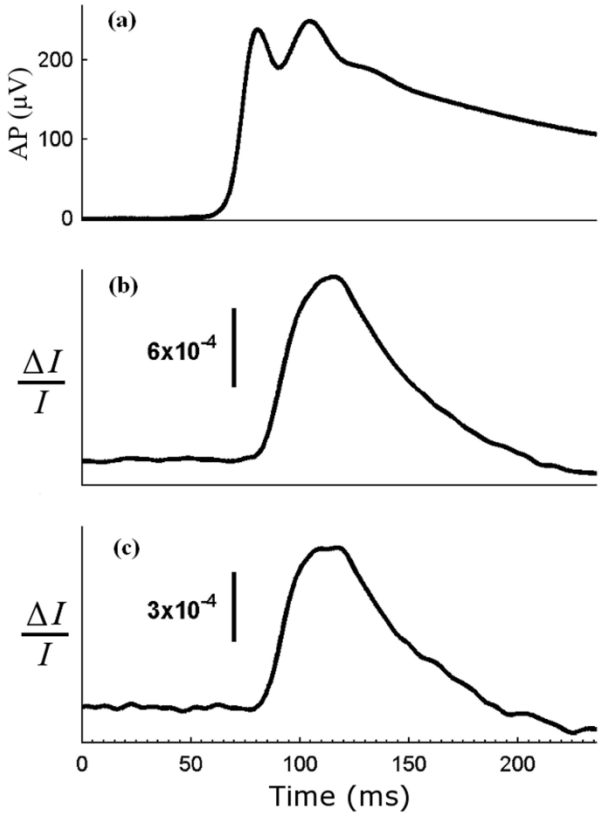

Figure 5.3 Measurement of neural activity in the olfactory pike nerve: compound AP (a), and cross-polarized intensity changes in transmission (b) and reflection (c) geometries.

5.4 PMF-BASED LCI FOR MEASUREMENT OF MINUTE LINEAR BIREFRINGENCE

The PMF-based interferometer is illustrated in Figure 5.4. The setup is largely similar to the one presented in CHAPTER 4; thus, only the slight modifications and the corresponding analysis are presented here. The input arm is illuminated by a SLD with an average power of 5 mW, λ_o of 856 nm, and $\Delta\lambda$ of 32 nm. The reference arm operation is described in section 4.3.1. A slightly different modulation approach is employed here: sawtooth signal with frequency f and amplitude $V_{2\pi}$ is applied only to EOM_2. The cross coupled channels I_{xs} and I_{xf} are therefore modulated at f, while I_{ss} and I_{ff} are modulated at zero and $2f$. This allows filtering the signal at f to avoid the influences of I_{ss} and I_{ff}, if any.

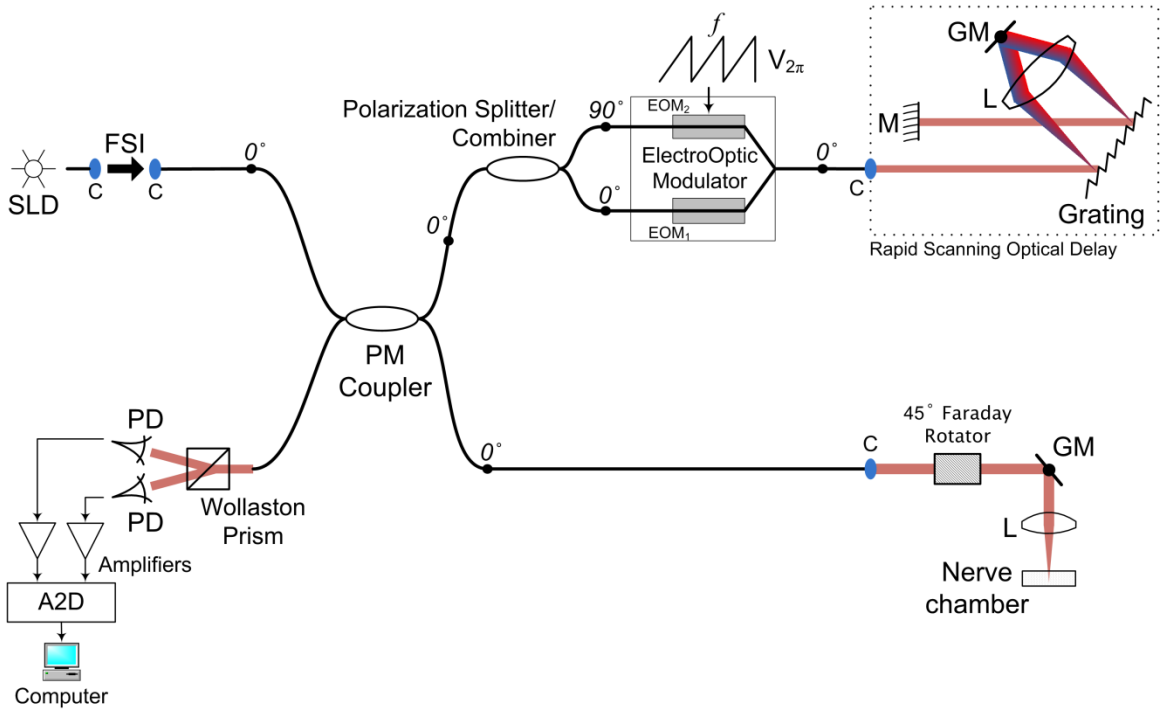

Figure 5.4 Schematic diagram of the PMF-based PSLCI configured for measuring minute linear birefringence. SLD – superluminescent diode, FSI – free-space isolator, G – grating, L – lens, M – mirror, GM – mirror on a galvanometer, PD – photodetector (the amplifiers are built-in), and A2D – analog to digital converter. All fibers are PMF.

In the sample arm, the linear orthogonal polarization states transmitted from the sample arm fiber are cross-coupled in the channels of the fiber after the second pass in a 45˚ Faraday rotator. Each polarization state is therefore rotated a total of 90˚ in double pass. The nerve axis is aligned with any of the incident polarization states so that its retardance is modulated on the phase difference between the two polarizations.

Light is focused on the reflector underneath the nerve. To increase the signal intensity reflected from the nerve and reduce the phase noise, a gold-plated mirror is fixed underneath the groove in the "optical window" of the nerve chamber. The reflected light interferes with the corresponding modes in the reference arm, and the interference fringes on the two cross-coupled channels are detected in the detection arm. More details are presented in Sections 4.3.1 and 4.3.4.

5.4.1. MATHEMATICAL FORMULATION

Jones calculus is applied to study light in the sample arm. We consider the definition in Equation 3.3 where the slow and fast axes of the PMF are parallel to the first and second elements in Jones vector, respectively. The polarization state of light coupled into the sample arm, E_{sample}, for any polarization state transmitted from the sample fiber, E_{in}, can be written as

$$E_{sample} = \mathbb{R}(45^{\circ}).J_{sample}.\mathbb{R}(45^{\circ}).E_{in} \quad \textbf{5.2}$$

where J_{sample} stands for the Jones matrix of the sample. The rotation matrix $\mathbb{R}(45^{o})$ is calculated using Equation 4.3.

Two equal and orthogonal components are transmitted from the sample arm fiber. The two decorrelated components can be treated individually. Therefore, light transmitted into the free-space of the sample arm is written as

$$E_{in} = \left[\!\left[\begin{matrix}1\\0\end{matrix}\right]\!\right] + \left[\!\left[\begin{matrix}0\\1\end{matrix}\right]\!\right] \quad \textbf{5.3}$$

where the double-lined brackets indicate that the two channels are decorrelated.

Using Equations 5.3, the term $\mathbb{R}(45^{\circ}).E_{in}$ in Equation 5.2 can be written as

$$\mathbb{R}(45^{\circ}).E_{in} = \frac{1}{\sqrt{2}}\left[\!\left[\begin{matrix}1\\1\end{matrix}\right]\!\right] + \frac{1}{\sqrt{2}}\left[\!\left[\begin{matrix}-1\\1\end{matrix}\right]\!\right] \quad \textbf{5.4}$$

which are two orthogonal decorrelated linear polarization states at 45° with respect to the slow axis of the PMF. The nerve axis is aligned with either of the polarization states transmitted from the Faraday rotator. Due to birefringence of the nerve, a phase shift between the two terms in Equation 5.4 is applied. Thus, after a double pass in the nerve, J_{sample} is an identity matrix multiplied by exp(-i2δ) for the first term in Equation 5.4, where δ is the phase retardance due to the birefringence of the nerve. Solving Equation 5.2 yields

$$E_{in} = \left[\!\left[\begin{matrix}0\\1\end{matrix}\right]\!\right] + \left[\!\left[\begin{matrix}1\\0\end{matrix}\right]\!\right]\exp(i2\delta) \quad \textbf{5.5}$$

This mean that the original polarization states transmitted from the sample PMF are cross-coupled, and the retardance of the nerve is modulated on the phase difference between the two channels.

Considering a single reflector in the sample arm, Equation 2.3 can be used to describe the signals captured by the photodetectors. Retardance is modulated on the phase of the cross coupled terms, and the following expressions are limited to describing them

$$I_{xs}(\tau) = I_o\sqrt{R}\cos[2\pi f\tau].\exp[-(\alpha\tau)^2] \quad \textbf{5.6}$$

$$I_{xf}(\tau) = I_o\sqrt{R}\cos[2\pi f\tau + \varphi_o + 2\delta].\exp[-(\alpha\tau)^2] \quad \textbf{5.7}$$

where I_{xs} and I_{xf} are the cross-coupled interference patterns detected on the slow and the fast channels of the detection arm, respectively. I_o is a constant, R is the reflectivity of the sample surface, α is a constant related to the coherence function of the source, f is the modulation frequency, τ is the time delay mismatch between the sample and reference arm, and φ_o is a constant phase offset described in Section 3.5.2. Contrary to the interference fringes detected in system in CHAPTER 4, the fringes detected in this setup are in phase when $\delta = 0$ and the offset φ_o is subtracted.

Because we are only interested in the cosinusoidal fringes in Equations 5.6 and 5.7, the reference arm is aligned so that $\tau = 0$ (see Section 4.3.3). The equations can therefore be rewritten as

$$I_{xs}(t) = I_o\sqrt{R}\cos[2\pi ft] \quad \textbf{5.8}$$

$$I_{xf}(t) = I_o\sqrt{R}\cos[2\pi ft + \varphi_o + 2\delta] \quad \textbf{5.9}$$

Note that the time index t has replaced the time delay τ.

5.4.2. Data Acquisition and Signal Processing

Fringes are modulated at f = 5 kHz, amplified 3×10^3 times, filtered at a bandwidth of 10 Hz to 10 kHz, then digitized using a 12-bit data acquisition card at 250 kS/s. Each cosinusoidal fringe therefore has 50 points, enough to calculate phase information on each channel as the angle between the fringe signal and its Hilbert transform

$$\varphi_{xs} = \text{atan}\left[\frac{\mathcal{H}\{I_{xs}\}}{I_s}\right] = 2\pi ft \quad \textbf{5.10}$$

$$\varphi_{xf} = \text{atan}\left[\frac{\mathcal{H}\{I_{xf}\}}{I_x}\right] = 2\pi ft + 2\delta + \varphi_o \quad \textbf{5.11}$$

And the single pass retardance of the nerve is calculated, neglecting the constant phase offset, as

$$\delta = \frac{\Delta\varphi}{2}\frac{\lambda_o}{2\pi} \quad \textbf{5.12}$$

5.4.3. LCI MEASUREMENT

Retardance is modulated on the cosinusoidal fringes and the envelope of the coherence functions, $\exp[-(\alpha\tau)^2]$, does not carry important information. The system is however aligned to $\tau \approx 0$ so that the amplitudes of the cosinusoidal fringes are maximized. This is accomplished by manually aligning the length of the reference arm to match the sample arm.

Phase sensitivity depends on the accuracy of the modulation of the interference fringes. Dispersion mismatch between the sample and reference arms must be accurately compensated to avoid chirping, which in turn results in a non-uniform modulation across the coherence function. Dispersion is compensated in the RSOD as described in Section 3.4.3 with a difference that the two channels, because similar, are compensated together here.

5.4.4. PRECISE ADJUSTMENT OF THE MODULATION

The EOM scans the coherence function a full wave when a sawtooth waveform with amplitude $V_{2\pi}$ is applied. Distortions and consequent higher harmonics are observed when the voltage amplitude is not precisely adjusted. After compensating for dispersion, and maximizing the amplitude of the interference fringes, the second harmonic of either the cosinusoidal fringes is minimized by adjusting the voltage of the sawtooth waveform applied to the EOM.

5.4.5. ADAPTIVE ALIGNMENT FOR IMPROVED LONG TERM STABILITY

Observing retardance change due to action potential propagation requires sensitivity on the order of tens of picometers; careful optimization of the system is therefore essential. Highest phase sensitivity is achieved when the amplitudes of the fringes are maximized; that is when the lengths of the sample and reference arms are matched, that is τ (or equivalently d) = 0. We have observed slow fluctuations on d probably due to thermal or mechanical relaxation; and severe degradation on the sensitivity of the retardance measurement when d diverges from zero. To demonstrate this effect, we have varied d and calculated the corresponding retardance. Figure 5.5 shows the calculated noise standard deviation of the retardance measurements as a function of d. The figure shows that 3 μm deviation from d = 0 degrades the retardance sensitivity at least three folds. Each single data point in Figure 5.5 is acquired and calculated as described in Section 5.5.

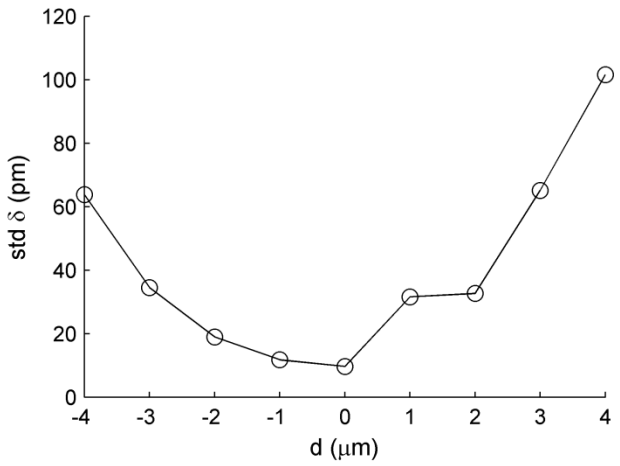

Figure 5.5 Lowest standard deviation of retardance noise is measured at the center of the coherence function. Slight deviation from perfect alignment is enough to severely degrade the phase sensitivity.

The measurement of AP itself is faster than the slow change in d. However, hundreds of recordings are usually acquired and averaged. This takes a few minutes and usually yields large noise levels due to large fluctuations in d. Improved long term stability is achieved by realigning the interferometer to d = 0 between consecutive measurements. This is accomplished by adjusting

the DC component in the sawtooth waveform applied to the EOM. Two independent DC signals are applied to EOM_1 and EOM_2 to find the maximum fringe amplitude. The total DC offset applied to the two modulators is ±10 V scanned with a step size of 1 V. The 20 V change enables the adjustment of d by about seven wavelengths, a little more than half of the coherence length of the source. Before every measurement, the DC level is scanned, and the DC offset that yields the highest fringe amplitude is selected. To avoid errors due noise, the recorded amplitudes across the scan are fitted to a quadratic curve, and the maximum is found from the curve not the original data. The entire adaptive adjustment procedure can be disabled in the acquisition software.

5.5 RESULTS

5.5.1. SYSTEM CHARACTERIZATION

A glass wedge is placed as a sample to evaluate the sensitivity of the system. Figure 5.6 (a) shows the noise floor of retardance data filtered using a low-pass bandwidth with a roll-off frequency at 1 kHz. The quantities δ_{xs} are δ_{xf} are single pass phase delays in nanometers calculated by multiplying φ_{xs} and φ_{xf} by $\lambda_o/4\pi$, respectively. Large common mode noise component is observed on δ_{xs} are δ_{xf} with 11.5 nm standard deviation of the noise. The differential phase measurement effectively rejects the common mode noise yielding a 30 dB common mode noise rejection; noise standard deviation on δ is measured as 12.5 ± 2.2 pm (nine samples). Theoretical phase noise is calculated using Equation 2.8 as 5.5 pm. This was calculated using the intensity SNR on I_{xs} which was measured as 1109 ± 330 (eight samples), slightly higher than that on I_{xf}. This shows that the differential phase measurement using the PMF-based PSLCI approaches the theoretical value. The slight difference between theoretical and measured sensitivity is attributed to residual thermal and mechanical noise. The Normal distribution of retardance noise is shown in Figure 5.6 (b).

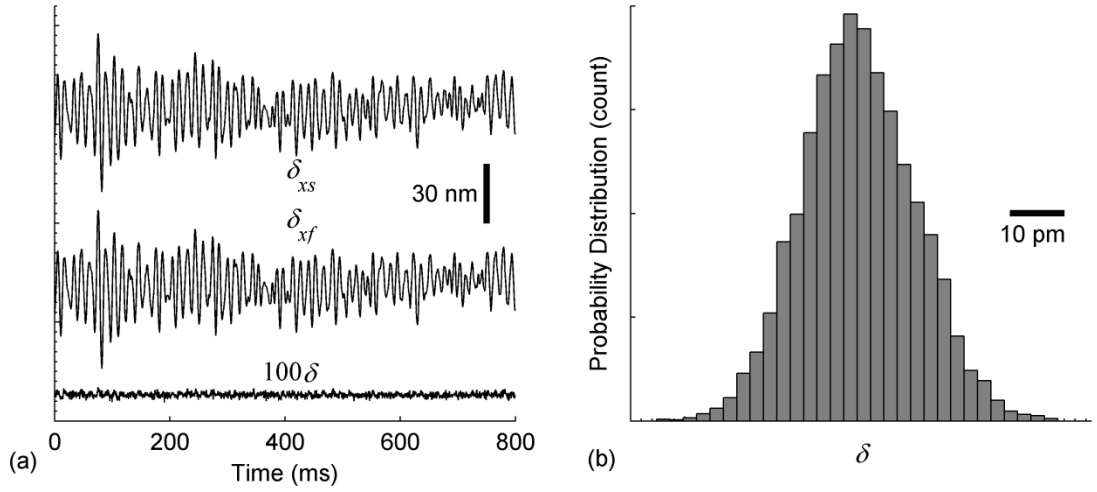

Figure 5.6 Phase information on the two channels calculated when a glass reflector is used as a sample. Phases of the two channels have a large common-mode noise component which is largely rejected in the differential-phase measurement. The differential phase is multiplied by 100 for comparison. (b) The probability distribution of δ.

The measurement of retardance change is demonstrated by adding a voltage-controlled variable retarder (VR) to the sample arm between Faraday rotator and the lens. The VR simulates an activated nerve by aligning it parallel to either of the polarization states transmitted from the Faraday rotator, and varying its retardance. Figure 5.7 shows the measured retardance changes when the applied voltage is stepped. The filtered data is also shown after applying a median filter. The figure demonstrated the system capability to measure retardance changes from the phase delay. The stimulated retardance change is in the range of that in the pike olfactory nerve.

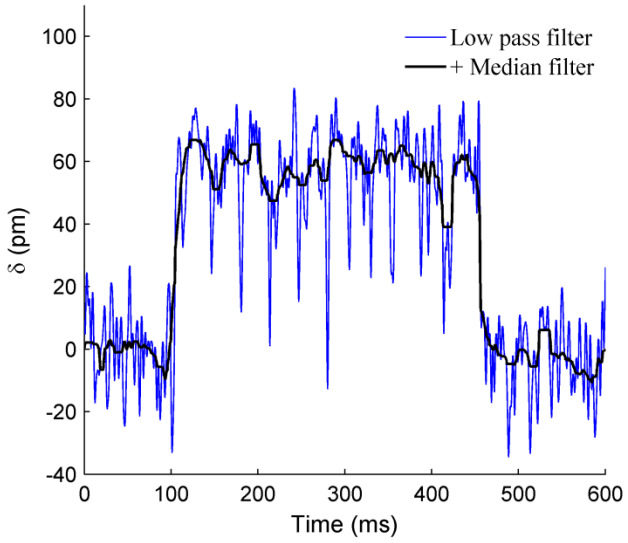

Figure 5.7 Measuring small retardance changes in the VR. The measured retardance change is applied is comparable to that in the pike olfactory nerve.

5.5.2. RETARDANCE IMAGES OF THE NERVE

Light in the sample arm is focused and a small portion of the nerve is interrogated. Understanding the distribution of resting retardance of the nerve is therefore important. Dissected nerves are imaged by scanning the galvanometers in the RSOD mirror and the sample arm. Intensity images are calculated as the summation of the intensities of the polarization channels, and retardance is calculated as the phase difference between the channels. Figure 5.8 shows images of nerve bundles from crayfish claw, and Figure 5.9 shows the largest nerve bundle taken from the first leg of a lobster. The images show that resting retardance is uniform but not in all cases. Images of smaller nerves from the same leg of the lobster and of the ventral nerve in of the crayfish are similar to the crayfish claw nerve in Figure 5.8. Retardance offset in the images is a result of the phase offset shown in Equation 4.14.

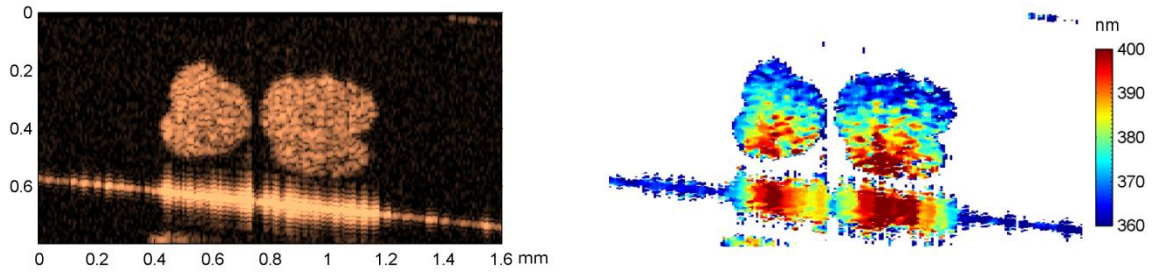

Figure 5.8 Intensity (left) and cumulative retardance (right) images of nerve bundles from the crayfish claw.

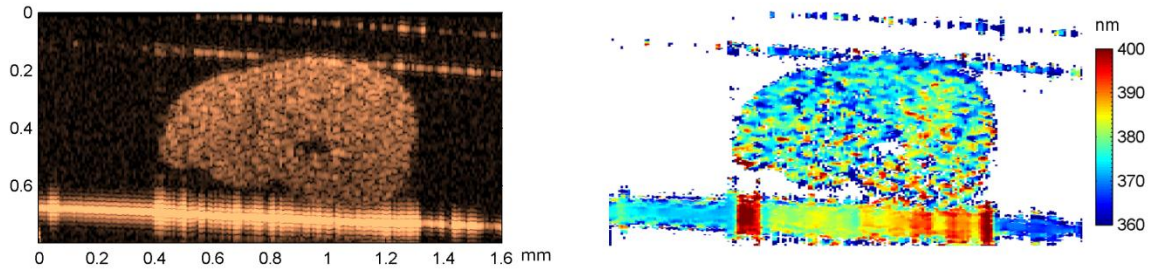

Figure 5.9 Intensity (left) and cumulative retardance (right) images of the largest nerve bundle from the first leg of a lobster. Smaller nerve bundles from the same leg have retardance maps like the crayfish claw nerve in Figure 5.8.

5.5.3. Attempts to Measure Retardance Change due to Neural Activity

In attempts to measure retardance change due to neural activity, interference fringes were acquired from the reflection of the mirror underneath the nerve. Nerves from first leg of lobsters, claw and ventral nerves of crayfishes were used. The nerves were stimulated and retardance was calculated from the phase difference between the channels.

Equation 5.1 shows that, if $\Delta I/I$ is constant, larger retardance change is measured in locations with larger resting retardance. Using XY plots, locations in the nerve where δ is large are located and interrogated. Figure 5.10 shows examples of the XY plots of normalized fringes in different crayfish and lobster nerves. The length of the minor axis of the ellipse corresponds to the retardance between the channels. The minor axis of the ellipse for the mirror is nonzero because of

the phase offset φ_o. One can note the variability between different nerves. The lobster leg nerve has a number of nerve bundles that can be roughly categorized into small and large. The figure shows that higher resting retardance is measured in the large bundles. The extraordinary high retardance measured at the edge of the nerve labeled "large 2" is also seen in Figure 5.9. The origin of the large resting retardance at the edges of the nerve can be better understood by histological sectioning.

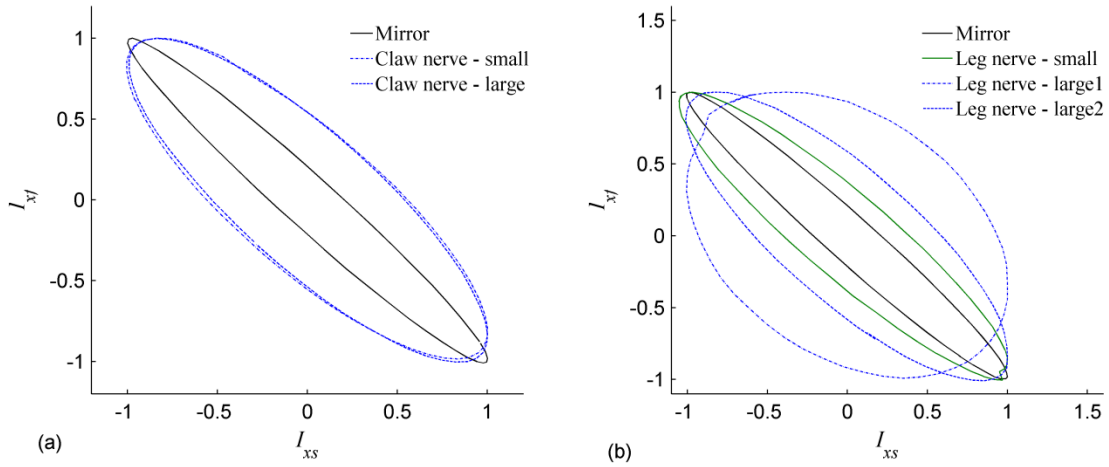

Figure 5.10 XY plots of the normalized interference fringes detected using the PMF-based interferometer. The constant phase offset is observed in the signal reflected from the non-birefringent mirror.

We have run many experiment in attempts to measure $\Delta\delta$. AP was recorded at stimulation currents less than 1 mA, an indication of the healthiness of the axons [76]. Small axons are believed to be the source of retardance change, and stimulation currents on order of a few milliampheres were usually required to stimulate smaller axons [76]. We could not, however, detect retardance changes in any experiment. The signal could not be detected even when noise standard deviation of averages of hundreds of recordings were a few picometers. Fresh nerves were also interrogated when δ is not at the maximum, and no signal was detected.

5.6 Discussion and Future Directions

The demonstrated PSLCI technique has the advantage to directly measure the value of retardance change. The measurement of $\Delta\delta$ using crossed-polarizers setups is altered by the resting retardance δ of the sample. The ratio $\Delta\delta/\delta$ is smaller at larger δ even if $\Delta\delta$ is the same. It was reported that largest $\Delta\delta$ due to action potential is observed at the edges of some nerve models [71]. Figure 5.8 shows larger δ in the center of some nerves, which might be the reason for this observation. A technique that can directly measure $\Delta\delta$ is therefore desired especially when δ is large, as in myelinated nerves.

The retardance change $\Delta\delta$ can be calculated using Equation 5.1 if δ and $\Delta I/I$ are known. We measured the maximum δ in six crayfish claw nerves as 26.3 ± 1.1 nm. Similar resting retardance was measured in the ventral nerve. Large variability was observed in the first leg of lobster samples: the maximum retardance in smaller nerve bundles is around 10 nm, while it is in most large bundles around 30 nm. In a few cases at the edge of large bundles, resting retardance of up to 65 nm was measured.

Using data from [76], $\Delta I/I$ in crayfish claw nerve is about 1×10^{-5}, and up to 6×10^{-5} in the lobster's leg nerve. Using the measured δ, this translates into 0.2 pm to 1 pm $\Delta\delta$, which is around or less than the detection limit of the PMF-based PSLCI system after averaging hundreds of recordings. Because phase sensitivity of the system approaches the theoretical value, nerve models with larger $\Delta\delta$, like the pike olfactory nerve or the crab leg nerve, need to be studied.

It is important to note that light scattering and absorption changes were recorded in activated nerves. The crossed-polarizers setups previously used to measure retardance change are sensitive to light intensity transmitted through the nerve. The measured retardance change may

therefore be an interference or may have different values than reported. Experimental work in [71] has supported the fact that the detected change is in large a birefringence change.

5.7 CONCLUSION

Birefringence of unmyelinated nerves is studied using the PMF-based PSLCI. An adaptive alignment technique is presented to maintain the long term stability of the interferometer. Images of the retardance of crayfish and lobster nerve models were presented. Measurements of the resting retardance of the nerve models have enabled calculating the retardance change during neural activity. The information presented here suggests studying models with larger retardance changes to investigate the possibility of using the system to detect neural activity, and understand the biochemical mechanism of the retardance change.

CHAPTER 6
PMF-BASED FOURIER DOMAIN PSOCT FOR IMAGING[18]

We have demonstrated in CHAPTER 3 the feasibility of using PMF to build TD PSOCT systems. For imaging purposes, however, speed is a main advantage of Fourier-Domain (FD) over TD systems. In this chapter, we present the first FD swept-source PSOCT system using PMF. A single sweep of the optical spectrum yields two complex measurements, sufficient to calculate retardance, optical axis orientation, and polarization-diversity reflectivity information without the need to polarization modulation or compensation. We establish that imaging and signal to noise characteristics of PMF-based PSOCT are comparable to conventional setups; characterization of the PMF system demonstrates sensitivity of 106 dB. Absolute optical axis orientation image is presented, and errors due polarization leakage are calculated. Area and volume images of biological tissues are also demonstrated.

---

[18] The system in this chapter was published and used in the study in the following peer-reviewed journal articles:

- Muhammad K. Al-Qaisi and Taner Akkin, "Swept-source polarization-sensitive optical coherence tomography based on polarization-maintaining fiber," Optics Express 18, 3392-3403 (2010)
- Rouzbeh Amini, Julie E. Whitcomb, Muhammed K. Al-Qaisi, Taner Akkin, Syril Dorairaj, Tiago Prata, E. Illitchev, Jeery Liebmann, Robert Ritch, and Victor H. Barocas, "The Posterior Location of the Dilator Muscle Induces Anterior Iris Bowing during Dilation Even in the Absence of Pupillary Block," (In review) Investigative Ophthalmology and Visual Science

6.1 INTRODUCTION

FD OCT does not require scanning of the reference arm. Instead, the spectral coherence function, which is a Fourier pair with the A-line, is recorded (see Appendix D). FD OCT is realized by utilizing a spectrometer in the detection arm, this approach is known as spectral-domain (SD) OCT [5-7]; or by sweeping through the spectrum of the laser source, known as swept-source (SS) OCT [8-10]. FD systems advance faster imaging speeds, and improved theoretical sensitivity [11-13]. In [77], some theoretical and practical concerns about the advantages of FD systems were raised.

Several FD PSOCT systems have been already introduced in bulk and based on SMF [78-84], retaining the same limitations in the corresponding SMF TD implementations. SD PSOCT systems equipped with two line scan cameras have been demonstrated in free-space [79], and with a SMF implementation that requires at least three incident polarization states [80]. Single camera-based SD PSOCT systems have also been reported in free-space [81], and with SMF implementation that requires two consecutive A-scans [82]. SMF-based SS PSOCT system has been demonstrated with dual-detectors requiring two consecutive scans to quantify birefringence [83]. Sophisticated SMF-based SS PSOCT setups in [84, 85] have enabled single-scan imaging using dual-detectors [84], and a single-detector with the incident polarization state circumnavigates Poincaré sphere during a single A-scan [85]. Optical axis orientation measurement has also been demonstrated [79-81, 85].

PMF-based SD PSOCT setups were recently developed at 850 nm range using single [86] and dual [87] camera setups. SS systems compared to SD ones have the advantage to introduce less motion artifacts [88]. Lasers available for SSOCT operate at higher wavelength yielding deeper penetration in further scattering tissues. Moreover, the simplicity of the detection arm in SSOCT makes it possible to perform differential measurements to potentially eliminate the excess

source noise [89, 90], remove the fixed parasitic lines due to laser source and autocorrelation in the interferometer [91], and achieve power efficient interferometers [92].

Herein, we introduce a SS PSOCT based on PMF that benefits from the advantages of balanced detection. The system operates at 1300 nm regime, suitable for imaging turbid tissues. In a single axial scan and a straightforward algorithm, the PMF-based PS interferometer retrieves retardance, relative optical axis orientation, and polarization-independent reflectivity information of a turbid sample. The circular polarization state illuminating the sample yields birefringence measurements insensitive to sample orientation in the lateral plane. Here, we describe the system and compare its dynamic range and sensitivity with those of SMF-based SSOCT. The influence of temperature changes is investigated. Retardance and axis orientation measurements of the SS PSOCT are also characterized. The results demonstrate sensitive, accurate, and ghost-line-free performance. Area and volume imaging capabilities of the SS PSOCT are demonstrated by imaging tissues *ex vivo*. A fast tuning frequency of 28 kHz is achieved by an in-house built polygon mirror monochromator, with imaging rate limited by the data acquisition system.

6.2 HARDWARE SETUP

The schematic of the PMF-based SS PSOCT with a polygon mirror based tuned source is shown in Figure 6.1. Half of the output power of the internally isolated booster optical amplifier (BOA) (Covega Corporation, MD) is tapped out of the cavity using a 50:50 coupler. The other half is transmitted to a polygon scanning monochromator through a circulator. The monochromator is built of a 600 lines/mm grating, a confocal telescope (75 and 35 mm achromatic lenses), a rotating polygon mirror (6.1 cm diameter, 72 facets) (Lincoln Laser, AZ), and an end mirror. After a round trip in the filter, light is directed by the circulator to feed back into the optical amplifier. Five percent of the light exiting the cavity is directed to a grating-based trigger generator that tracks a narrowband line of the source output to synchronize data acquisition. The other 95% illuminates

the interferometer with an average power of 45 mW. The speed of the SS is determined by the number of facets of the polygon and its rotation speed. Details about the function of the SS can be found in [96].

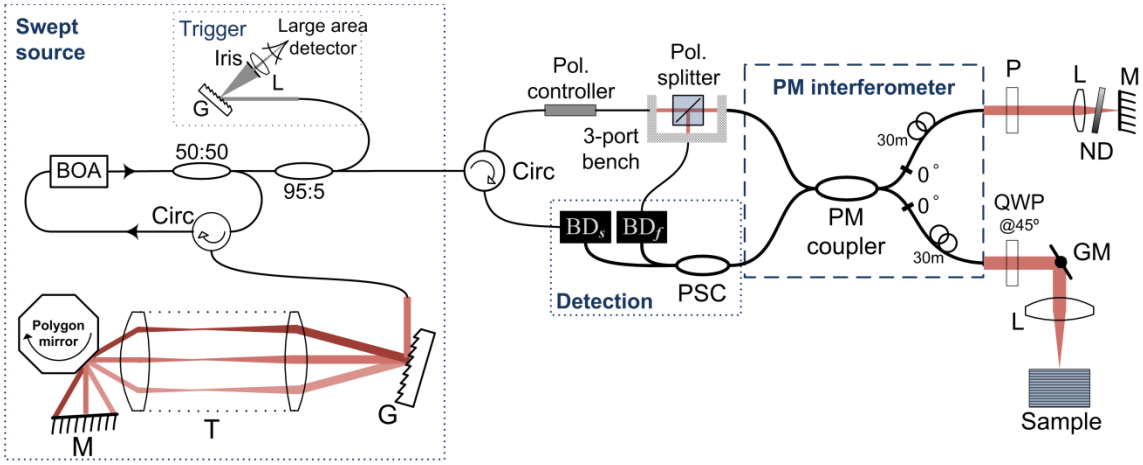

Figure 6.1[19] PMF-based SS PSOCT system. BD: balanced detectors, BOA: booster optical amplifier, Circ: circulator, G: grating, L: lens, T: achromatic telescope, M: mirror. P: polarizer, ND: neutral density filter, QWP: quarter-wave plate, and GM – galvanometer scanner. Dashed boxes show various stages as labeled. Bold lines represent the PMF. Zero degree splices in the reference and sample arms are indicated.

The output of the swept source is fed into a circulator that prevents returning light from reentering the laser cavity. A polarization controller is employed to maximize the polarization state transmitted through a polarization splitter cube, which is positioned in a three-port fiberbench (Thorlabs, NJ). The output port is aligned so that all the polarized light is coupled into the slow axis of the PMF.

[19] Some data presented in this chapter were collected with a free-space optics detection arm. The polarization states were split using a Wollaston prism, and the beams were focused on the detectors using a lens. The sensitivities of the SS PSOCT using the two detection configurations were compared and found similar.

A PM coupler transmits equal shares of light into the sample and reference arms. In the sample arm, an achromatic QWP aligned at 45º with the slow axis of the PMF transmits circularly-polarized light, focused using a lens onto the sample. Lateral scanning of the sample is accomplished by galvanometer scanners. In birefringent tissues, the polarization state of light is altered as it propagates in the sample. Light backscattered from the sample is collected by the lens and coupled back into the fast and slow channels of the PMF. The sample light carries information about the reflectivity and birefringence of the sample.

The free space of the reference arm consists of a polarizer rotated at 45º with respect to the slow axis of the PMF, a 45 mm achromatic lens, a neutral density attenuator, and a mirror. After a round trip in this setup, light is equally coupled in the slow and fast axes of the PMF. As a result, two equal polarization components reenter the PM coupler from the reference arm's end. The polarization components in the reference arm interfere with the corresponding ones in the sample arm, making it possible to describe any polarization state of light backscattered from the sample.

6.2.1. Aligning the Coherence Functions

Birefringence of the PMF renders a lag between the polarization components propagating in the slow and fast channels. If this lag is matched in the two arms, the coherence functions of the polarization channels will coincide. Otherwise, an axial shift between the envelopes of the coherence functions, U_s and U_f, is observed. If not taken into account, this can degrade the resolution and generate errors. U_s and U_f are aligned by using fiber segments from the same production pool with matched lengths in the sample and reference arms. A length mismatch of one

beat length (2.5 – 4 mm[20] for Corning's PM1300) leads to a λ_0 shift between U_s and U_f; an order of magnitude smaller than the axial resolution (See Section 6.4.1).

6.2.2. BALANCED-DETECTION

When the coherence functions U_s and U_f are aligned, and the optical pathlength difference between the two arms is smaller than the instantaneous coherence length of the source, spectral interference fringes form on two orthogonal channels. The PM coupler directs half of the power of the interference patterns into the detection arm, and the other half goes into the input arm. The interference signals on the input and detection arms are 180º out of phase [89]; therefore, subtracting one signal from the other, known as balanced-detection, doubles the signal and minimizes the common excess noise.

In the detection arm, a PMF-based PSC splits the interference patterns carried on the orthogonal channels of the PMF, and couples them to the corresponding positive elements of the balanced-photodetectors (PDB150C, Thorlabs, NJ). Balanced detection is achieved for both channels by collecting the interference patterns returning to the input arm, and coupling the light to the corresponding negative elements of the balanced photodetectors - the pattern on the slow channel is collected through the polarization splitter, polarization controller, then the circulator; whereas light from the fast is collected from the polarization splitter using a fiber.

6.2.3. SIGNAL AMPLIFICATION AND ACQUISITION

Higher frequencies of the spectral interference pattern correspond to deeper sample penetration, see Appendix D. The PDB150C balanced detectors do not provide enough bandwidth at electrical gain higher than 10^4. We built two extra amplifier circuits to further amplify the

[20] From Corning's datasheet

outputs of the detectors and cover the entire dynamic range of the analog to digital converter. The amplifiers are based on the high speed OPA657 operational amplifiers (Texas Instruments, TX) and have a gain of -95[21]. A schematic drawing and a picture of the circuit are shown in Figure 6.2.

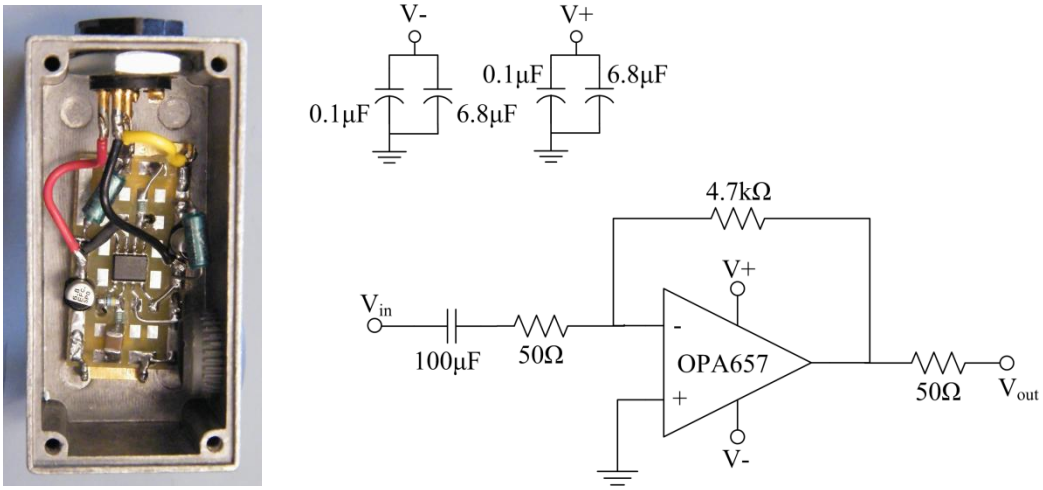

Figure 6.2 A picture and the schematic diagram of one of the amplifiers used for second stage amplification.

To avoid degradation of the amplified electrical signals at higher frequencies, the shortest possible segments of high frequency coaxial cables were used to conduct the signals to a 12-bit analog to digital converter (PCI-6224, National Instruments). The signals are digitized at 50 MS/sec.

[21] A prototyping board (9081, Capital advanced technologies, inc., IL) was found convenient for permanent fabrication. Input resistor = 50 Ω, and feedback resistor = 47 kΩ. Stray capacitance of the wires was minimized by routing the feedback resistor through the back of the board after drilling fine holes to pass the wires. Two sets of parallel capacitors, 6.8 µF electrolyte and 0.1 µF tantalum, were added to the positive and negative supplies of the OPA657 to filter line noise was filtered. External noise was reduced by enclosing the circuit in a grounded aluminum enclosure. The DC input was blocked by a 100 µF ceramic series capacitor. The amplified signal was coupled to the output through a 50 Ω series resistor.

6.3 SIGNAL PROCESSING

SS OCT captures the spectral interference information, and the complex interference information along the sample depth need to be calculated, see Appendix D. In the PMF-based SS PSOCT two channels are simultaneously acquired and similar signal processing is applied to each. The number of points in each spectral pattern is first doubled to 3400 points/line using a Fourier-transform-based interpolation method [93]; more points allows more accurate numerical processing in the following steps. The spectral interference patterns are remapped from wavelength domain (λ) to wavenumber domain ($k = 2\pi/\lambda$) [7, 93]; depth information are in fact a Fourier pair with wavenumber-indexed spectra. Apodization [94] is then applied to suppress the side lobes due to truncation; hamming window is used here. Dispersion mismatch is compensated using a numerical method [95]. Fixed lines due to interferences in the source and the coupler are removed by subtracting the reference arm's signal; that is the signal recorded when the sample arm is blocked [11, 91]. The complex information along the A-line, U_s and φ_s, and U_f and φ_f, are calculated using Fast Fourier transform. Since the interference data is real, information in the spatial domain are symmetric, a Heaviside function is therefore applied. Equations 3.17, 3.18, and 3.22 are used to calculate polarization-diversity reflectivity, retardance, and optical axis orientation, respectively. The chart in Figure 6.3 shows the steps to calculate PSOCT images from the acquired signals.

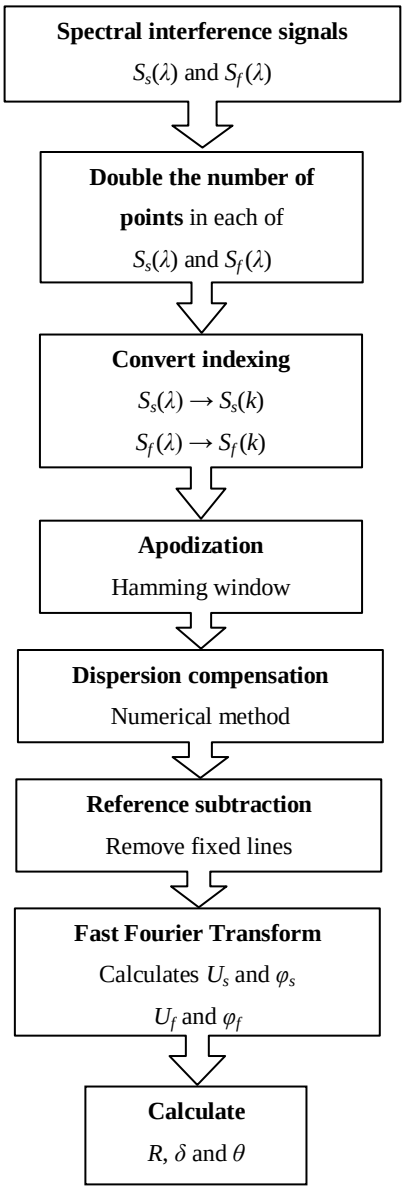

Figure 6.3 Signal processing applied to calculate PSOCT images from the acquired signals.

6.4 SYSTEM CHARACTERIZATION

6.4.1. OPTICAL SPECTRUM

The time-varying output of the swept source is recorded by a photodetector; Figure 6.4 (a) shows four consecutive cycles of the record. A single cycle is used to calculate the optical spectrum of the SS shown in Figure 6.4 (b); the spectrum is calculated using the monochromator

characteristics calculated from the grating equation and the responsivity curve of the detector. Using the calculated spectrum, the center wavelength of the source, λ_o, is measured at the maximum power as 1291 nm, and the FWHM bandwidth, $\Delta\lambda$, is measured as 78 nm. Theoretical axial resolution is calculated using Equation 2.4 as 9.4 µm. The polygon-based swept source for SSOCT was presented in [96].

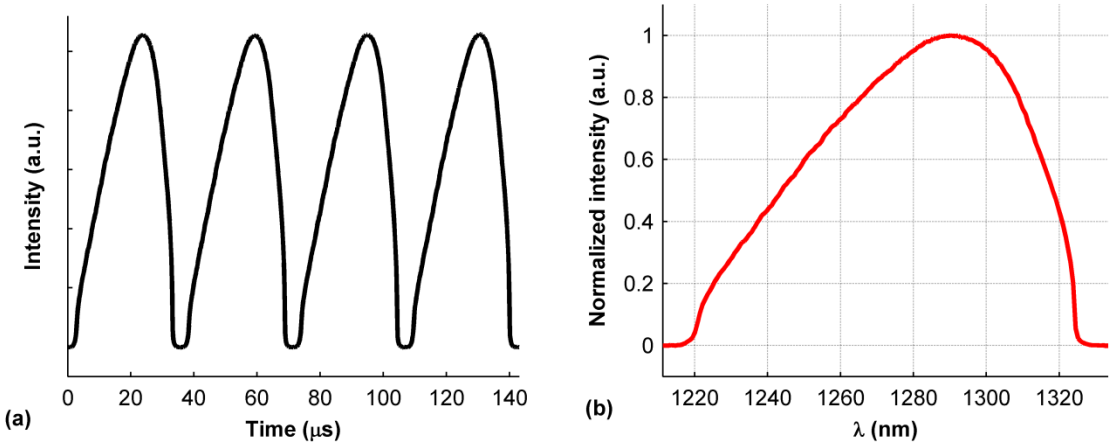

Figure 6.4 (a) Output of the swept source, (b) optical spectrum calculated from the characteristics of the monochromator.

6.4.2. ALIGNMENT OF THE COHERENCE FUNCTIONS

The alignment of the coherence functions on the polarization channels is demonstrated by using a mirror and a neutral density filter in the sample arm, and rotation the QWP to 22.5° in order to couple the sample light in the two channels. The coherence function amplitudes U_s and U_f acquired at sample depth of 500 µm are shown in Figure 6.5. The figure shows that the separation between the two coherence functions is sufficiently smaller than the axial resolution; the alignment is therefore adequate for imaging.

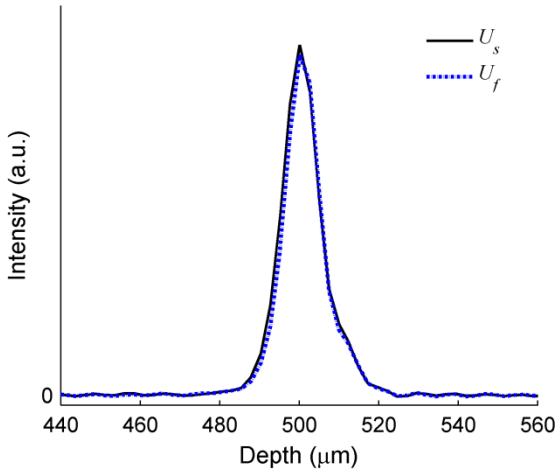

Figure 6.5 The coherence functions on the slow and the fast channels.

6.4.3. SIGNAL TO NOISE MEASURES

In order to study the signal to noise characteristics of the PMF-based SS PSOCT, the QWP is returned to 45° with respect to the slow axis of the fiber. A mirror and a neutral density filter with and optical density (OD) of 2.1 were placed in the sample arm. Figure 6.6 shows the reflectivity profile at sample depth of 500 μm. Logarithmic scaling is calculated as in Equation 3.19. The raw reflectivity profile is calculated after mapping the spectrum into the *k* domain, and compensating for dispersion in software, see the black trace in Figure 6.6. The red trace shows the suppression of the broad side lobes by apodization. The figure also shows that the autocorrelation term at $d \approx 0$, and the source line at 0.1 mm diminish after reference subtraction. The maximum reflectivity at 500 μm is equal to the double-pass attenuation in the sample arm ($2\times10\times OD_{sample}$).

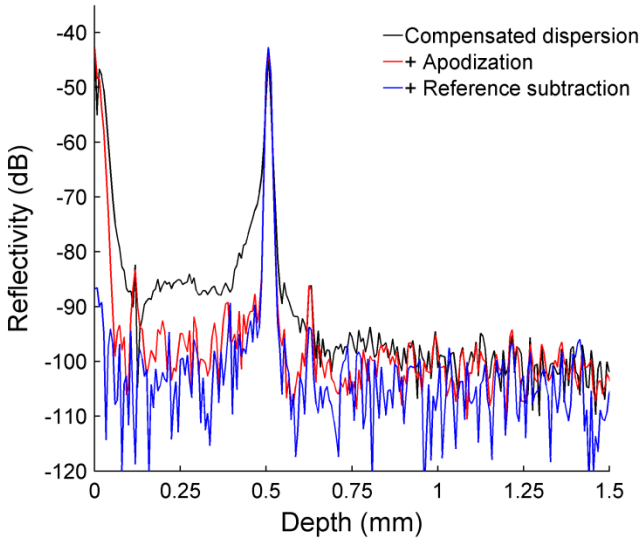

Figure 6.6 Coherence function of PMF-based SS PSOCT. Black trace shows the coherence function after dispersion compensation. The red and blue traces are obtained after apodization, and reference subtraction in addition to apodization, respectively.

To quantify the dynamic range and sensitivity of the reflectivity measurement, light from the sample arm was attenuated to a level close to tissues. The power returning from the reference and sample arms was measured at the fast channel of the detection arm as 12 µW and 220 nW, respectively. Because the sample is not birefringent, there is no light coupled back in the slow channel of the sample PMF. To avoid saturating the photodetectors, the source power was attenuated by slightly loosening the FC/APC connector between the SS and the circulator. The dynamic range, SNR_{dB}, is measured as the difference between peak reflectivity and the baseline

$$SNR_{dB} = (\text{peak reflectivity} - \text{baseline})_{dB} \quad \textbf{6.1}$$

After apodization and reference subtraction, the baseline values between 1 and 1.5 mm are averaged and the dynamic range is measured as 64.2 dB.

Sensitivity is defined as the largest sample reflectivity that can be measured. The value of the interferometer's sensitivity is equal to the value of the baseline of the reflectivity profile. It can be calculated as the summation of the dynamic range and the double-pass sample arm attenuation

$$\text{Sensitivity}_{\text{dB}} = \text{SNR}_{\text{dB}} + 2 \times 10 \times \text{OD}_{\text{sample}} \quad \textbf{6.2}$$

Sensitivity of the PMF-based SS PSOCT is measured as 106.2 dB, which is in the range of optimized SMF-based SSOCT systems [91, 94, 97]. A noise model developed in [91] for shot noise limited SMF SSOCT systems approximates the theoretical sensitivity to

$$\text{Sensitivity} = -10 \log_{10}\left(\frac{\eta \lambda_o P_{sample}}{hcf_{ss}}\right) \quad \textbf{6.3}$$

where η is the detector sensitivity, P_{sample} is the power illuminating the sample, h is Planck constant, and f_{ss} is A-line rate. With $\eta \approx 1$, $h \approx 6.626 \times 10^{-34}$ $\text{m}^2\text{kg/s}$, $P_{\text{sample}} = 4.5$ mW, and $f_{\text{ss}} = 28$ kHz, the theoretical sensitivity is equal to 120 dB. The interferometer was optimized by reference arm attenuation (see Section 2.3.3) and balanced-detection; the latter has resulted in 6-7 dB improvement on the SNR of the system. Sensitivity deviation from the theoretical value is discussed in the next subsection.

Without apodization, axial resolution is measured as 12.2 μm in air. This deviation from the theoretical value is attributed to errors in mapping the optical spectrum, its non-Gaussian spectral distribution, and limited accuracy in numerical processing. Although apodization reduces resolution to 15 μm, the contrast advantage is worthy.

6.4.4. SENSITIVITY OF PMF- VERSUS SMF-BASED INTERFEROMETERS

It is important to compare the performance of PMF-based systems to the conventional SMF approach. The PM coupler was replaced with a SMF-based 50:50 coupler. The input arm of the coupler was directly connected to the circulator output, and the fiber of the detection arm was directly connected to the balanced detector. The polarizer and the QWP were removed from the reference and sample arms. Light power in the sample arm, and attenuation of light in the sample and reference arms were all matched to the corresponding values in the PMF interferometer. Degraded sensitivity was observed when polarization states in the sample and reference arms were not matched (see Section 2.7); therefore, polarization controllers were added to the fibers of the two arms to maximize the fringe visibility.

Figure 6.7 shows the reflectivity profiles of the SMF and PMF interferometers. The measured sensitivity in the SMF system is 112 dB. The discrepancy between the measured and the 120 dB theoretical sensitivity is attributed to residual thermal and excess noise. The additional 5.8 dB sensitivity loss in the PMF system is attributed to leakage between the polarization channels of the optical components. The reflectivity SNR and sensitivity of the PMF-based PSOCT are however comparable to those in SMF-based systems.

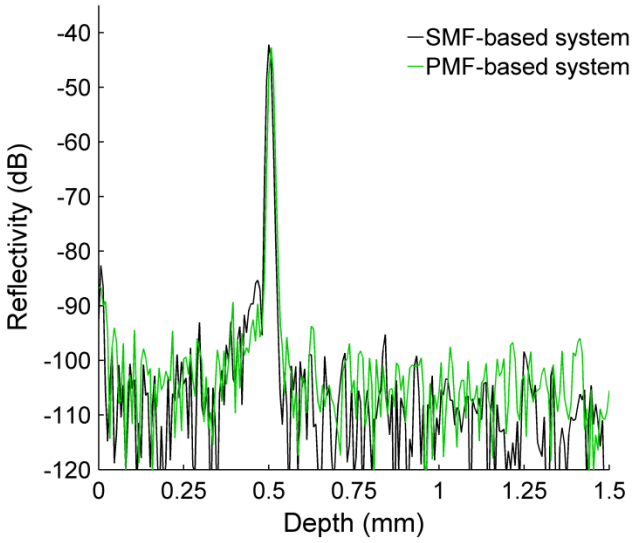

Figure 6.7 The reflectivity profile of the PMF-based interferometer compared to equivalent SMF-based system.

6.4.5. IMAGING CHARACTERISTICS OF PMF- VERSUS SMF-BASED OCT

The finite instantaneous line width of the swept source results in decay in the SNR, and therefore the sensitivity, at larger depths; see Appendix D. The depth-dependent degeneracy is characterized for both PMF and SMF fiber systems. The coherence functions of the two SS OCT systems at different sample depths are shown in Figure 6.8. The characteristics of the PMF system shown in Figure 6.8 (a) are similar to that of the SMF fiber system in Figure 6.8 (b). The figure shows that the decay is the same using the two interferometers; a decrease of about 11 dB was measured at a depth of 2.75 mm for both cases.

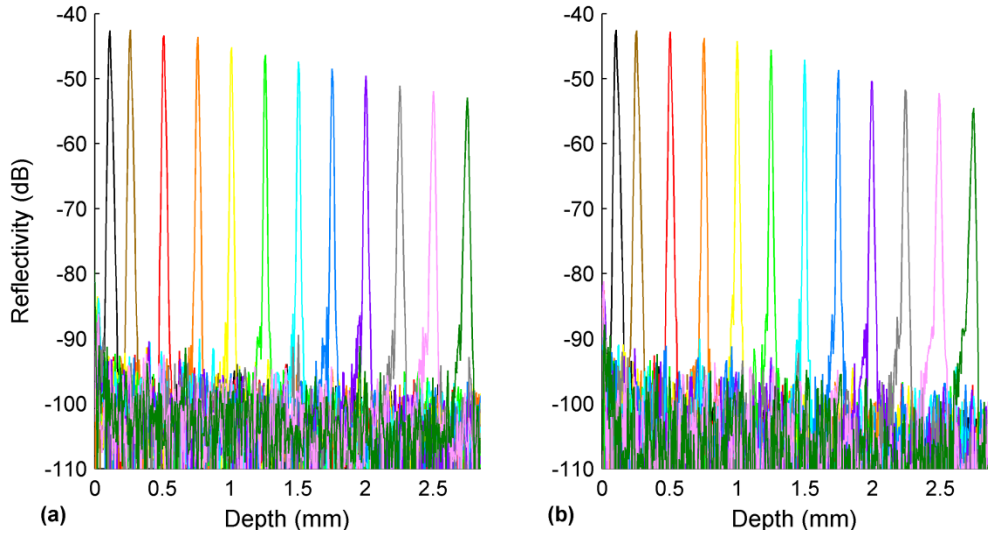

Figure 6.8 Depth degeneracy in (a) PMF-based SS PSOCT, and (b) equivalent SMF-based SS OCT. Differences between the plots are barely distinguishable.

Because reflections from larger depths in the sample correspond to higher frequency components in the spectral fringe pattern, they are described by fewer number of points after digitization; giving rise to larger numerical errors. The axial resolution measured at 2.75 mm is consequently degraded to 18 µm in air. Such degradation is common to SSOCT systems [94, 98].

6.4.6. IMAGING RANGE

Fourier transform is calculated in the digital domain; hence, imaging depth range is limited because of aliasing. The range of the recorded wavelength spectrum in each source sweep is 125 nm (see Figure 6.4 (b)). It is sampled at 1700 points per A-line; yielding an instantaneous bandwidth of $\delta\lambda \approx 73.5$ pm. Using the equation for imaging range in [6] (see Appendix D)

$$d_{max} = \frac{1}{4n}\frac{\lambda_o^2}{\delta\lambda} \qquad \textbf{6.4}$$

the imaging range of system is calculated as 5.7 mm in air; plenty for OCT imaging. The calculated d_{max} number was experimentally confirmed.

6.4.7. BIREFRINGENCE MEASUREMENTS

To characterize the birefringence measurements of the PMF-based SS PSOCT system, a voltage-controlled liquid crystal Variable Retarder (VR) was used as a birefringent sample. The VR is placed in the sample arm between the quarter wave plate and the lens. A mirror is used as reflector, and a neutral density filter is also placed in the sample arm to attenuate the light to the same level used in Section 6.4.2. The voltage applied to the retarder was scanned from 0 to 10 V with a step size of 10 mV. Figure 6.9 shows the retardance curve obtained from the system. The shape of the curve is consistent with the one shown in Figure 3.7 (b). The measured retardance, however, is slightly different due to the large discrepancy between the measurement wavelengths.

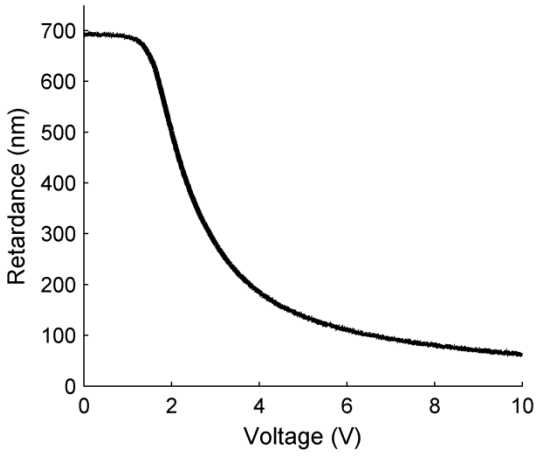

Figure 6.9 Retardance measurement of a voltage-controlled variable retarder.

Because light incident on the sample is circularly polarized, the retardance measurement is insensitive to the optical axis orientation of the sample. This is illustrated by fixing the retardance of the variable retarder and rotating it over a range of 180° in rotational steps of 5°. Figure 6.10 shows the measured phase retardance, δ, in hollow blue circles. Indicating a repeatable measurement, the average of δ is 43.2° with 0.8° standard deviation. Figure 6.10 also shows the

optical axis orientation, θ, in solid green circles. The measurement deviates from a unity slope by 0.02, and has a standard deviation of 2.5º around the best fit line.

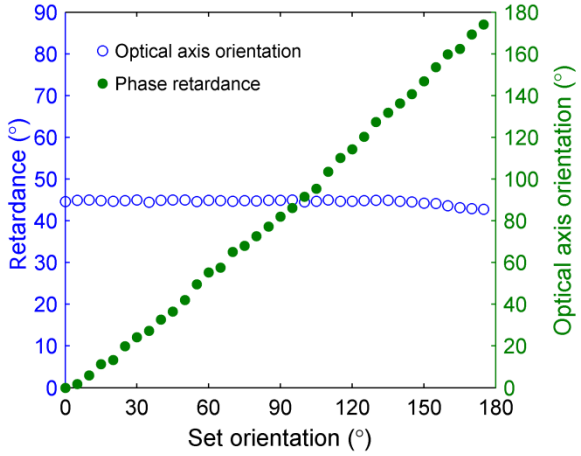

Figure 6.10 Measurements of retardance and axis orientation as a function of rotation.

To look into the stability of the birefringence measurement at different sample depths, both retardance and orientation of the variable retarder were fixed and the optical path length difference between the reference and sample arms was varied by extending the reference arm. Figure 6.11 shows the consistency of the measurement over a depth of 2.75 mm. Standard deviations of 0.7º and 2.0º were calculated for phase retardance and axis orientation measurements, respectively.

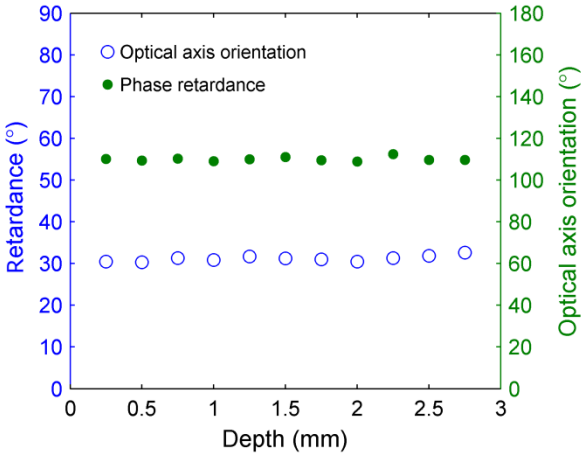

Figure 6.11 Measurements of retardance and axis orientation as a function of sample depth.

Errors in Figure 6.10 and Figure 6.11 are attributed to misalignments and imperfections of the polarization components. The phase offset $\varphi_o/2$ in Equation 3.22 is measured and subtracted from the phase measurements in the figures; therefore, the measurements shown in the figures are absolute not relative axis orientation. This demonstrates the feasibility to measure the phase bias and subtract it to achieve absolute axis orientation images.

6.4.8. TEMPERATURE EFFECT

Birefringence of the sample and reference fibers, and consequently the phase offset φ_o, changes with external perturbations. To study the influence of temperature changes on the birefringence measurements, retardance and axis orientation of the VR were fixed, and the temperature of a 60 cm long segment of the sample fiber was increased from 25 ºC to 42 ºC. The solid lines in Figure 6.12 show that the retardance measurement was not altered by the temperature change, but the axis orientation measurement was drifting. Almost a full wavelength shift was observed by the 17 ºC temperature increase.

The dotted lines in Figure 6.11 represent data acquired when fiber segments with the same lengths from the sample and reference arms were heated together. The data shows that the birefringence changes in the two arms cancel out and the axis orientation measurement is constant. This suggests that altering the axis orientation measurement due to disturbing the sample fiber can be compensated in the reference fiber. PMF heating experiments were executed on different days and the environment dependence of the VR is probably the reason for the difference between retardance measurements in the two experiments. Temperature data was recorded manually, and the slight errors observed at higher temperatures are attributed to human errors.

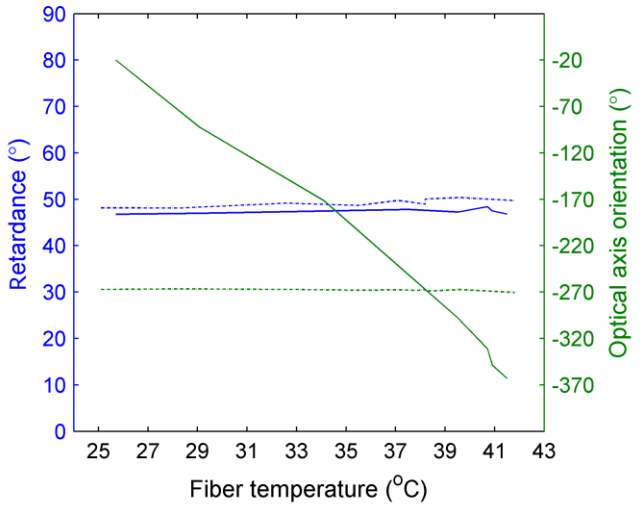

Figure 6.12 The effect of changing the temperature of a segment of the fiber of the sample arm (solid lines), and two equal segments of the fibers of the sample and reference arms (dotted lines). The retardance measurement is constant in both cases. The axis orientation measurement is influenced by the temperature of the sample fiber. This effect cancels out when the fibers experience the same temperature change.

6.5 TISSUE IMAGING

6.5.1. AREA IMAGING

The capability of PMF-based SS PSOCT to image biological tissues is demonstrated by imaging chicken muscle and tendon tissues. The sample objective is a telecentric lens (LSM03, Thorlabs, NJ) that guarantees a flat imaging plane despite scanning, and a minimal change on the lateral spot size across the scanned field. Illuminated by a collimated beam with 2.4 mm diameter, the lens provides a lateral resolution of 42 μm.

Figure 6.13 shows the reflectivity and retardance images of muscle and tendon tissues from a chicken leg. Each image consists of a 1000 A-line. The dynamic range of the reflectivity images is 40 dB. The retardance images show banding patterns with a frequency proportional to tissue birefringence. The tendon was covered with a non-birefringent connective tissue that is hardly distinguishable in the reflectivity image. The two tissues are however easily differentiated in the retardance image. The frequency of the banding patterns shows that the tendon tissue exhibits more birefringence than the muscle tissue. Phase retardance at the tissue surface is zero, which changes as light propagates deeper in the birefringent tissue. The measurement returns back to zero after 180º of single pass phase retardance. Based on this, approximate phase retardance values of 320 º/mm and 1280 º/mm are measured for the leg muscle and tendon tissues shown in Figure 6.13, respectively.

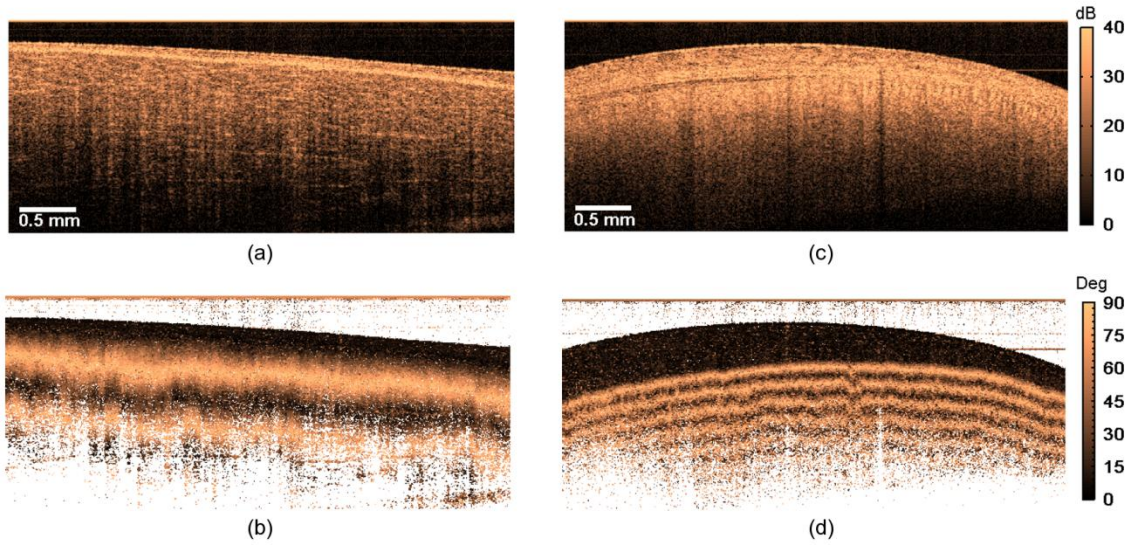

Figure 6.13 Reflectivity (a,c) and phase retardance (b,d) images of a chicken leg muscle (a,b) and tendon tissue (c,d).

To demonstrate imaging of the relative axis orientation, a rectangular slab of a muscle tissue harvested from chicken breast was diagonally cut into two pieces. The pieces were put together so that the muscle fibers had an angular separation. Figure 6.14 shows the acquired images. The reflectivity and retardance images are not influenced by the orientation of tissue fibers. The relative optical axis orientation image, however, displays this variation as an additional contrast. The measured phase retardance for the imaged breast muscle tissue is 450 °/mm.

6.5.2. Absolute Optical Axis Orientation Image

The alignment of the coherence functions envelopes was discussed in Section 6.2.1, and demonstrated in Section 6.4.2. The phases of the coherence functions, however, are not matched using the same method, and the phase offset φ_o yields relative axis orientation mapping. The offset is measured using a retarder with known orientation, and absolute orientation images can be obtained by subtracting the offset. The relative axis orientation image in Figure 6.14 (c) was corrected, and the image of the absolute axis orientation is shown in Figure 6.15.

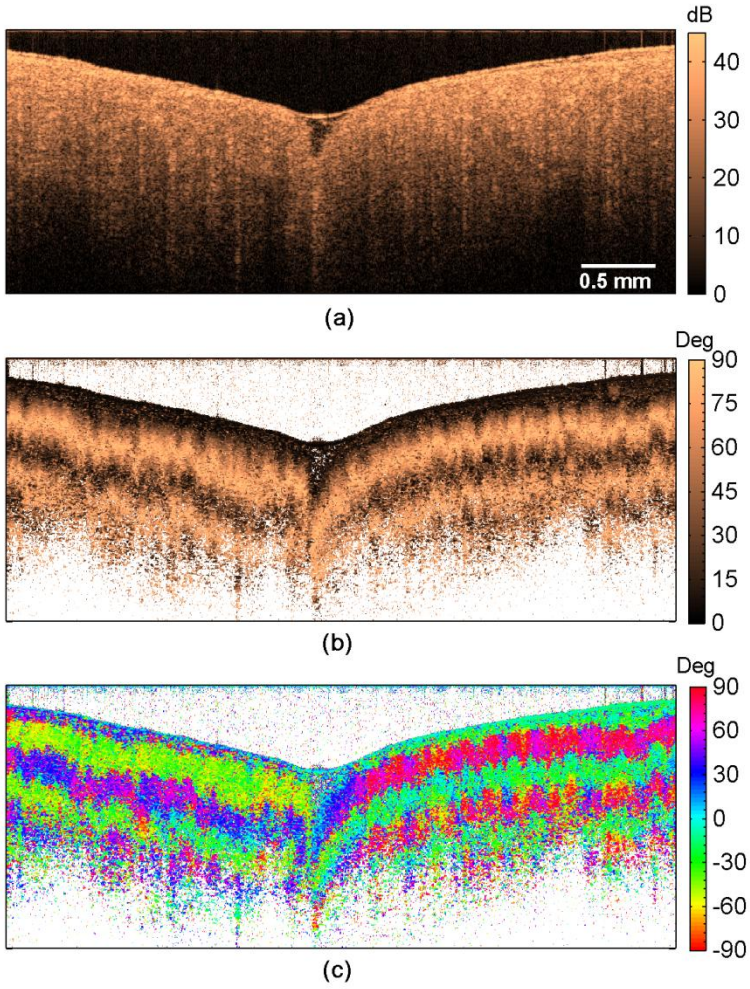

Figure 6.14 Reflectivity (a), phase retardance (b), and relative optical axis orientation (c) images of two angled slabs of chicken breast muscle.

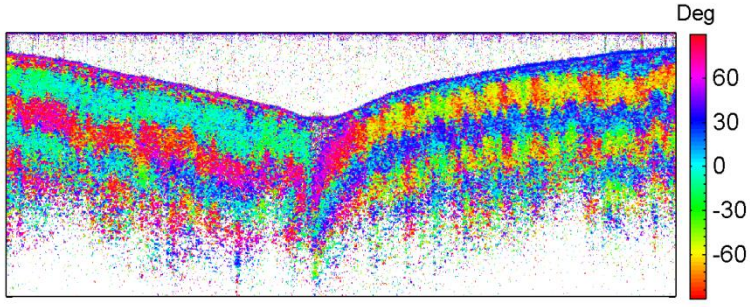

Figure 6.15 Absolute optical axis orientation image of the same data in Figure 6.14 (c) after subtracting the phase offset.

6.5.3. VOLUME IMAGING

The galvanometer scanner in the sample arm was scanned in the two lateral directions, and a volume image of pathologic human bladder tissue was imaged *ex-vivo*. A 1000 frame were recorded along the *x* direction, and 260 frames on the *y* direction. Views of the three-dimensional reconstruction of the tissue are shown in Figure 6.16.

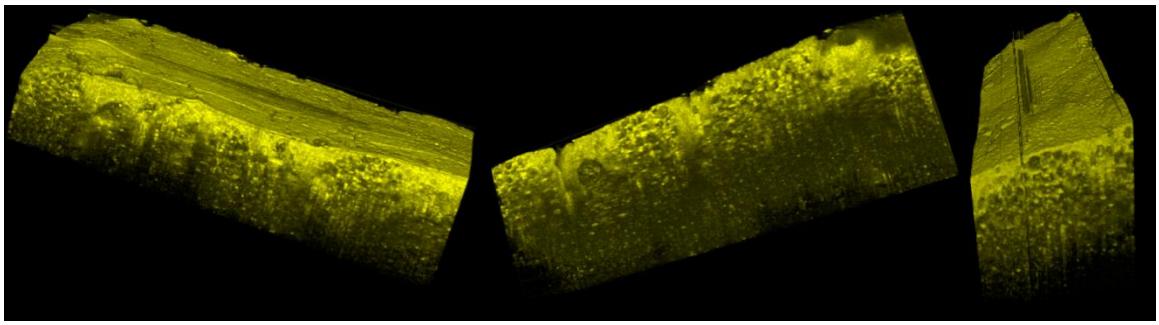

Figure 6.16 Views of the 3D reconstruction of pathologic human bladder tissue.

6.6 DISCUSSION

6.6.1. POLARIZATION LEAKAGE

PMF exhibit high isolation between its orthogonal channels. In some instances, however, polarization leakage can occur, and leaked components interfere with other components generating undesired lines. The main unavoidable polarization leakage occurs in the PM coupler. To understand how ghost lines arise, light components reentering the PM coupler from the sample and reference arms are shown in Figure 6.17 (a and b). The original polarization components of the sample and reference lights are shown in solid black lines, and the leaked components are shown in dotted red. The components that reenter the PM coupler on the fast and slow channels of the fibers are marked with triangles and diamonds, respectively. The leaked components originate when the PM coupler splits the light between the sample and reference arms. The shifts between

the polarization components are due the birefringence of the PMF in the two arms. It is assumed that the sample light is coupled in the two channels of the PMF.

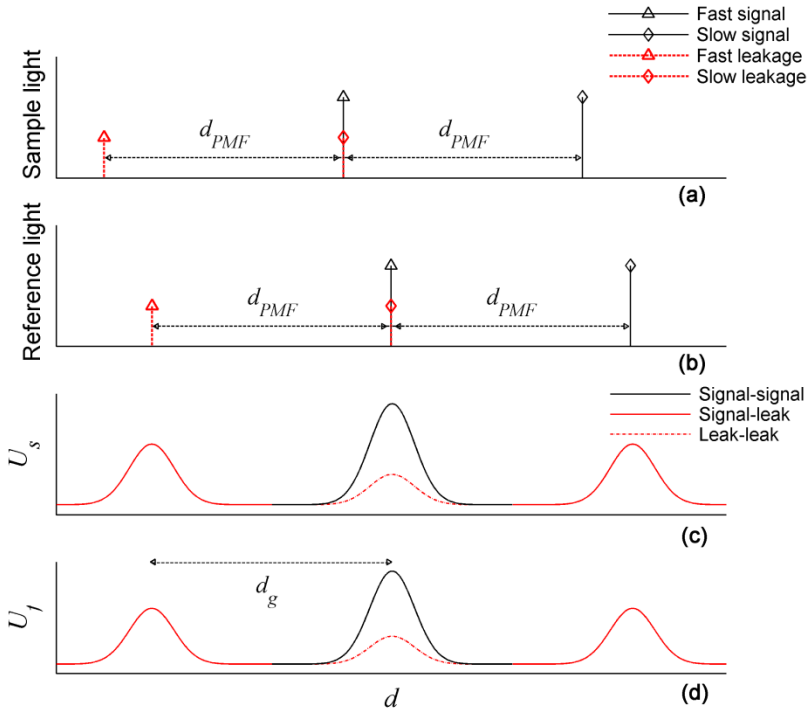

Figure 6.17 The polarization components for light coupled from the sample (a) and reference arms (b) in the PM coupler. The delay d_{PMF} is due to the birefringence of the PMF in the sample and reference arms. (c, d) show the coherence functions envelopes are shown in black, the ghost lines are all in red, and the line due to leaked component interferes with leaked component are shown in dotted red. All amplitudes describe the relative intensities, but they are not plotted to scale.

The plots (c) and (d) in Figure 6.17 are showing the coherence functions due to interference of components in (a) and (b). The main lines are shown in black, the ghost lines due to a signal interfering with leakage are shown in solid red, and the smaller lines due leaked components interfering with each others are shown in dotted red. The signal-leak ghosts are separated from the main lines by a delay, d_{PMF}, equal to the phase lag in the fibers of the sample or reference arm. The leak-leak lines coincide with the main lines. Errors in due to the leak-leak lines are discussed in the following section.

Since the separation between the main line and the large signal-leak ghost lines, d_{PMF}, is dictated by the length of the PMF in the sample and reference arms, the signal-leak ghosts can be displaced out of the imaging range by adding long PMF segments to the two arms. The displacement is equal to a single pass lag between the orthogonal channels of the PMF. Depth ranging of the sample, *d*, is actually measured as a double pass delay that is converted to a single pass by dividing by two. Thus, the displacement, d_g, between the ghost line and the main is equal to half of the delay in the PMF segment

$$d_g = \frac{1}{2}\frac{l_{PMF}\lambda_o}{L_B} \qquad \textbf{6.5}$$

where L_B is the beat length, and l_{PMF} is the PMF length in the sample arm (equal to that in the reference arm).

The signal-leak ghost lines are displaced by adding 30 meters long PMF segments to each of the sample and reference arms. With L_B = 2.5 to 4 mm for Corning's PM 1300 fiber, the calculated displacement is between 4.9 and 7.8 mm; we measured a displacement of about 6 mm. Because the fiber segments are substantially long, slight difference in the optical properties of the PMF segments can result in severe dispersion mismatch, and difficult alignment of the coherence functions. Therefore, using PMF segments from the same manufacturing pool is highly desirable.

Leakage in either of the detection or input arms of the interferometer gives rise to fixed parasitic lines. These lines are minimized by fine alignments of the FC/APC connection between the PM coupler and the PSC in the detection arm, and the polarization splitter cube with respect to the PMF axes in the sample arm. Precise alignment was accomplished by displaying the A-line in real time, and aligning until the parasitic lines diminish. Residuals, if any, are eliminated by

reference arm subtraction. The method we used to precisely splice PMF is presented in Section 3.8.2.

6.6.2. ERRORS DUE TO LEAKS

The leak-leak lines coincide with the main lines; this creates an offset that result in errors in the reflectivity and retardance measurement. We have maximized the main line in fast channel, and found that the leak-leak line on slow channel is 70 times smaller. Almost the same ratio was measured when the main line on the slow channel was maximized. Equation 3.17 can now be written as

$$R \propto (U_s^2 + U_x^2)(1 + 1/70) \quad \textbf{6.6}$$

which indicates that larger reflectivity error is proportional to the reflectivity itself. Equation 3.18 can also be rewritten as

$$\delta = \text{atan}\left(\frac{U_s + U_f/70}{U_f + U_s/70}\right) \quad \textbf{6.7}$$

Equations 6.6 and 6.7 are written considering that the two polarization channels are in phase. If they were out of phase, errors due to polarization leakage are smaller. When the two channels are in phase, error on the retardance measurement due to polarization leakage is plotted in Figure 6.18. The error is equal to zero when δ = 45º. Maximum errors occur when δ = 0º and 90º, where the measurement deviates from the actual value by 0.82º. Similar error was discussed in bulk PSOCT due to the finite extinction ratio between the two channels in the detection arm [28]. The finite extinction ratio also contributes, to lesser extent, to the error described here. The small error is, however, systematic and can be corrected if needed. Precise retardance measurements can be also launched in differential-phase mode as presented in CHAPTER 5.

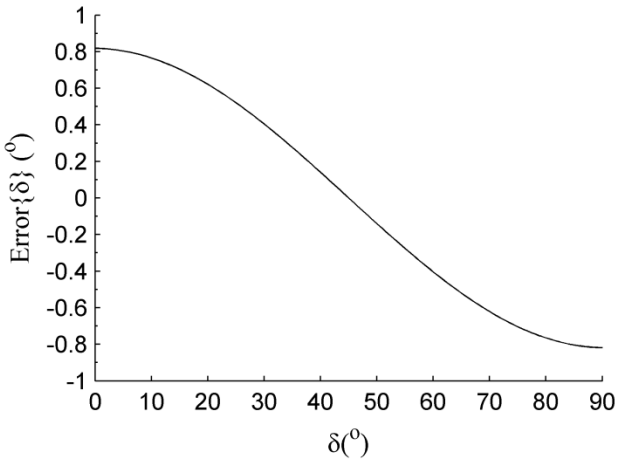

Figure 6.18 Error on the retardance measurement due to the leak-leak line.

6.6.3. ABSOLUTE AXIS ORIENTATION IMAGES

We have shown that the phase offset in the relative axis orientation images can be subtracted to measure absolute axis orientation. Because the two coherence functions are aligned, we were able to remove the phase offset by simple subtraction. In case the coherence functions were not aligned, they can be brought together, and the phase offset can be cleared, by adding a complex number to either of the coherence functions through an iterative trial and error process [87].

Environmental disturbances such as fiber movement and temperature effects can alter the correction. Perturbations are minimized by placing the PMF interferometer in an insulated enclosure. This excludes about 1 m of PMF in each arm that connects to collimators. Axis orientation images can yet be altered if the fiber is disturbed during image acquisition. At high imaging rates, environmental disturbances are usually too slow to influence a single frame. If the fibers of the sample and reference arms were not disturbed, the offset does not change even after days.

6.7 CONCLUSION

We have described and characterized a SS PSOCT based on PMF technology, and demonstrated its performance in imaging biological tissues. A single sweep of the optical spectrum is sufficient to yield polarization-diversity reflectivity, retardance, and optical axis orientation information along the A-line. System characterization and error analysis have shown that the PMF-based interferometer can measure these quantities with high accuracy. We established that PMF-based PSOCT can be implemented to have sensitivity and SNR figures comparable to bulk- or SMF-based systems. PMF-based PSOCT has therefore the potential to considerably impact scientific studies and clinical applications.

CHAPTER 7
CORRECTING THE BIREFRINGENCE IMAGES

Direct calculation of tissue birefringence using PSOCT data yields cumulative retardance images. When light experience strong birefringence in the tissue, bands in the retardance and axis orientation images are observed due to intensity inversion every quarter wave of retardance. Banding patterns contain incorrect retardance mapping, and degrade the ability to differentiate tissue boundaries in retardance images. The axis orientation images are difficult to interpret because of the banding patterns and regions when the phase noise is extremely high. We present an analysis of the origin of the banding patterns, and introduce an algorithm to correct birefringence images. We also set a limit for masking high-noise regions in the axis orientation images. Corrected birefringence images are shown and discussed to demonstrate the importance of the correction algorithm.

7.1 INTRODUCTION

Retardance and optical axis orientation of birefringent tissues are imaged using PSOCT. Retardance images have been always displayed as cumulative retardance that adds up as light propagates in a birefringent tissue. Retardance images are therefore presented with a large dynamic range, which degrades the visibility of local changes of retardance. Plotting cumulative retardance limits the ability to differentiate between tissues at the boundaries. When the imaged tissue exhibits retardance that exceeds one quarter wavelength, angle wrapping renders banding patterns that make retardance images difficult to interpret.

Axis orientation images also suffer from banding patterns in tissues with high birefringence. Because the axis orientation images are calculated from the phase information, large errors are observed at regions when the either of the interferometric signals is low. Banding patterns and large noise regions cause a severe difficulty to understand the axis orientation images.

Banding patterns are evident in the images shown in CHAPTER 3 and CHAPTER 6. They are also evident in all PSOCT papers in literature in the retardance [21, 25, 34, 38, 79, 80, 82, 83] and optical axis orientation [34, 79, 80, 82, 83] images. Bands are also shown in manuscripts that calculate Stokes parameters [35, 37], and Mueller matrix of the samples [36]. A very recent paper has demonstrated a numerical method to correct the axis orientation images [99], but the retardance images were not corrected.

In this chapter we discuss the characteristics of the calculated retardance and axis orientation, and the origin of the banding patterns. We present a method to display birefringence images as contrast images instead of increasing slopes or banding. Methods to remove the bandings from axis orientation images and to reject high-noise area to eliminate large errors are also presented. The proposed methods are applied to tissue images, and the processed

images are compared against the original to demonstrate the advantages of correcting birefringence images.

7.2 ANALYSIS

7.2.1. THEORY

We consider the interference patterns detected using a TD system, and use Equations 3.14 and 3.15 to write light intensities of the interference patterns on the orthogonal channels. When the observation is made within the coherence length of the source, the normalized and demodulated intensities for a single reflector in the sample arm can be expressed as

$$I_s = \sin\delta \tag{7.1}$$

$$I_f = \cos\delta\, e^{i(2\theta+\varphi_o)} \tag{7.2}$$

Retardance can then be calculated as

$$\delta = \operatorname{atan}\left(\frac{I_s}{I_f}\right) \tag{7.3}$$

And axis orientation as half of the phase difference between the two channels

$$\theta = \frac{\varphi_f - \varphi_s}{2} \tag{7.4}$$

The constant term, φ_o, in Equation 7.2 is dropped from Equation 7.4. The constant does not affect the discussion in this chapter, and it is dropped from the following analysis for simplicity.

Figure 7.1 shows I_s and I_f, overlaid with δ, and θ calculated using Equations 7.3 and 7.4. The calculated retardance, when unwrapped, is in fact the cumulative retardance light has gained

as it propagates deeper into the birefringent sample. The slope of δ represents the localized retardance.

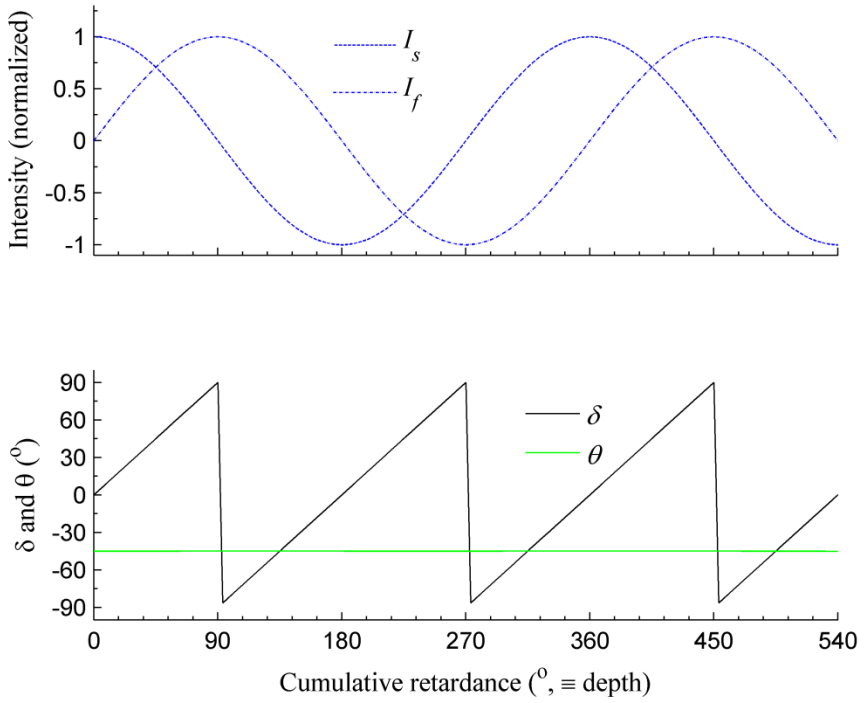

Figure 7.1 δ and θ calculated from I_s and I_f. δ represents the cumulative retardance. The phase shift between I_s and I_f, and hence θ, is constant.

Using the Hilbert transform demodulation scheme in TD OCT (CHAPTER 3), or calculating the interferometric intensities and phases using Fourier transform in FD OCT (CHAPTER 6), yields the absolute amplitudes U_s and U_f of I_s and I_f, respectively. This does not affect the measurement as long as the cumulative retardance is less than 90°; that is when sin(δ) and cos(δ) are positive. As shown in Figure 7.2, once the cumulative retardance of the tissue exceeds 90° and before it reaches 180°, the amplitude of cos(δ) is inverted. This bounds the measured δ to the range 0° to 90° (see Figure 3.7 for experimental results), and erroneously yields a negative slope δ. When the cumulative retardance of the tissue is between 180° and 270°, the

amplitude of sin(δ) is now inverted, yielding a positive slope δ. The slope of the curve therefore alternates for every 90º increase on the cumulative retardance.

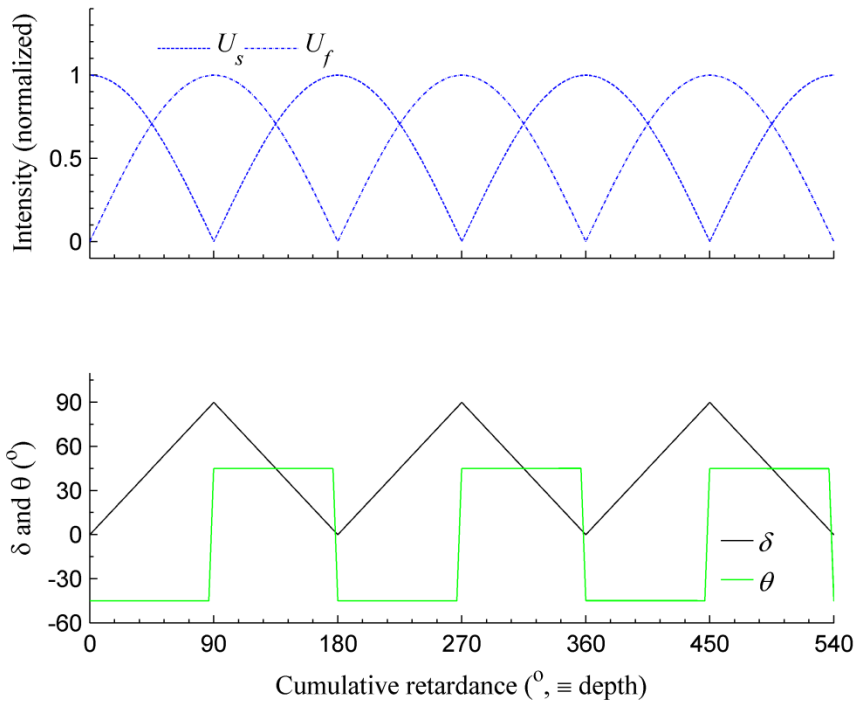

Figure 7.2 When δ and θ are calculated from the digitized U_s and U_f, amplitude inversion erroneously causes negative slope bands on δ, and phase reversal causes 90° phase shift bands on θ. The negative slope on δ and phase shift on θ occur simultaneously.

Because cos(δ) = – cos($\delta - \pi$), the amplitude inversion of the cosine is equivalent to a 180º phase shift, or phase reversal. When the tissue cumulative retardance > 180º and < 270º, another phase reversal is observed on the sin(δ). Therefore, an alternating 90º phase shift is observed on θ every time δ increases an extra 90º, see Figure 7.2. This alternating phase shift results in banding pattern in the axis orientation images. The numerical error observed on θ at the middle of the bands is because θ is actually calculated from the absolute value of the signals, not the full representation of the cosine and sine. In the actual measurement, the signals sin(δ) and cos(δ) have

a DC offset (see Section 6.6.2), which yields additional error on the phase measurement. These errors can result in banding patterns with angle difference between bands that is non-uniform, and not equal to 90º.

7.2.2. EXAMPLE DATA

Phase reversal and amplitude inversion are observed on the interference fringes of TD OCT. A good example is demonstrated by using a variable retarder in the sample arm, similar to Section 3.6.2. Increasing the retardance of the variable retarder is equivalent to penetrating deeper in a birefringence tissue. Wrapped retardance as function of voltage is shown in Figure 7.3 (a). The plots in Figure 7.3 (b) show the interference fringes on the fast and slow channels of the detection arm when δ wraps around 90º, and immediately before and after. The plots show the phase reversal on the fast interference after passing the point δ = 90º. Phase reversal on a sinusoidal waveform is equivalent to amplitude inversion. Data in the figure is collected using the frequency-multiplexed system in CHAPTER 3, the fast and slow channels therefore have different modulation frequencies. The amplitudes of the signals on the fast channel are amplified in the figure.

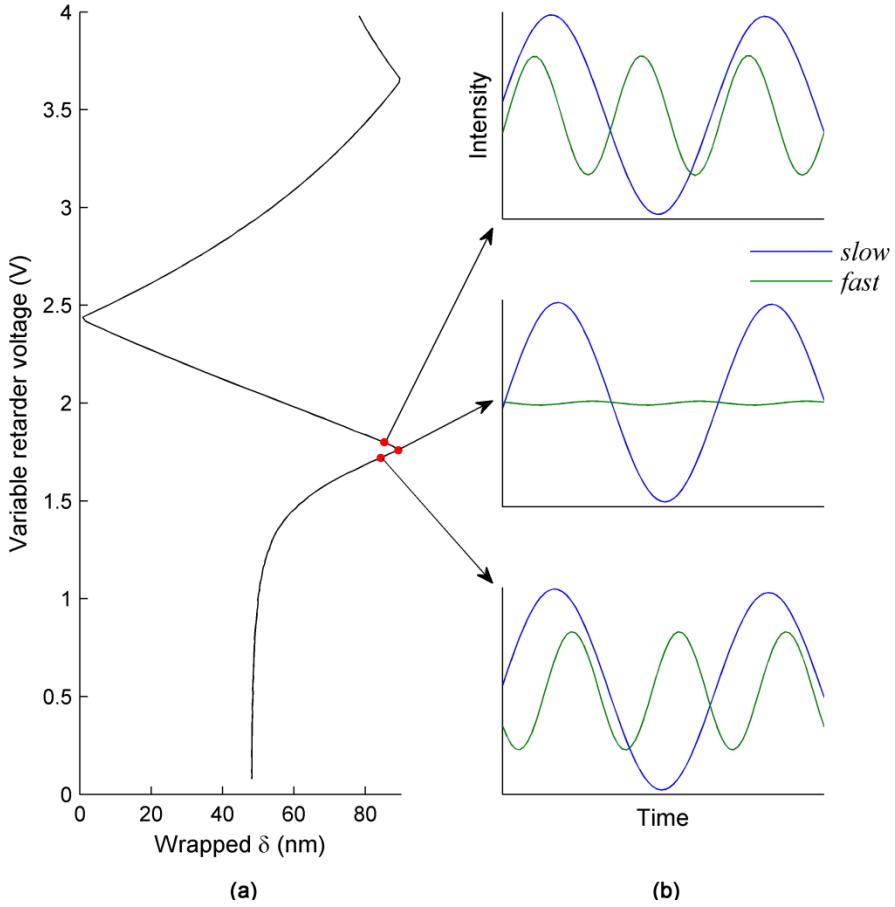

Figure 7.3 (a) Retardance of the variable retarder increases as the applied voltage increases, equivalent to penetrating deeper in a birefringence tissue, and (b) shows the interferometric fringes on the slow and fast channels around the wrapping point. Phase reversal, and consequently amplitude inversion, is observed on the slow channel. Data is collected using the frequency-multiplexed system in CHAPTER 3; the fast and slow channels therefore have different modulation frequencies.

Figure 7.4 shows the birefringence information across an A-line of the chicken muscle sample shown in Figure 6.13 (a, b). The figure shows the banding on the measured cumulative δ due to intensity inversion, and the unwrapped cumulative δ using the image processing method described in Section 7.3. Local retardance is equal to the slope of the cumulative retardance curve at the depth of interest. The figure also shows the axis orientation information (with an offset to fit in the curve) of the same A-line. The effect of phase reversal is clearly observed on the data. The

phase shift between bands is not exactly 90º, neither constant; which is expected due to the errors described above. All lines in Figure 7.4 are median-filtered to reduce speckles.

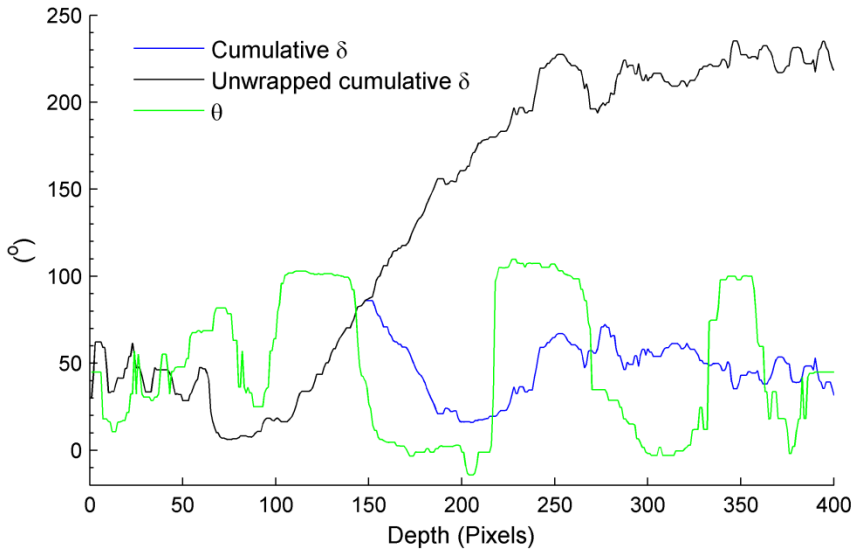

Figure 7.4 Cumulative δ and θ data from chicken muscle sample. Retardance is also shown unwrapped after correcting for the intensity inversion. Due to DC offsets and numerical errors, the alternating phase shifts on θ can take a value other than 90º.

7.3 METHOD

7.3.1. CORRECTING RETARDANCE IMAGES

Retardance image is calculated as usual, and a Canny edge detection algorithm [100] is applied to detect the points at largest slopes (when $\delta \approx 45º$), see the green lines in the example in Figure 7.5. The top surface of the sample is also detected. These are not the lines of retardance wrapping; therefore one adjust increase the width of the Gaussian window in Canny detector, and change the threshold to make sure that all bands are captured (an automatic adjustment algorithm is presented in 7.5.1). Speckles in the retardance image are now smoothed using a two-dimensional square-windowed median filter, and the smoothed image is divided into segments

based on the edges detected earlier. Wrapping points are found by finding the maxima or minima in each segment; see the red lines in Figure 7.5.

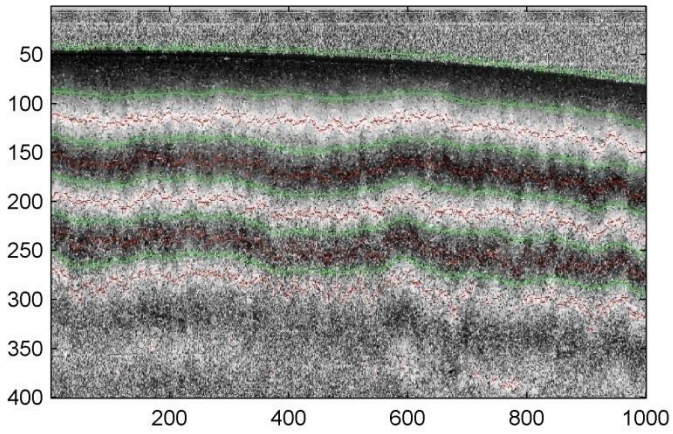

Figure 7.5 The green lines are detected using a Canny edge detection algorithm. The red lines used as boundaries for the bands, are calculated as the maxima or the minima of the segments between the green lines.

Let's consider Figure 7.2 again, right after I_s first reaches zero at δ = 90º, the cosine function is phase-shifted by a 180º. If this point is considered the time origin, I_s is actually described by a sine function, and I_f by a cosine; recall that $|\sin(\delta + 90º)| = |\cos(\delta)|$ and $|\cos(\delta + 90º)| = |\sin(\delta)|$. Therefore, negative slopes in the retardance image are inverted by calculating retardance as $\delta = \text{atan}(U_f/U_s)$ for the corresponding bands. Retardance is still calculated as $\text{atan}(U_s/U_f)$ when the original slope is positive. If bands are numbered from top to bottom, the correct retardance is calculated as

$$\delta = \begin{cases} \text{atan}\left(U_f/U_s\right), & \text{odd bands} \\ \text{atan}\left(U_s/U_f\right), & \text{even bands} \end{cases} \qquad \textbf{7.5}$$

This is actually a more accurate representation because the double-passing the first band is equivalent to a half wave plate.

Retardance is unwrapped by processing the unsmoothed image at the red lines in Figure 7.5. For each A-line, the last point and the first point in two consecutive bands are averaged and added to all the values in the second band in the same A-line. The dynamic range of the directly-calculated retardance is less than 90º as the signal intensity decays; therefore, unwrapping retardance information by adding additional 90º for each new band generates large errors at the wrapping points.

Speckle noise in the corrected and unwrapped cumulative retardance images is minimized by a two-dimensional median filter with a larger dimension along the depth of the sample. Local retardance is calculated as degrees per pixel by calculating the derivative along the depth of filtered image; the derivative is calculated as the difference between each consecutive pixels. The derivative image is multiplied by the ratio of the number of points in the A-line over the imaging depth; and local retardance is then represented as degrees/mm. If the cumulative retardance in the sample did not originally exceed 90º and banding is not present in the image, the slope correction and unwrapping steps and skipped and the local retardance is calculated as described.

7.3.2. Correcting Optical Axis Orientation Images

Axis orientation images are corrected when the cumulative retardance is larger than 90º. The edges at the boundaries of the bands are detected using a Canny edge detection algorithm. A constant phase shift around 90º is added to every other band starting after the first edge. Two-dimensional median filtering is sometimes applied to the corrected image to reduce speckle noise. An example of edge detection of the boundaries of the bands in the axis orientation image is shown in Figure 7.6. The phase jumps at the boundaries of the bands are abrupt, and the edges are not difficult to detect. Small errors in edge detection, however, are acceptable because the regions around the boundaries are large-noise regions and will be rejected as discussed in the next subsection.

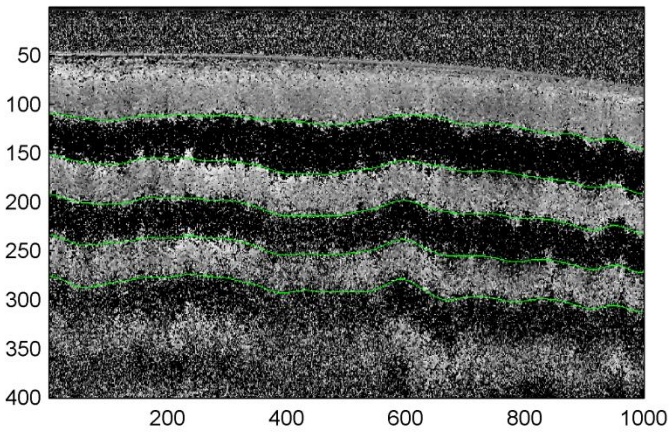

Figure 7.6 Optical axis orientation images are corrected by adding a constant to every other band (the dark bands here). The green lines are detected using a Canny edge detector.

7.3.3. Rejecting the High-Noise Regions in Axis Orientation Images

Optical axis orientation images are calculated from the phase signal on I_s and I_f. Axis orientation measurement is therefore noisy when either of the channels is noisy. Axis orientation images are typically masked at low reflectivity levels. The reflectivity measurement can however be large even if there is no signal on one of the channels. We define two masks that reject low signal levels on each channel separately, and then mask the axis orientation image with the two masks combined. The low-reflectivity mask will still be used to mask retardance images. To differentiate between the two masks, the axis orientation mask calculated from the amplitude on each individual channel is called the amplitude mask.

As described in Section 2.3.4, the standard deviation of phase noise, σ_θ, in radians is inversely proportional to the linear SNR of the amplitudes U_s and U_f. Axis orientation images are masked in the regions when the SNR of the of either of U_s and U_f drops below a threshold, typically 15, equivalent to about 1.5° standard deviation phase noise.

7.4 RESULTS[22]

7.4.1. IMAGES OF TISSUES WITH LOW CUMULATIVE RETARDANCE

To demonstrate the significance of correcting retardance images, images of porcine iris in the eye globe are shown in Figure 7.7. The data was acquired after removing the birefringent corneal tissue. Histological image of a porcine iris stained to differentiate muscle tissues is shown in Figure 7.8; the stroma is not well-differentiated from the anterior border layer in the histology image. The cumulative retardance image shows that the iris tissues exhibit birefringence. It is however difficult to differentiate between tissues in the cumulative retardance image. The local retardance image, on the other hand, shows that the circularly-arranged sphincter smooth muscle, and the anterior (upper) portion of the stroma exhibit strong birefringence; and the anterior border layer exhibit weaker birefringence properties.

A strong difference in birefringence properties between anterior and posterior (lower) segments of the stroma is observed. PSOCT reflectivity image also indicates that the stromal reflectivity is not the same in the two segments. The stroma is composed of collagen fibers, fibroblast, blood vessels and nerves. Stromal collagen fibers are aligned with the fibroblasts around the blood vessels; they form a loose matrix elsewhere [101]. The histology image shows that the density of the blood vessel, and consequently aligned collagen fibers, in the anterior stroma is higher than the posterior; justifying the strong birefringence in the anterior stroma, and its absence in the posterior stroma. The axis orientation images in Figure 7.7 demonstrate the significance of masking regions with large noise error. The posterior stromal tissue, for example, shows misleading information before masking.

---

[22] All images in this section were acquired *ex vivo* using the PMF-based system presented in CHAPTER 6

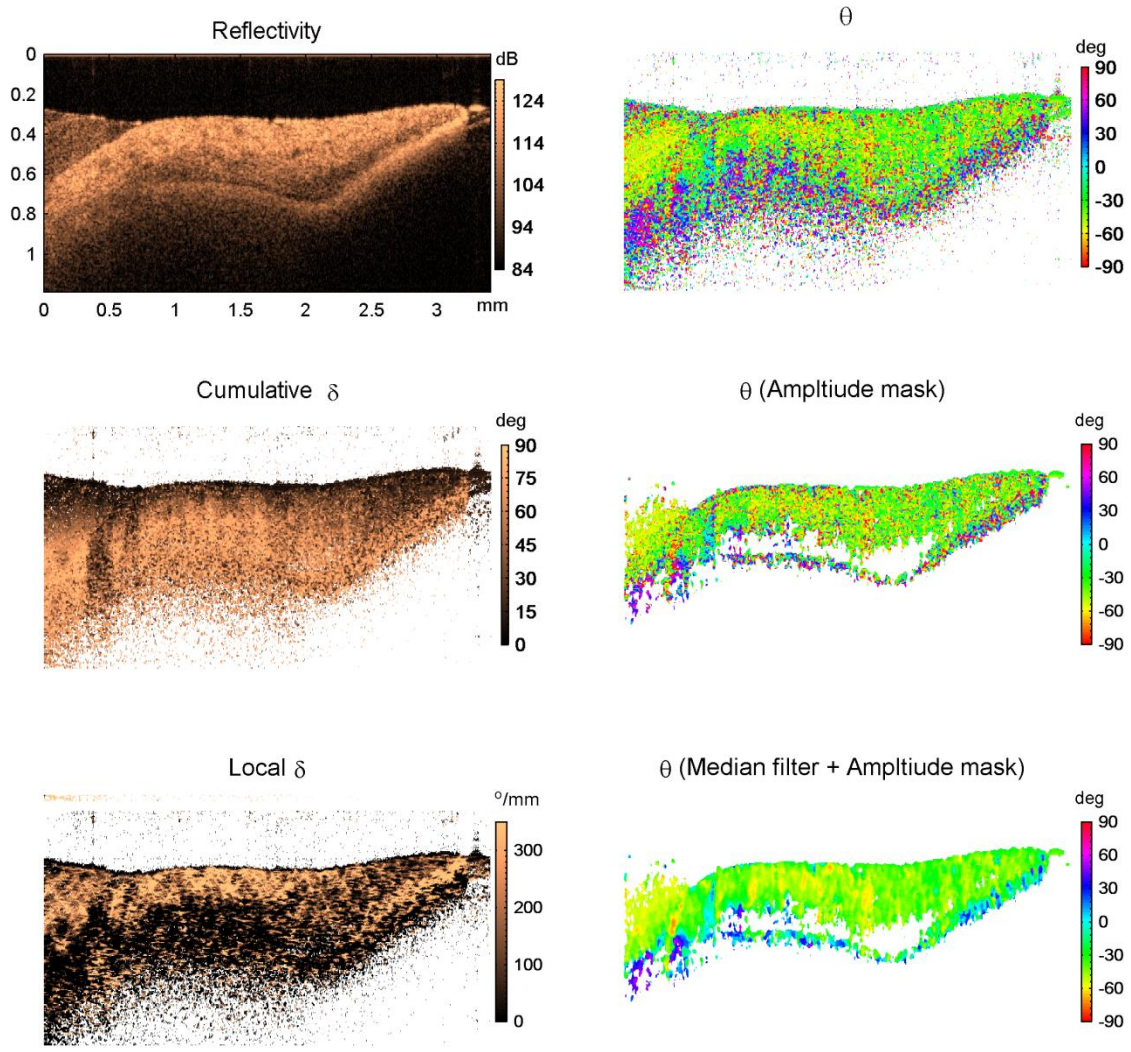

Figure 7.7 Raw and processed PSOCT images of a porcine iris. Images were taken after removing the cornea. Contrary to the cumulative retardance image, the local retardance image reveals structures that can be correlated to the reflectivity image. The axis orientation image, *θ*, misleadingly shows regions with invalid measurements. The same image is shown after amplitude masking to remove the invalid regions, and median filtering to reduce speckles.

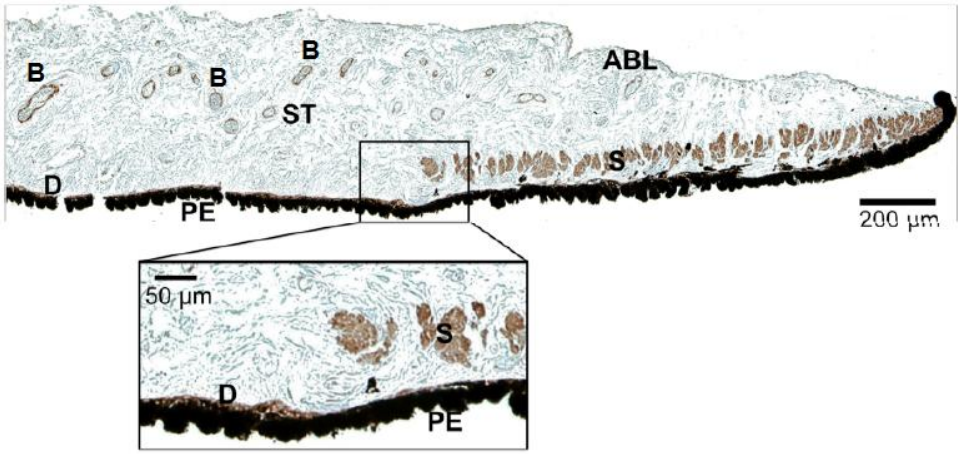

Figure 7.8 Histology section of a porcine iris. S – sphincter or constrictor pupillae, D – dilator, ST - stroma, PE - pigment epithelium, ABL – anterior border layer, B – blood vessel. The stroma is not differentiated well from the anterior border layer.

Raw and processed PSOCT images of human bladder tissue are shown in Figure 7.9. The local retardance image shows that the tissue is not uniformly birefringent. Masking the axis orientation image at lower light intensities rejects large noise regions, see the circled region. The variation of the axis orientation of the tissue is shown nicely in the masked and filtered image.

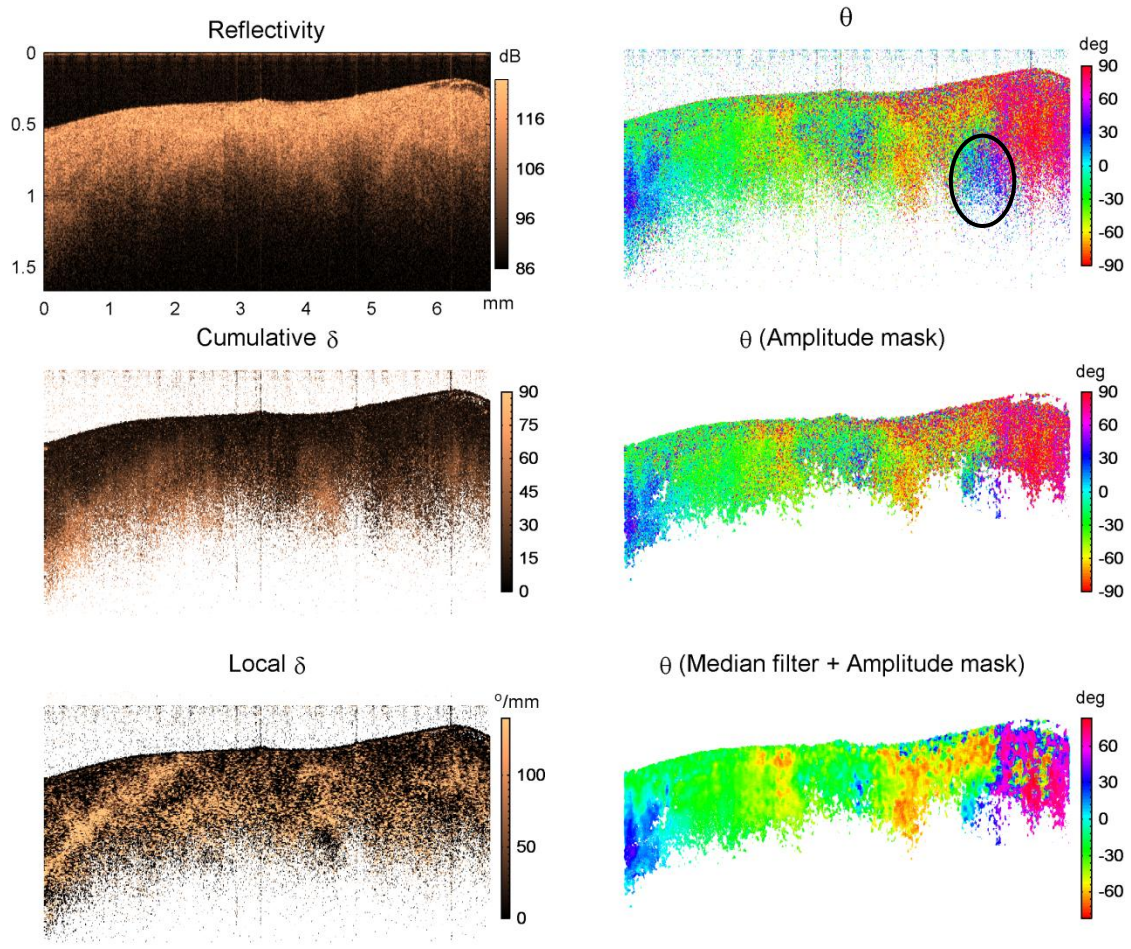

Figure 7.9 PSOCT images of human bladder tissue. The local retardance image shows accurate representation of the birefringent structures. Masking the axis orientation image rejects the circled region where high noise level disturbs the measurement.

7.4.2. Retardance Images of High-Birefringence Tissues

Reflectivity and retardance images of chicken muscle tissue are shown in Figure 7.10. The same dataset was used to plot Figure 6.13 (a) and (c). The corrected and unwrapped cumulative retardance image has a high dynamic range; which degrades the visibility of local retardance changes. The local retardance image shows a thin non-birefringent tissue on top of the muscle tissue (green arrow), and a region where the birefringence local birefringent varies (green ellipse). The two structures are not visible in the cumulative retardance images. These structures correlate

to the reflectivity image. The retardance measured from the local retardance image is in agreement with the measurement in Section 6.5. Figure 7.11 shows another set of images at a different location in the same muscle tissue. One can notice that the non-birefringent tissue is also visible in the local and not the cumulative retardance image. The birefringence properties of the muscle tissues shown in the two figures are slightly different.

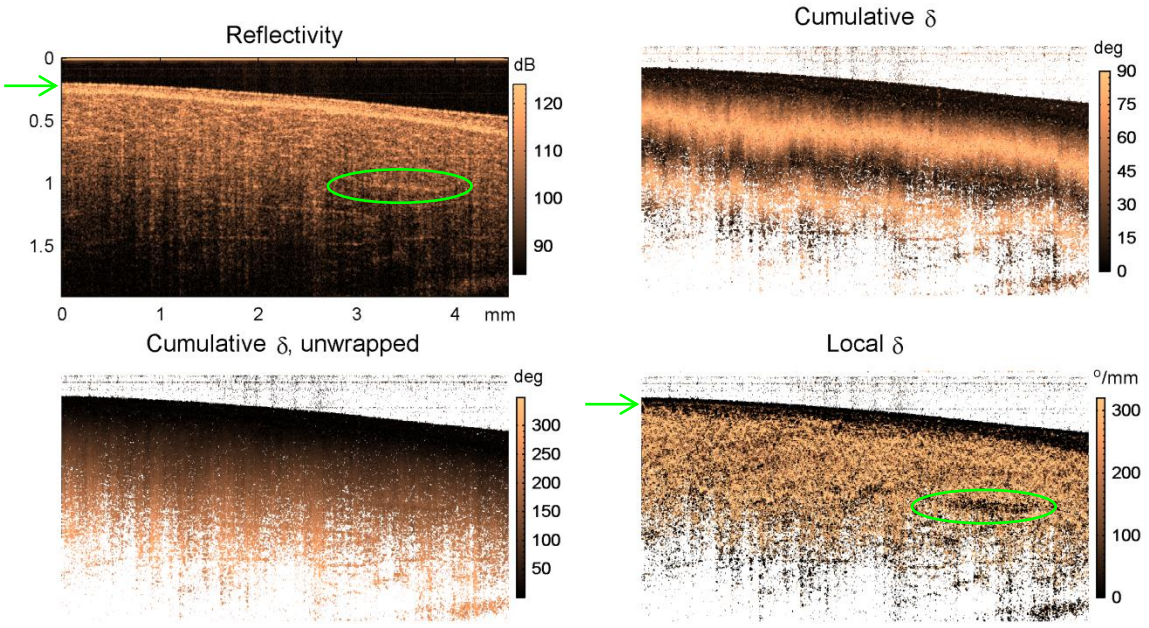

Figure 7.10 PSOCT reflectivity and retardance images of a chicken muscle. The local retardance reveals structure and boundaries, indicated in green, that are invisible in the cumulative retardance images. The structures shown in the local retardance image correlate with the reflectivity image.

Figure 7.12 shows image of a tendon tissue in a chicken leg. The upper non-birefringent tissue is invisible in neither of the reflectivity nor the cumulative retardance images. A lower boundary of the tendon tissue can be seen in the reflectivity image. Both boundaries are, however, clearly visible in the local retardance image. A close look at the cumulative retardance image shows that banding stops below the tendon tissue, but the boundary between the two tissues is not discernable. The local retardance image also shows that the birefringence of the tendon tissue is three to four times stronger than that of the muscle tissues shown above.

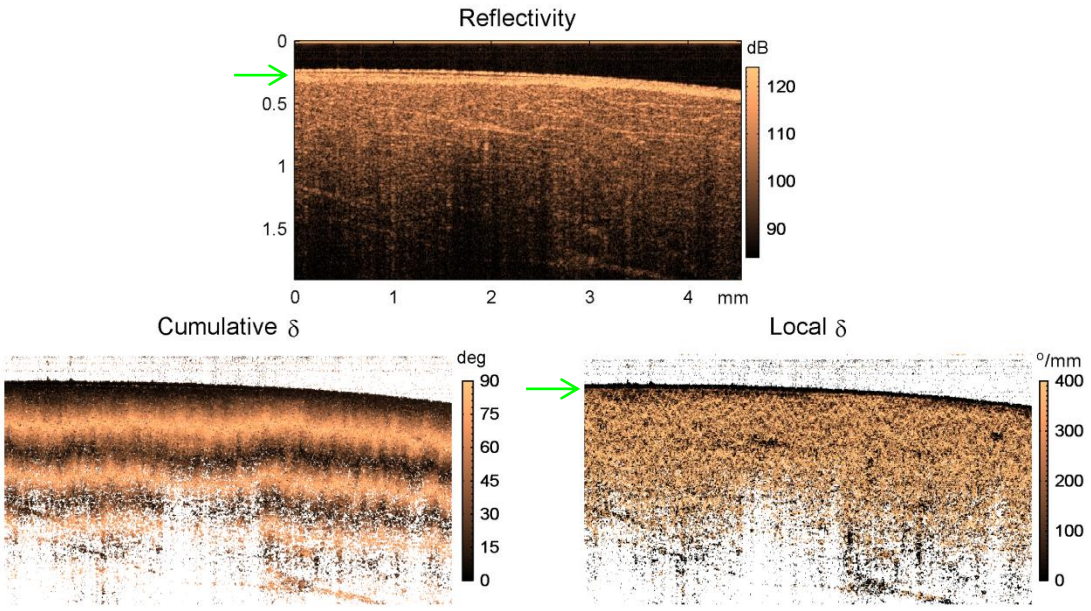

Figure 7.11 PSOCT reflectivity and retardance images of a chicken muscle. The non-birefringent tissue, indicated in the local retardance and reflectivity images, is not visible in the cumulative retardance image

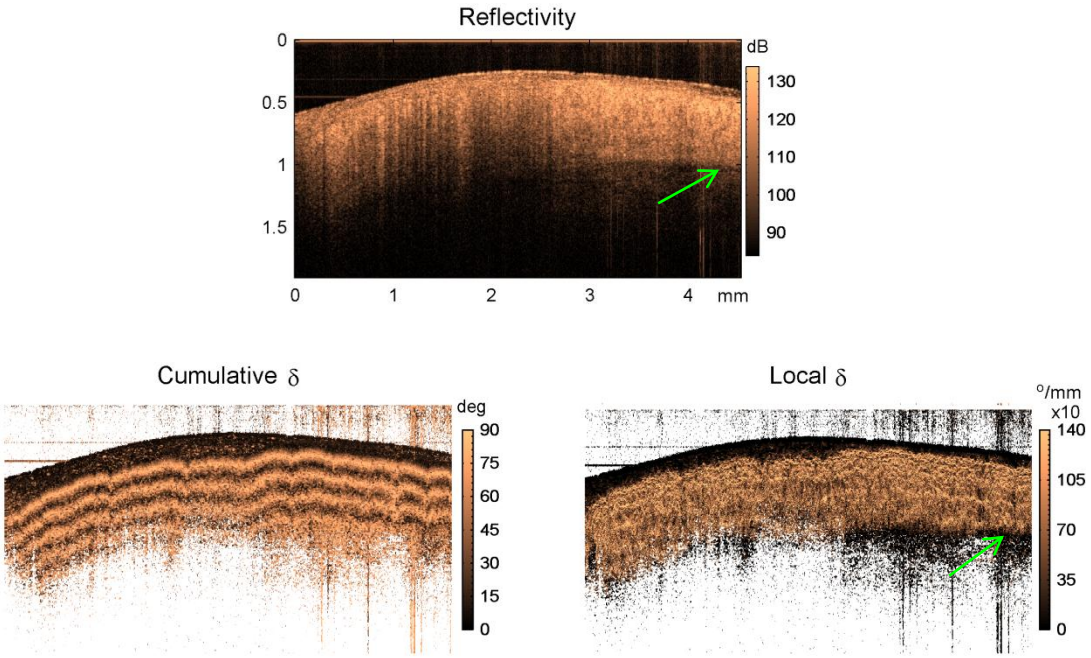

Figure 7.12 PSOCT reflectivity and retardance images of a tendon tissue in a chicken leg. It is difficult to determine the boundaries of the birefringent tendon tissue in the cumulative retardance image. The lower boundary is a discerned in the reflectivity image. Both boundaries are clearly visible in the local retardance image.

7.4.3. Optical Axis Orientation Images of High-Birefringence Tissues

Optical axis orientation image of the same cross-section presented in Figure 7.11 is shown in Figure 7.13. Banding due to phase reversal is seen in the uncorrected image. The corrected image shows a roughly uniform orientation of the optical axis across the image. In the unmasked corrected image, large errors are mainly observed at the boundaries of banding. In the masked image, only axis orientation information with acceptable noise level is displayed. To demonstrate the efficacy of the image processing method to correct axis orientation images with closely-packed bands, corrected and masked axis orientation of the tendon tissue is shown in Figure 7.14. The corrected axis orientation image of the two angled chicken muscle slabs is shown in Figure 6.14.

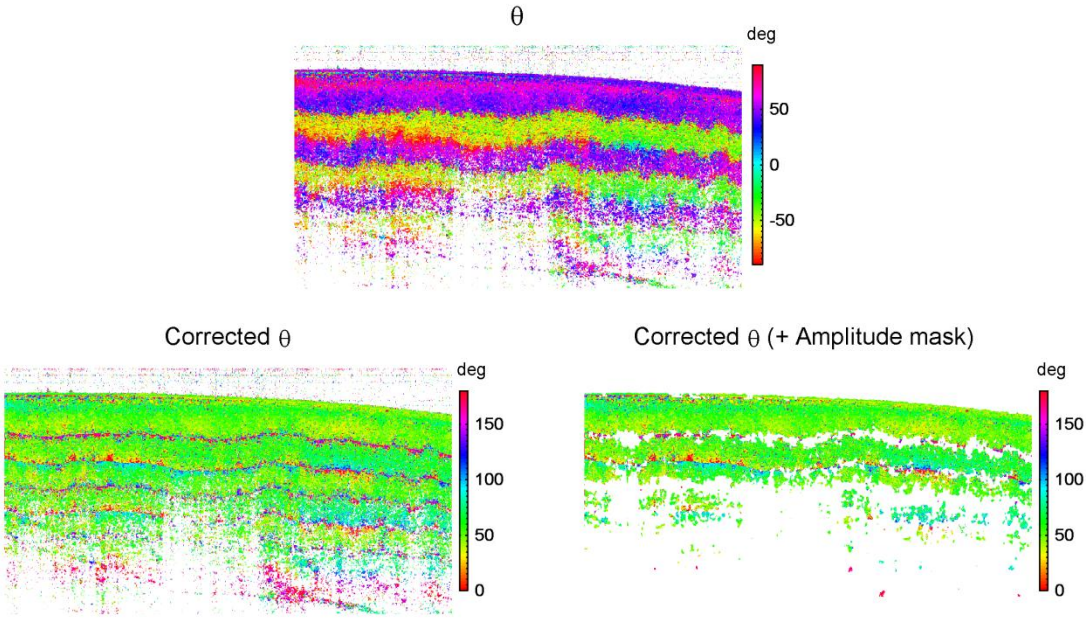

Figure 7.13 Optical axis orientation images of the tissue shown in Figure 7.11. The correction removes the phase jumps from the original image, and shows a roughly uniform orientation of the muscle fibers. Amplitude masking removes the regions where large noise levels alter the image.

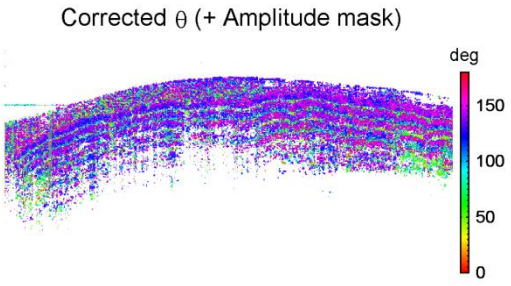

Figure 7.14 Corrected and masked optical axis orientation image of the tendon tissue shown in Figure 7.12. The correction algorithm is efficient even at closely-packed banding pattern.

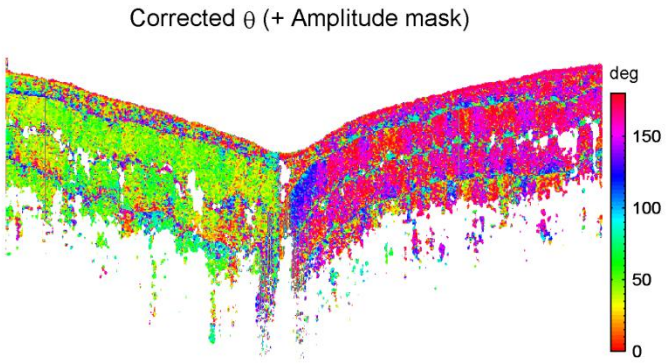

Figure 7.15 Corrected and masked optical axis orientation image of the angled muscle tissue slabs shown in Figure 6.14.

7.5 Discussion

7.5.1. Automatic Adjustment of the Gaussian Window of Canny Edge Detector

The algorithm presented here detects the boundaries of the bands in PSOCT images using an image processing algorithm. The algorithm is based on Canny edge detector, which is designed to optimize "good detection, good localization, and only one response to a single edge" [100]. Like any other image processing algorithm, the detection parameters may need to be slightly adjusted when the features of the image are largely different. For example, the bands in the chicken muscle images are considerably broader than those in case of the tendon; a larger Gaussian window in Canny detector was therefore used to process the chicken images.

Manual adjustment is abandoned by employing an algorithm that detects the frequency of the banding pattern, and scaling the window size accordingly. Figure 7.16 shows the Fourier transform along the axial dimension of the uncorrected retardance images shown in Figure 7.10, Figure 7.11, and Figure 7.12. We have, in fact, scaled the edge detector window based on outcome of the data in Figure 7.16 to demonstrate the feasibility of automatic scaling of the window.

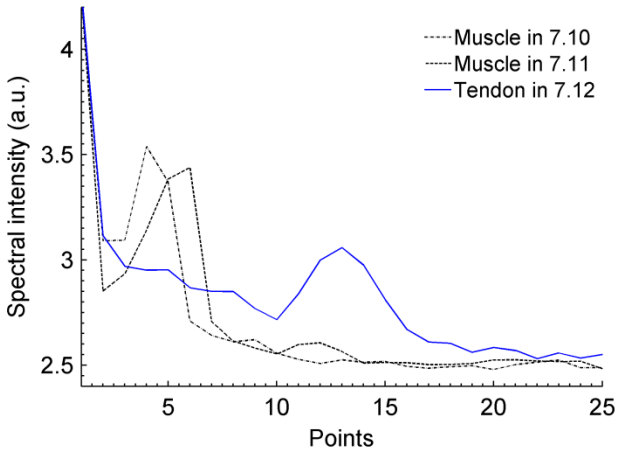

Figure 7.16 Spectral data from the uncorrected retardance images shown in the indicated figures. The frequency of the banding pattern is automatically-detected to scale the Gaussian window of Canny detector.

7.5.2. TOWARDS A FULLY-AUTOMATED ALGORITHM

In tissues with very high birefringence, bands are very thin and closely-spaced. In this case, the number of points along the axial direction is doubled or tripled using a linear interpolation method before applying the edge detection algorithm. To correctly detect the edges in the uncorrected axis orientation image of the tendon tissue, the original number of points along the axial dimension was doubled before applying the edge detector. Based on the same Gaussian window adjustment algorithm above, a simple subroutine might be added to the algorithm to determine when to increase the number of points in the image.

The sensitivity thresholds of the edge detector were adjusted manually. Lower threshold levels were set to process the tendon image. Because the dynamic range of the uncorrected retardance image is fixed at 0º to 90º, and the speckle noise is similar in all images, it might be possible to develop an automatic sensitivity adjustment algorithm. A method to check for acceptable continuity of the detected edges will aid accomplishing a fully-automated algorithm.

7.5.3. Phase Reversal Correction in Axis Orientation Images

Perfect phase reversal produces an exact 90º jump between bands in the uncorrected axis orientation images. Practically, DC offset and errors in the polarization components produce phase jumps larger or smaller than 90º. The phase jumps in the images presented above were manually-adjusted until two consecutive bands show the same measurement of the axis orientation. The phase jumps were found to vary between 85º and 110º. Realignments in the optic components, like rotating the QWP in the sample arm, may influence this error; and it will therefore be useful to measure the error, calibrate the system, and fix the interferometer optics.

7.6 Conclusion

We presented an analysis of the origin of the banding patterns in PCOST birefringence images. The difficulty to visualize fine structures when displaying cumulative retardance images was discussed. A novel algorithm was developed to correct the banding pattern in birefringence images, and calculate images of local retardance. Corrected birefringence images of various tissues were presented to demonstrate the efficacy of the new algorithm. The corrected images have revealed information that are otherwise invisible, which emphasizes the importance of correcting PSOCT birefringence images.

CHAPTER 8
SUMMARY

We have demonstrated a new approach to implement PSOCT using PMF. PMF-based PSOCT interferometers in TD and FD are presented. Characterization of the systems, in addition to area and volume images of tissues demonstrates the feasibility of the approach. Bulk-optics PSOCT implementations are straightforward and simple, but usually lack the flexibility needed in clinical and laboratory setups. Conventional SMF-based PSOCT systems employ expensive phase modulators, polarization-controllers, multiple measurements, and extensive processing. Usually, upgrading a SMF-based OCT system to PSOCT is impossible, or as expensive as the base system. The new approach enables simple optical designs at lower cost and better characteristics.

Building PSOCT using PMF yields two major benefits: (1) PMF is immune to external perturbations. Therefore, the measurement is not influenced by the fiber movement. This gives the systems the flexibility and stability required to incorporate PSOCT systems in clinics for *in situ* and endoscopic imaging. (2) PMF maintains the polarization state of two independent propagating polarization states, making it possible to measure two complex quantities in a single measurement and calculate tissue reflectivity and birefringence using compensation-free and computationally-inexpensive algorithms.

It is essential to demonstrate that the advantages of PMF-based PSOCT do not compromise the sensitivity of conventional systems. We have compared the sensitivity of a PMF system with equivalent OCT system based on SMF. Using a standard reflector in the sample arm, the sensitivity of the PMF-based interferometer was found similar to that in the SMF-based system. We have also demonstrated that useful subsystems, like balanced detection and rapid scanning optical delay lines, can be incorporated with PMF-based PSOCT.

In PMF-based interferometer, light in the orthogonal channels propagates a common optical path, and complex measurements of two channels are recorded simultaneously. This enables differential-phase measurements with sensitivity that approaches the theoretical value. This measurement would not have been possible if conventional SMF had been utilized.

We have employed the superior phase sensitivity of the PMF-based PSLCI for sensitive measurement of Faraday rotation. The measurement was demonstrated with field-depth factors two orders of magnitude lower than common techniques. The reflection-mode measurement was demonstrated in tissue-mimicking phantoms. The measurement is potentially applicable for imaging of Faraday rotation in tissues, and understanding of magneto-optical interactions in biology.

The high sensitivity of the phase measurement was also employed in investigations of the birefringence of unmyelinated nerves. Several nerve models were studied and imaged; we believe this is the first time that depth-resolved retardance of unmyelinated nerves has been mapped. Resting retardance of the nerve models was quantified, which has enabled the calculation of the expected retardance change during neural activity. It is important for future investigations in the field to consider the resting retardance distribution within the nerve, and the expected level of retardance change during neural activity.

The common representation of PSOCT retardance images displays cumulative retardance images. We believe that further processing to calculate local retardance images and display retardance as a contrast rather than horizontal bands. An analysis of the calculation of birefringence images was presented. We have found that the currently accepted representation of birefringence images contains errors. The origin of the errors was indicated, and a correction algorithm was presented and tested. The algorithm identifies regions with errors and applies the appropriate equations to the corresponding regions. Local retardance is calculated from the corrected images. Phase jumps in axis orientation images were also discussed and corrected and a criterion to identify and mask regions in the orientation images with inadequate accuracy was presented. Several images of birefringent tissues were presented to demonstrate the importance of displaying local retardance, and corrected axis orientation.

REFERENCES

1. D. Huang, E. Swanson, C. Lin, J. Schuman, W. Stinson, W. Chang, M. Hee, T. Flotte, K. Gregory, C. Puliafito, J. Fujimoto, "Optical coherence tomography," Science 254, 1178-1181 (1991)
2. G. J. Tearney, B. E. Bouma, and J. G. Fujimoto, "High-speed phase- and group-delay scanning with a grating-based phase control delay line," Optics Letters 22, 1811-1813 (1997)
3. E. A. Swanson, D. Huang, M. R. Hee, J. G. Fujimoto, C. P. Lin, and C. A. Puliafito, "High-speed optical coherence domain reflectometry," Optics Letters 17, 151-153 (1992)
4. A. Rollins, S. Yazdanfar, M. Kulkarni, R. Ung-Arunyawee, and J. Izatt, "In vivo video rate optical coherence tomography," Optics Express 3, 219-229 (1998)
5. A. Fercher, C. Hitzenberger, G. Kamp and S. El-Zaiat, "Measurement of intraocular distances by backscattering spectral interferometry," Optics Communications 117, 43-48, (1995).
6. G. Hausler, M. Lindner, " "Coherence Radar" and "Spectral Radar" – New Tools for Dermatological Diagnosis," Journal of Biomedical Optics 3, 21-31, (1998).
7. M. Wojtkowski, R. Leitgeb, A. Kowalczyk, T. Bajraszewski, A. Fercher, "In vivo human retinal imaging by Fourier domain optical coherence tomography," Journal of Biomedical Optics 7, 457-463 (2002).
8. S. R. Chinn, E. Swanson, J. G. Fujimoto, "Optical coherence tomography using a frequency-tunable optical source, " Optics Letters 22, 340-342 (1997)
9. B. Golubovic, B. E. Bouma, G. J. Tearney, and J. G. Fujimoto, "Optical frequency-domain reflectometry using rapid wavelength tuning of a Cr4+:forsterite laser, " Optics Letters 22, 1704-1706 (1997)
10. F. Lexer, C. K. Hitzenberger, A. F. Fercher, and M. Kulhavy, "Wavelength-tuning interferometry of intraocular distances," Applied Optics 36, 6548-6553 (1997).
11. R. Leitgeb, C. Hitzenberger, and A. Fercher, "Performance of fourier domain vs. time domain optical coherence tomography," Optics Express 11, 889-894 (2003)
12. M. Choma, M. Sarunic, C. Yang, and J. Izatt, "Sensitivity advantage of swept source and Fourier domain optical coherence tomography," Optics Express 11, 2183-2189 (2003)
13. J. F. de Boer, B. Cense, B. H. Park, M. C. Pierce, G. J. Tearney, and B. E. Bouma, "Improved signal-to-noise ratio in spectral-domain compared with time-domain optical coherence tomography," Optics Letters 28, 2067-2069 (2003)
14. W. Sorin and D. Baney, "A simple intensity noise reduction technique for optical low coherence reflectometry," IEEE Photonics Technology Letters 4, 1404–1406 (1992)

15. B. Park, M. C. Pierce, B. Cense, S. Yun, M. Mujat, G. Tearney, B. Bouma, and J. de Boer, "Real-time fiber-based multi-functional spectral-domain optical coherence tomography at 1.3 μm," Optics Express 13, 3931-3944 (2005)

16. J. Brinckmann, H. Notbohm, and P. Müller, Collagen: primer in structure, processing, and assembly, 1st edition, (Springer, 2005)

17. P. Fratzl, Collagen, Structure and Mechanics, 1st edition, (Springer, 2008)

18. B. Alberts, D. Bray, D. Bray, K. Hopki, A. Johnson, J. Lewis, J. Lewis, M. Raff, K. Roberts, P. Walter, Tissues and Cancer in "Essential Cell Biology", 2nd edition, (Garland Science/Taylor & Francis Group, September 2003)

19. I. Richter, P. Sun, F. Xu, and Y. Fainman, "Design considerations of form birefringent microstructures," Applied Optics 34, 2421-2429 (1995)

20. M. Kobayashi, H. Hanafusa, K. Takada, and J. Noda, "Polarization-Independent Interferometric Optical-Time-Domain Reflectometer," IEEE Journal of Lightwave Technology 9, 623-628 (1991).

21. M. J. Everett, K. Schoenenberger, B. W. Colston, Jr., and L. B. Da Silva, "Birefringence characterization of biological tissue by use of optical coherence tomography," Optics Letters 23, 228-230 (1998)

22. J. F. de Boer, S. M. Srinivas, B. H. Park, T. H. Pham, Z. Chen, T. E. Milner, and J. S. Nelson, "Polarization effects in optical coherence tomography of various biological tissues," IEEE Journal of Selected Topics in Quantum Electronics 5, 1200-1204 (1999)

23. S. Jiao and M. Ruggeri, "Polarization effect on the depth resolution of optical coherence tomography," Journal of Biomedical Optics 13 (6), 060503 (2008)

24. M. R. Hee, D. Huang, E. A. Swanson, and J. G. Fujimoto, "Polarization-sensitive low-coherence reflectometer for birefringence characterization and ranging," Journal of Optical Society of America B 9, 903- (1992)

25. J. F. de Boer, T. E. Milner, M. J. van Gemert, and J. S. Nelson, "Two-dimensional birefringence imaging in biological tissue by polarization-sensitive optical coherence tomography," Optics Letters 22, 934-936 (1997)

26. K. Kim, J. Burns, J. Bernstein, G. Maguluri, B. Park, and J. de Boer, "In vivo 3D human vocal fold imaging with polarization sensitive optical coherence tomography and a MEMS scanning catheter," Optics Express 18, 14644-14653 (2010)

27. R. Kuranov, V. Sapozhnikova, I. Turchin, E. Zagainova, V. Gelikonov, V. Kamensky, L. Snopova, and N. Prodanetz, "Complementary use of cross-polarization and standard OCT for differential diagnosis of pathological tissues," Optics Express 10, 707-713 (2002)

28. K. Schoenenberger, B. W. Colston, D. J. Maitland, L. B. Da Silva, and M. J. Everett, "Mapping of Birefringence and Thermal Damage in Tissue by use of Polarization-Sensitive Optical Coherence Tomography," Applied Optics 37, 6026-6036 (1998)

29. B. Park, C. Saxer, T. Chen, S. Srinivas, J. Nelson and J. de Boer, "In vivo burn depth determination by high-speed fiber-based polarization sensitive optical coherence tomography," J. Biomed. Optics 6, 474-479 (2001).

30. W. Drexler, D. Stamper, C. Jesser, X. Li, C. Pitris, K. Saunders, S. Martin, M. B. Lodge, J. Fujimoto, M. Brezinski, "Correlation of collagen organization with polarization sensitive

imaging of in vitro cartilage: implications for osteoarthritis", Journal of Rheumatology 28, 1311-1318, (2001)

31. W. Kuo, N. Chou, C. Chou, C. Lai, H. Huang, S. Wang, and J. Shyu, "Polarization-sensitive optical coherence tomography for imaging human atherosclerosis," Applied Optics 46, 2520-2527 (2007)
32. E. Götzinger, M. Pircher, I. Dejaco-Ruhswurm, S. Kaminski, C. Skorpik, and C. K. Hitzenberger, "Imaging of birefringent properties of keratoconus corneas by polarization-sensitive optical coherence tomography," Invest. Ophthalmol. Vis. Sci. 48(8), 3551–3558 (2007).
33. M. G. Ducros, J. D. Marsack, H. G. Rylander III, S. L. Thomsen, and T. E. Milner, "Primate retina imaging with polarization-sensitive optical coherence tomography," Journal of the Optical Society of America A 18, 2945-2956 (2001)
34. C. Hitzenberger, E. Goetzinger, M. Sticker, M. Pircher, and A. Fercher, "Measurement and imaging of birefringence and optic axis orientation by phase resolved polarization sensitive optical coherence tomography," Optics Express 9, 780-790 (2001)
35. J. F. de Boer, T. E. Milner, and J. S. Nelson, "Determination of the depth-resolved Stokes parameters of light backscattered from turbid media by use of polarization-sensitive optical coherence tomography," Optics Letters 24, 300-302 (1999)
36. G. Yao and L. V. Wang, "Two-dimensional depth-resolved Mueller matrix characterization of biological tissue by optical coherence tomography," Optics Letters 24, 537-539 (1999)
37. C. E. Saxer, J. F. de Boer, B. H. Park, Y. Zhao, Z. Chen, and J. S. Nelson, "High-speed fiber based polarization-sensitive optical coherence tomography of in vivo human skin," Optics Letters 25, 1355-1357 (2000)
38. J. Roth, J. A. Kozak, S. Yazdanfar, A. M. Rollins, and J. A. Izatt, "Simplified method for polarization-sensitive optical coherence tomography," Optics Letters 26, 1069-1071 (2001)
39. D. Davé and T. E. Milner, "Optical low-coherence reflectometer for differential phase measurement," Optics Letters 25, 227-229 (2000)
40. D. Digant, T. Akkin, T. E. Milner, and G. Rylander III, "Phase-sensitive frequency-multiplexed optical low-coherence reflectometery", Optics Communications 193, 39-43 (2001)
41. D. Davé, T. Akkin, and T. E. Milner, "Polarization-maintaining fiber-based optical low-coherence reflectometer for characterization and ranging of birefringence," Optics Letters 28, 1775-1777 (2003)
42. E. Smith, A. V. Zvyagin, and D. D. Sampson, "Real-time dispersion compensation in scanning interferometry," Optics Letters 27, 1998-2000 (2002)
43. C. Yuchuan and L. Xingde, "Dispersion management up to the third order for real-time optical coherence tomography involving a phase or frequency modulator," Optics Express 12, 5968–5978 (2004)
44. B. Saleh and M. Teich, Fundamentals of Photonics, 2nd edition (Wiley-Interscience, 2007)
45. A. M. Weiner, D. E. Leaird, J. S. Patel, and J. R. Wullert, "Programmable femtosecond pulse shaping by use of a multielement liquid-crystal phase modulator," Optics Letters 15, 326-328 (1990)

46. K. Kwong, D. Yankelevich, K. Chu, J. Heritage, and A. Dienes, "400-Hz mechanical scanning optical delay line," Optics Letters 18, 558-560 (1993)

47. W. Yang, D. Keusters, D. Goswami, and W. Warren, "Rapid ultrafine-tunable optical delay line at the 1.55-μm wavelength," Optics Letters 23, 1843-1845 (1998)

48. R. Azzam and N. Bashara, Ellipsometry and Polarized Light, (North-Holland, 1988)

49. Y. Shmaliy, Bandlimited signals in "Continuous-time signals," 1st edition (Springer 2010)

50. J. Blackledge and M. Turner, Other integral transforms in "Digital signal processing: mathematical and computational methods, software development and applications", (Horwood Publishing, 2001)

51. J. Poirson, T. Lanternier, J. Cotteverte, A. Le Floch, and F. Bretenaker, "Jones matrices of a quarter-wave plate for Gaussian beams," Applied Optics 34, 6806-6818 (1995)

52. T. Yoshino, M. Yokota and T. Kenmochi, "High-speed all-fibre polarisation controller," IEEE Electronics Letters 39, No. 25, (2003)

53. M. Yokota, Y. Sato, I. Yamaguchi, T. Kenmochi and T. Yoshino, "A compact polarimetric glucose sensor using a high-performance fibre-optic Faraday rotator," Measurement Science and Technology 15, 143-147, (2004)

54. Y. Ning, Z. Wang, A. Palmer and K. Grattan, "Recent progress in optical current sensing techniques," Review of Scientific Instruments 66, 3097-3111 (1995)

55. P. Jorge, P. Caldas, L. Ferreira, A. Ribeiro, J. Santos and F. Farahi, "Electrical current metering with a dual interferometric configuration and serrodyne signal processing," Measurement Science and Technology 13, 533–538 (2002)

56. M. Bock, R. Umathum, J. Sikora, S. Brenner, E. Aguor and W. Semmler, "A Faraday effect position sensor for interventional magnetic resonance imaging," Physics in Medicine and Biology 51, 999–1009, (2006)

57. E. Munin, V. Longo, A. Villaverde and M. Pacheco, "Analysis of the picosecond magneto-optical phenomena in scattering media of biological interest," Physics in Medicine and Biology 47, 1519–1534 (2002)

58. L. Ingersoll and D. Liebenberg, "Faraday Effect in Gases and Vapors. III," Journal of Optical Society of America 48, 339-343 (1958)

59. N. George, R. Waniek, and S. Lee, "Faraday Effect at Optical Frequencies in Strong Magnetic Fields," Applied Optics 4, 253-254 (1965)

60. K. Dismukes, S. Lott, Jr., and J. Barach, "Faraday Effect Measurements with Pulsed Magnetic Fields," Applied Optics 5, 1246-1247 (1966)

61. A. Villaverde, D. Donatti, D. Bozinis, "Terbium gallium garnet Verdet constant measurements with pulsed magnetic field," Journal of Physics C: Solid State Physics 11, L495-L498 (1978)

62. P. David, T. Milos, A. José Luis, L. V. Wang, "Evaluation of the magneto-optical effect in biological tissue models using optical coherence tomography", Journal of Biomedical Optics 12, 060502 (2007)

63. J. Davis, M. Islam and R. Lilly, "Time-dependent effects in Faraday rotation in pulsed magnetic fields: an explanation," Applied Optics 24, 1780-1783 (1985)

64. A. Yariv, “Optical Electronics in Modern Communications”, 5th edition, (Oxford University Press, 1997)

65. A. B. Villaverde, D. A. Donetti, “Verdet constant of liquids; measurements with a pulsed magnetic field”, Journal of Chemical Physics 71, 4021-4024 (1979)

66. I. Driver, J. W. Feather, P. R. King and J. B. Dawson, “The optical properties of aqueous suspensions of Intralipid, a fat emulsion,” Physics in Medicine and Biology 34, 1927-1930 (1989)

67. S. Flock, S. Jacques, B. Wilson, W. Star, and M. vanGemert, "The optical properties of Intralipid: a phantom medium for light propagation studies," Lasers in Surgery and Medicine 12, 510-9 (1992).

68. L. B. Cohen, "Changes in neuron structure during action potential propagation and synaptic transmission," Physiological Reviews 53, 373-418 (1973).

69. L. B. Cohen, R. D. Keynes and B. Hille, “Light Scattering and Birefringence Changes during Nerve Activity,” Nature 218, 438 - 441 (1968)

70. I. Tasaki, A. Watanabe, R. Sandlin, L. Carnay, “Changes in fluorescence, turbidity, and birefringence associated with nerve excitation,” Proceedings of the National Academy of Sciences US 61, 883-888 (1968).

71. L. Cohen, B. Hille, and R. D. Keynes, “Changes in axon birefringence during the action potential,” Journal of Physiology 211, 495–515 (1970)

72. A. Muralt, “The optical spike,” Philosophical Transactions of the Royal Society of London, B 270, 411-42 (1975)

73. K. Furusawa, “The depolarization of crustacean nerve by stimulation or oxygen want,” Journal of Physiology 67, 325-342, (1929)

74. A. Watanabe, “Change in optical activity of a lobster nerve associated with excitation,” Journal of Physiology 389, 223-253 (1987)

75. A. Van Harreveld, “A physiological solution for freshwater crustaceans,” Proceedings of the Society for Experimental Biology and Medicine 34, 428-432, (1936)

76. K. Carter, J. George, and D. Rector , “Simultaneous birefringence and scattered light measurements reveal anatomical features in isolated crustacean nerve,” Journal of Neuroscience Methods 135, 9–16 (2004)

77. K. Zheng, B. Liu, C. Huang, and M. E. Brezinski, "Experimental confirmation of potential swept source optical coherence tomography performance limitations," Applied Optics 47, 6151-6158 (2008)

78. J. Zhang, W. Jung, J. Nelson, and Z. Chen, "Full range polarization-sensitive Fourier domain optical coherence tomography," Optics Express 12, 6033-6039 (2004).

79. E. Götzinger, M. Pircher, and C. K. Hitzenberger, "High speed spectral domain polarization sensitive optical coherence tomography of the human retina," Optics Express 13, 10217-10229 (2005).

80. M. Yamanari, S. Makita, V. D. Madjarova, T. Yatagai, and Y. Yasuno, "Fiber-based polarization-sensitive Fourier domain optical coherence tomography using B-scan-oriented polarization modulation method," Optics Express 14, 6502-6515 (2006).

81. B. Baumann, E. Götzinger, M. Pircher, and C. K. Hitzenberger, "Single camera based spectral domain polarization sensitive optical coherence tomography," Optics Express 15, 1054-1063 (2007).

82. B. Cense, M. Mujat, T. C. Chen, B. H. Park, and J. F. de Boer, "Polarization-sensitive spectral-domain optical coherence tomography using a single line scan camera," Optics Express 15, 2421-2431 (2007).

83. W. Oh, S. Yun, B. Vakoc, M. Shishkov, A. Desjardins, B. Park, J. de Boer, G. Tearney, and B. Bouma, "High-speed polarization sensitive optical frequency domain imaging with frequency multiplexing," Optics Express 16, 1096-1103 (2008).

84. M. Yamanari, S. Makita, and Y. Yasuno, "Polarization-sensitive swept-source optical coherence tomography with continuous source polarization modulation," Optics Express 16, 5892-5906 (2008).

85. W. Oh, B. Vakoc, S. Yun, G. Tearney, and B. Bouma, "Single-detector polarization-sensitive optical frequency domain imaging using high-speed intra A-line polarization modulation," Optics Letters 33, 1330-1332 (2008)

86. H. Wang, M. K. Al-Qaisi, and T. Akkin, "Polarization-maintaining fiber based polarization-sensitive optical coherence tomography in spectral domain", Optics Letters 35, 154-156 (2010)

87. E. Götzinger, B. Baumann, M. Pircher, and C. K. Hitzenberger, "Polarization maintaining fiber based ultra-high resolution spectral domain polarization sensitive optical coherence tomography," Optics Express 17, 22704-22717 (2009)

88. S. H. Yun, G. Tearney, J. de Boer, and B. Bouma, "Pulsed-source and swept-source spectral-domain optical coherence tomography with reduced motion artifacts," Optics Express 12, 5614-5624 (2004)

89. A. Yurek, H. Taylor, L. Goldberg, J. Weller, A. Dandridge, "Quantum noise in superluminescent diodes," IEEE Journal of Quantum Electronics 22, 522-527 (1986)

90. M. Kobayashi, H. F. Taylor, K. Takada, and J. Noda, "Optical Fiber Component Characterization by High-Intensity and High-Spatial-Resolution Interferometric Optical-Time-Domain Reflectometer," IEEE Photonics Technology Letters 3, 564-566 (1991)

91. S. Yun, G. Tearney, J. de Boer, N. Iftimia and B. Bouma, "High-speed optical frequency-domain imaging," Optics Express 11, 2953-2963 (2003).

92. A. M. Rollins and J. A. Izatt, "Optimal interferometer designs for optical coherence tomography," Optics Letters 24, 1484-1486 (1999).

93. C. Dorrer, N. Belabas, J. P. Likforman, and M. Joffre, "Spectral resolution and sampling issues in Fourier-transform spectral interferometry," Journal of Optical Society of America B 17, 1795-1802 (2000)

94. E. Lee, J. de Boer, M. Mujat, H. Lim, and S. H. Yun, "In vivo optical frequency domain imaging of human retina and choroid," Optics Express 14, 4403-4411 (2006)

95. B. Cense, N. Nassif, T. Chen, M. Pierce, S. Yun, B. Park, B. Bouma, G. Tearney, and J. de Boer, "Ultrahigh-resolution high-speed retinal imaging using spectral-domain optical coherence tomography," Optics Express 12, 2435-2447 (2004)

96. S. H. Yun, C. Boudoux, G. J. Tearney, and B. E. Bouma, "High-speed wavelength-swept semiconductor laser with a polygon-scanner-based wavelength filter," Optics Letters 28, 1981-1983 (2003).

97. H. Lim, J. de Boer, B. Park, E. Lee, R. Yelin, and S. Yun, "Optical frequency domain imaging with a rapidly swept laser in the 815-870 nm range," Optics Express 14(13), 5937–5944 (2006)

98. Y. Yasuno, V. Madjarova, S. Makita, M. Akiba, A. Morosawa, C. Chong, T. Sakai, K. Chan, M. Itoh, and T. Yatagai, "Three-dimensional and high-speed swept-source optical coherence tomography for in vivo investigation of human anterior eye segments," Optics Express 13, 10652-10664 (2005)

99. C. Fan and G. Yao "Correcting Optical-Axis Calculation in Polarization-Sensitive Optical Coherence Tomography," IEEE Transactions on Biomedical Engineering 57 (10), 2556 - (2010)

100. J. Canny, "A computational approach to edge detection," IEEE Transactions on Pattern Analysis and Machine Intelligence 8(6), 679–698 (1986).

101. H. Nema, V. Singh, and N. Nema, "Anatomy of the Uveal Tract" in Textbook of Ophthalmology, S. Agarwal, A. Agarwal, D. Apple, L. Buratto, 1st edition, (Lippincott Williams & Wilkins, 2002) pp 1982

102. L. Mandell and E. Wolf, Optical Coherence and Quantum Optics, 1st edition (Cambridge University Press, 1995)

103. M. Born and E. Wolf, Interference and Diffraction with Partially Coherent Light in "Principles of Optics", 5th edition (Pergamo, 1975) pp 491-518

104. G. Fowles, "Coherence and Interference" in Introduction to Modern Optics, 2nd edition (Dover Publications, 1989)

105. L. Mandel, E. Wolf, Second-Order Coherence Theory of Scalar Wavefields in "Optical Coherence and Quantum Optics", 1st edition (Cambridge University Press, 1995) pp147-179

106. M. Born, E. Wolf, A. Bhatia, P. Clemmow, D. Gabor, A. Stokes, A. Taylor, P. Wayman, W. Wilcock, Principles of Optics: Electromagnetic Theory of Propagation, Interference and Diffraction of Light, 7th edition (Cambridge University Press, 2000)

107. E. Hecht, Basics of Coherence Theory in "Optics", 4th edition, (Addison Wesley, 2001)

108. L. Mandell and E.Wolf, "Coherence Properties of Optical Fields," Reviews of Modern Physics 37(2), 231-287 (1965)

109. J. Perina, Coherence of Light, 1st edition (Springer, 1985)

110. P. Hariharan, "Optical Interferometry" 2nd edition (Academic Press, 2003)

111. J. Goodman, Statistical Optics, 1st edition, (Wiley-Interscience, 2000)

112. Y. Pan, R. Birngruber, J. Rosperich, and R. Engelhardt, "Low-coherence optical tomography in turbid tissue: theoretical analysis," Applied Optics 34, 6564-6574 (1995)

113. J. Schmitt, "Optical coherence tomography (OCT): A review," IEEE Journal of Selected Topics in Quantum Electronics 5(4), 1205–1215 (1999)

114. J. Izatt, M. Kulkarni, H. Wang, K. Kobayashi, and M. Sivak, Jr., "Optical coherence tomography and microscopy in gastrointestinal tissues," IEEE Journal of Selected Topics in Quantum Electronics 2, 1017-1028 (1996).

115. J. Goodman, “Fresnel and Fraunhofer Diffraction” in Introduction to Fourier Optics, 3rd edition, (Roberts & Company Publishers, 2004), pp 63-65

116. W. Koechner, “Introduction” in Solid State Lasers, 5th revised and updated edition, (Springer, 1999) p8-12

117. A. Siegman, Linear Pulse Propagation in “Lasers”, (University Science Books, 1986) pp 331-335

118. W. Drexler, J. Fujimoto, OCT Applications in Developmental Biology in “Optical Coherence Tomography: Technology and Applications”, 1st edition. A. Davis, S. Boppart, F. Rothenberg, and J. Izatt. 1st edition (Springer, April 2008) pp 923

119. S. Yun, G. Tearney, J. de Boer, and B. Bouma, "Removing the depth-degeneracy in optical frequency domain imaging with frequency shifting," Optics Express 12, 4822-4828 (2004)

120. J. Zhang, J. Stuart Nelson, and Z. Chen, "Removal of a mirror image and enhancement of the signal-to-noise ratio in Fourier-domain optical coherence tomography using an electro-optic phase modulator," Optics Letters 30, 147-149 (2005)

121. B. Vakoc, S. Yun, G. Tearney, and B. Bouma, "Elimination of depth degeneracy in optical frequency-domain imaging through polarization-based optical demodulation," Optics Letters 31, 362-364 (2006)

122. B. Baumann, M. Pircher, E. Götzinger, and C. Hitzenberger, "Full range complex spectral domain optical coherence tomography without additional phase shifters," Optics Express 15, 13375-13387 (2007)

123. K. Lee, P. Meemon, W. Dallas, K. Hsu, and J. Rolland, "Dual detection full range frequency domain optical coherence tomography," Optics Letters 35, 1058-1060 (2010)

Appendix A
THE OCT EQUATION

The OCT characteristic equation is mentioned in a countless number of references, but we are not aware of any that presents the derivation of the equation with details. In this appendix, the OCT equation is derived in details to help understanding the equations used in the rest of this manuscript.

OCT measures the temporal coherence of light. Because the mathematical analyses of spatial and temporal interferometry are sometimes similar, and to maintain a comprehensive description of the derivation of the OCT equation, the references describing spatial coherence are recalled as needed [44, 102-110]. In most instances, the derivation in this appendix follows the temporal interferometry derivation in [111 (pp 158-170)]. Brief derivation of the OCT equation is described in [112-114].

A.1. LOW COHERENCE INTERFEROMETRY

Let us consider a light source with a central frequency v_o, and bandwidth Δv, illuminating a Michelson interferometer (the interferometer is shown in Figure 2.3). For a quasi-monochromatic (low-coherence) source, $\Delta v / v\mathrm{o} \ll 1$; and the electric field of the source can be written as $E_{in}(t) = |E_{in}|\exp(j2\pi v_o t)$ [102]. The intensity split factors of the beam splitter are k_r and k_s for light transmitted into the reference and sample arms, respectively. In a lossless beam

splitting, $k_r + k_s = 1$. The electric field illuminating the reference and sample can be therefore written as $\sqrt{k_s}E_{in}(t)$ and $\sqrt{k_r}E_{in}(t)$, respectively.

If R is the reflectivity of the sample, light reflected from the sample can be written as $\sqrt{R}\sqrt{k_s}E_{in}(t)$, and the portion of electric field coupled in the detection arm from the sample arm is written as

$$E_s(t) = \sqrt{R}\sqrt{k}E_{in}(t) \quad \textbf{A.1}$$

where

$$k = k_r k_s \quad \textbf{A.2}$$

Similarly, the portion $E_r(t) = \sqrt{A}\sqrt{k}E_{in}(t)$is transmitted from the reference arm into the detection arm, where A is the reference mirror attenuation. For an arbitrary increase in the length of the reference arm $d/2$, a double pass phase delay of $(2\pi/\lambda_0)d$ is encountered by the reference light, where λ_o is the central wavelength of the light source. Define τ as the time delay resulting from light travelling d[23]. Light coupled from the reference arm into the detection arm can therefore be rewritten as

$$E_r(t-\tau) = \sqrt{A}\sqrt{k}E_{in}(t-\tau) \quad \textbf{A.3}$$

In case the polarizations of the electric fields reflected from the sample and reference arms are the same, the electric fields at the output of the interferometer, $E_o(t)$, can be written as the sum of $E_s(t)$ and $E_r(t - \tau)$

[23] The consequent phase delay can be rewritten as $2\pi v_o \tau$. Recall that $d = c/\tau$ and $\lambda_o = c/v_o$.

$$E_o(t) = E_r(t-\tau) + E_s(t) \qquad \textbf{A.4}$$

Light vibrations are faster than the response of electronic detectors, and the electric field of a light wave cannot be recorded as a function time [102 (p 161)]; the detector therefore records the time average of the signal. This means that each measurement is actually an average of a number optical wave cycles. The intensity of light detected using the photodetector is $I_d^{'} = \eta\langle|E_o(t)|^2\rangle = \rho\langle E_o(t)E_o^*(t)\rangle$, where η is the responsivity of the detector [115], and the brackets $\langle\ \ \rangle$ indicate time averaging. Because η is a scalar that is not significant in the following analysis, we define $I_d = I_d^{'}/\eta$ and write

$$I_d = \langle E_o(t)E_o^*(t)\rangle = \langle[E_r(t-\tau) + E_s(t)][E_r^*(t-\tau) + E_s^*(t)]\rangle \qquad \textbf{A.5}$$

Solving Equation A.5 yields

$$\begin{aligned} I_d = {} & \langle\left[\sqrt{k_s}\sqrt{k_r}\sqrt{A}E_{in}(t-\tau) + \sqrt{k_s}\sqrt{k_r}\sqrt{R}E_{in}(t)\right] \\ & .\left[\sqrt{k_s}\sqrt{k_r}\sqrt{A}E_{in}(t-\tau) + \sqrt{k_s}\sqrt{k_r}\sqrt{R}E_{in}(t)\right]^*\rangle \\ I_d = {} & \sqrt{k_r k_r^*}\sqrt{k_s k_s^*}\sqrt{AA^*}\langle E_{in}(t)E_{in}^*(t)\rangle + \sqrt{k_s k_s^*}\sqrt{k_r k_r^*}\sqrt{RR^*}\langle E_{in}(t-\tau)E_{in}^*(t-\tau)\rangle \\ & + \sqrt{k_r k_r^*}\sqrt{k_s k_s^*}\sqrt{AR^*}\langle E_{in}(t-\tau)E_{in}^*(t)\rangle + \sqrt{k_s k_s^*}\sqrt{k_r k_r^*}\sqrt{A^*R}\langle E_{in}(t)E_{in}^*(t-\tau)\rangle \end{aligned} \qquad \textbf{A.6}$$

Neglecting the constant phase delay in the beam splitter, the constants k_s and k_r are real-valued, and $k_s^* = k_s$ and $k_r^* = k_r$. The phase difference between the sample and reference arms is considered in the time delay τ; A and R are therefore real-valued, too. Equation A.6 can be rewritten as

$$\begin{aligned} I_d = {} & kA\langle|E_{in}(t)|^2\rangle + kR\langle|E_{in}(t-\tau)|^2\rangle \\ & + k\sqrt{AR}\langle E_{in}(t-\tau)E_{in}^*(t)\rangle + k\sqrt{AR}\langle E_{in}(t)E_{in}^*(t-\tau)\rangle \end{aligned} \qquad \textbf{A.7}$$

The last two terms of equation A.7 are in fact a summation of a complex value and its conjugate, this equals the real value of either of the values multiplied by two:

$$I_d = kA\langle|E_{in}(t)|^2\rangle + kR\langle|E_{in}(t-\tau)|^2\rangle + 2k\sqrt{AR}\,\mathcal{R}e\{\langle E_{in}(t)E_{in}^*(t-\tau)\rangle\} \quad \textbf{A.8}$$

The first two terms in Equation A.8 are DC components that are equal to light intensity coupled from sample and reference arms into the detection arm, respectively. The third term carries the autocorrelation information. The time-averaged cross-correlation function in the third term is known as the self coherence function, $\Gamma(\tau)$,

$$\Gamma(\tau) = \langle E_{in}(t)E_{in}^*(t-\tau)\rangle \quad \textbf{A.9}$$

The time averages of the first two terms in Equation A.8 can similarly be written as

$$\langle E_{in}(t)E_{in}^*(t)\rangle = \langle|E_{in}(t)|^2\rangle = \Gamma(0) \quad \textbf{A.10}$$

$$\langle E_{in}(t-\tau)E_{in}^*(t-\tau)\rangle = \langle|E_{in}(t-\tau)|^2\rangle = \Gamma(0) \quad \textbf{A.11}$$

And Equation A.8 can be rewritten as

$$I_d = kA\Gamma(0) + kR\Gamma(0) + 2k\sqrt{A}\sqrt{R}\,\mathcal{R}e\{\Gamma(\tau)\} \quad \textbf{A.12}$$

If we define I_{DC} as the DC light intensity coupled from the reference and sample arms assuming unity reflectivity and attenuation, the following expression can be written

$$I_{DC} = k\Gamma(0) \quad \textbf{A.13}$$

And we can write

$$k = \frac{I_{DC}}{\Gamma(0)} \tag{A.14}$$

And rewrite Equation A.12 as

$$\begin{aligned} I_d &= AI_{DC} + RI_{DC} + 2\frac{I_{DC}}{\Gamma(0)}\sqrt{A}\sqrt{R}\,\mathcal{R}e\{\Gamma_{rs}(\tau)\} \\ &= AI_{DC} + RI_{DC} + 2I_{DC}\sqrt{A}\sqrt{R}\,\mathcal{R}e\left\{\frac{\Gamma(\tau)}{\Gamma(0)}\right\} \end{aligned} \tag{A.15}$$

A normalized version of mutual coherence function has resulted in the third term in Equation A.15. This quantity is known as complex degree of coherence of the light

$$\gamma(\tau) = \frac{\Gamma(\tau)}{\Gamma(0)} \tag{A.16}$$

If we write $I_s = RI_{DC}$ and $I_r = AI_{DC}$, the intensity of the time-averaged electrical field detected using the photodetector can be written as

$$I_d = I_r + I_s + 2I_{DC}\sqrt{A}\sqrt{R}\,\mathcal{R}e\{\gamma(\tau)\} \tag{A.17}$$

And for a DC-filtered reading, the interference term I_i is expressed as

$$I_i = 2I_{DC}\sqrt{A}\sqrt{R}\,\mathcal{R}e\{\gamma(\tau)\} \tag{A.18}$$

Now let's write the complex degree of coherence as a magnitude and phase term

$$\gamma(\tau) = |\gamma(\tau)|e^{-i\Psi(\tau)} \tag{A.19}$$

and rewrite Equation A.18 as

$$I_i = 2\, I_{DC}\sqrt{A}\sqrt{R}\,|\gamma(\tau)|\cos[\Psi(\tau)] \qquad \textbf{A.20}$$

Equation A.20 shows that the AC signal on the detector is a cosinusoidal wave weighted by the reflectivity of the sample, and the τ-dependent complex degree of coherence of the light. In the next section we will show how, for a Gaussian illumination, this interference pattern enables us to resolve the signal reflected from different depths in the sample, and record information about the phase delay in the sample arm.

A.2. Optical Coherence Tomography

The basic OCT setup is similar to the LCI shown in Figure 2.3. In the sample arm, however, there is usually a lens to focus the light on the tissue, and 2-dimenstional scanning mechanism to interrogate different points in the sample. In time-domain OCT, the reference arm is equipped with a scanning mechanism to change the time delay τ.

We have mentioned in the previous subsection that the photodetector measures the time average of the light wave, and that each measurement is an average of a number of optical wave cycles. The intensity measurement launched by the photodetector is thus independent from time origin. This type of processes is known as wide-sense stationary process [111 (pp 63-68)]. Weiner-Khintchen theorem states that for a stationary process, the power spectral density function is a Fourier conjugate of the autocorrelation of that function [111 (pp 73-79)]. Therefore,

$$\Gamma(\tau) = \mathcal{F}\{S(\nu)\} \qquad \textbf{A.21}$$

where $S(\nu)$ is the power spectral density of the source, and $\mathcal{F}$ is Fourier transform. Using Equations A.16 and A.21 we can write [111 (p 164)]

$$\gamma(\tau) = \frac{\mathcal{F}\{S(\nu)\}}{\mathcal{F}\{S(\nu)\}|_{\tau=0}} = \mathcal{F}\{\hat{S}(\nu)\} \qquad \textbf{A.22}$$

where $\hat{S}(\nu) = S(\nu)/\int_0^\infty S(\nu)d\nu$ is the power spectral density normalized to its area. $\hat{S}(\nu)$ is calculated here from a single-sided real value of the complex power spectral density [44 (pp 104-108), 102 (pp 494-499, 504, and 506)]. By definition, $\hat{S}(\nu)$ has a unit area.

The expression for normalized Gaussian power spectral density calculated for solid-state lasers is [116]

$$\hat{S}(\nu) = \frac{2\sqrt{\ln 2}}{\sqrt{\pi}\Delta\nu}\exp\left[-\left(2\sqrt{\ln 2}\frac{\nu-\nu_o}{\Delta\nu}\right)^2\right] \qquad \textbf{A.23}$$

where $\Delta\nu$ is a full-width at half-maximum (FWHM) power bandwidth. The complex degree of coherence can now be written as

$$\gamma(\tau) = \exp\left[-\left(\frac{\pi\Delta\nu\tau}{2\sqrt{\ln 2}}\right)^2\right]\exp(-i2\pi\nu_o\tau) \qquad \textbf{A.24}$$

and therefore

$$|\gamma(\tau)| = \exp\left[-\left(\frac{\pi\Delta\nu\tau}{2\sqrt{\ln 2}}\right)^2\right] \qquad \textbf{A.25}$$

$$\Psi(\tau) = 2\pi\nu_o\tau \qquad \textbf{A.26}$$

For a low-coherent Gaussian illumination of Michelson interferometer, Equation A.20 can be rewritten as

$$I_i(\tau) = 2\,I_{DC}\sqrt{A}\sqrt{R}\exp[-(\alpha\tau)^2]\cos[2\pi\nu_o\tau] \qquad \textbf{A.27}$$

where $\alpha = \pi\Delta\nu/2\sqrt{\ln 2}$. This means that, light reflected from a single reflector in the sample arm creates an interference pattern with a Gaussian envelope modulated by a cosinusoidal modulation at frequency ν_o. This pattern is known as the coherence function. If the time delay in the reference arm, τ, is increased by an amount larger than the width of $\gamma(\tau)$, the interference pattern diminishes. In other words, the interference pattern is only detected when the lengths of the sample and reference arms are almost the same, i.e. τ (or equivalently d) ≈ 0. This enables the localization of a reflector in the sample arm on the axial dimension, d, along the propagation axis of the sample beam.

Appendix B
GENERAL OCT DESIGN CONSIDERATIONS

B.1. AXIAL RESOLUTION

Equation A.27 shows that, with a single reflection from the sample arm, the cosinusoidal interference pattern has a Gaussian envelope, and that the width of the envelope is inversely proportional to the bandwidth of the source, Δv. The origin of the Gaussian envelope under low-coherence illumination can be understood by looking at the superposition of the spectral components of the source. In other words, the product of the Gaussian and cosinusoidal term in Equation A.27 is equivalent to the summation of the cosinusoids of the spectral components of the source. Because of dephasing, the summation of these terms starts to diminish as we go farther from the origin $\tau = 0$. In agreement with Heisenberg uncertainty principle, narrower Gaussian term is observed at broader Δv. If Δv approaches zero, i.e. light is monochromatic, the function $|\gamma(\tau)| = 1$, and the cosinusoidal fringe extends across the entire range of τ.

To understand this concept, Figure B.1 shows the spectral components of three light sources and the corresponding $S(\nu)$ and $\gamma(\tau)$ functions. The first case in (a) shows a monochromatic source yielding a unity $|\gamma(\tau)|$ envelope (the envelope is shown in green). Case (b) shows that as the bandwidth of the source increases, the components of the interference pattern dephases as τ departs from zero, and the magnitude of the complex degree of coherence function $|\gamma(\tau)|$ decays accordingly. For broader bandwidths, i.e. lower temporal coherence, $|\gamma(\tau)|$ decays faster as shown

in Figure B.1 (c). For simplicity, $S(\nu)$ is represented as a rectangular function in this example; according to Equation A.22, $|\gamma(\tau)|$ is actually a sinc function. The right column in Figure B.1 (b) and (c) shows only part of the main lobe of the sinc.

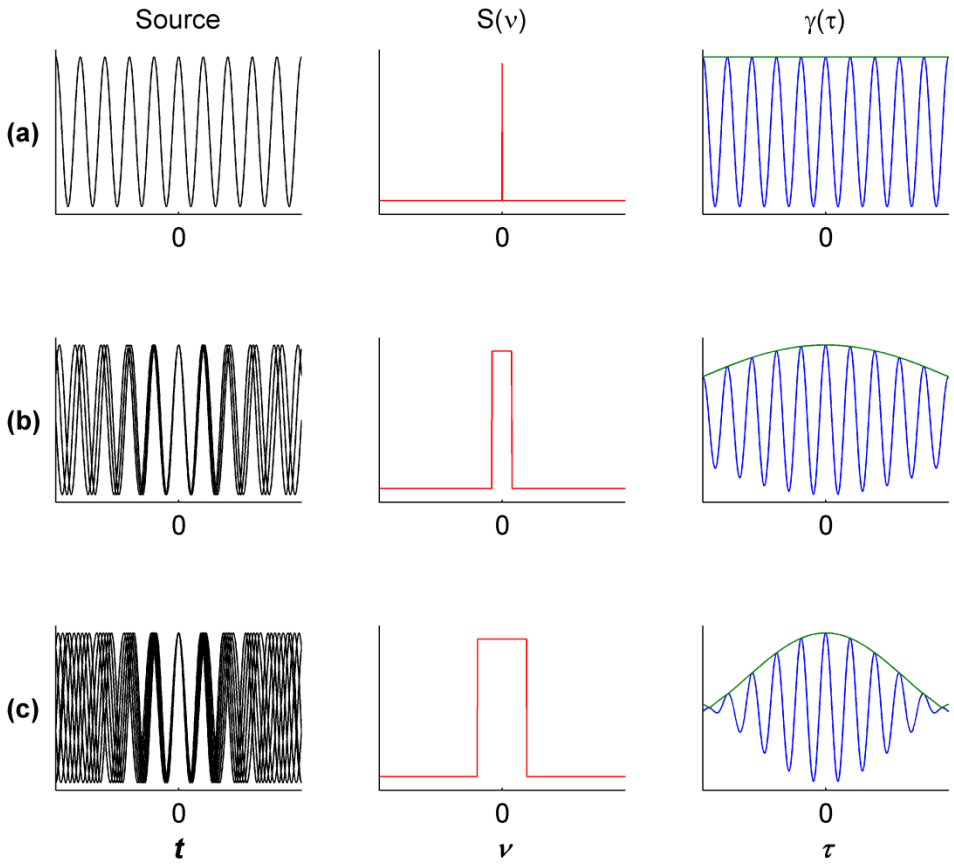

Figure B.1 The left column shows the spectral content of three light sources. (a) is monochromatic, while (b) and (c) exhibit respectively lower degrees of coherence. The second column shows that broader spectral density functions correspond to less-coherent sources. The third column shows that complex degree of coherence function. The green envelope, $|\gamma(\tau)|$, shows that the width of the coherence function is inversely proportional to the bandwidth of the source.

The time it takes a coherent wave to lose its coherence, i.e. $|\gamma(\tau)| \rightarrow 0$, is known as the coherence time τ_c; the corresponding coherence length d_c is equal to $c\tau_c$. Different definitions of the coherence length have been adopted in different applications. In OCT, the value of the

coherent time is taken at the time-bandwidth product, $\Delta\tau\Delta\nu$, at FWHM intensity. For a Gaussian source, the minimum $\Delta\tau\Delta\nu$ is equal to $2\ln 2/\pi = 0.44$ [116]. Because $\lambda/\Delta\lambda = \nu/\Delta\nu$, and $\nu = c/\lambda$, the coherence length can be written as $0.44(\lambda_o^2/\Delta\lambda)$. The axial resolution, ρ_a, is defined as the FWHM coherence length in a medium with refractive index n. OCT axial resolution is expressed as [114]

$$\rho_a = \frac{0.44}{n}\frac{\lambda_o^2}{\Delta\lambda} \qquad \textbf{B.1}$$

where $\Delta\lambda$ is the FWHM bandwidth of the source. Thus, higher OCT axial resolution is achieved at broader bandwidth of the source.

B.2. Dispersion Mismatch and Dispersion Compensation

Equation B.1 was calculated for a transform-limited coherence function that is equivalent to a Gaussian envelope modulated by a pure cosine. Practically, the coherence function recorded at the output of the interferometer might be altered yielding a chirp modulation. In this case, the constant in Equation B.1 is larger than 0.44 resulting in degraded axial resolution [116]. In case of dispersion mismatch between the sample and reference arms of OCT interferometers, chirped coherence function and degraded axial resolution are observed.

In the derivation of Equation A.27, the only phase delay considered was the one due to τ. Because broadband sources are desired in OCT, the wavelength-dependent dispersion in the optical media cannot be neglected. Due to dispersion, different frequencies of the propagating light experience different refractive indexes, $n(\nu)$; the time delay is thus a function of frequency, $\tau(\nu)$. As a result, the phasor of the electric field coupled from the reference arm, for example, in the detection arm is accurately written as $\exp[2\pi\nu(\tau)t]$. This means that $\Gamma(\tau)$ in Equation A.9 has the phasor $exp[2\pi(\nu(\tau) - \nu_o)t]$ yielding a cosine function with a τ-dependant frequency in Equation

A.27. Therefore, due to dispersion mismatch, the interference pattern is actually chirped, and the axial resolution of the OCT system can be considerably degraded.

If the sample and reference arms had similar dispersion, the τ-dependent phasors from the two arms are equal. Therefore, they cancel out in the autocorrelation function leaving the self-coherence function in Equation A.9 and the rest of the derivation unchanged. So, a simple and common dispersion compensation method can be accomplished by making the propagation media in the sample and reference arms the same. In cases like retinal imaging, for example, the dispersion in the sample arm due to propagating in the vitreous humor, which is 98-99% water, can be simply compensated by placing a cuvette of water in the reference arm to match the propagation path in the sample arm.

B.3. Lateral Resolution and Depth of Range

The lateral resolution of the OCT system is dictated by the optics of the sample arm. Two cases need to be considered to calculate the sport size at the focus of the sample objective. Lets define f_{obj} as the focal length of the objective lens in the sample arm, and d_{b} is the diameter of the collimated laser beam on the objective. Let us now consider diffraction-limited optics. A collimated beam illuminating a lens has an airy disk distribution at the focal point. If resolution is defined as the width of the main lobe at its first null, the expression $\rho_l^{diff} = 4/\pi \left(\lambda_o f_{obj} / d_b\right)$ can be derived. In the second case we consider that light does not propagate perfectly collimated but as a Gaussian beam [64 (pp 56)]. If waist of the Gaussian beam occurs at the lens surface, $\rho_l^{gauss} = 1/\pi \left(\lambda_o f_{obj} / d_b^2\right)$.

Lateral resolution is dictated by the larger of the two cases. A simple calculation shows that ρ_l^{diff} is larger than ρ_l^{gauss} as long as d_{b} is larger than a quarter millimeter. Given typical parameters of an OCT system where $\lambda_o \approx 1$ μm and $d_{\text{b}} \approx 30$ mm, the condition $d_{\text{b}} < 0.25$ mm yields

a poor lateral resolution of more than 150 μm. Therefore the diffraction-limited resolution is used to express the lateral resolution

$$\rho_l = 1.22\frac{\lambda_o f_{obj}}{d_{\mathrm{b}}} \qquad \textbf{B.2}$$

Which is the same to the expression in [118].

It is still important, however, to consider the Gaussian propagation of the beam to calculate the Rayleigh range, or equivalently the depth-of-focus (DOF). Most of light energy is lost after a single DOF around the focal place along the axial direction. The DOF is expressed as [114]

$$\mathrm{DOF} = \frac{\pi\rho_l^2}{2\lambda_o} \qquad \textbf{B.3}$$

It is desired to design the system to yield to the best possible lateral resolution. However, because the DOF is quadratically proportional to the lateral resolution, the axial imaging range poses a limitation on ρ_l. In order to achieve the best possible depth-resolved imaging, DOF should be larger than, or at least comparable to, the axial imaging range. For example, if the same abovementioned case is considered, ρ_l < 40 μm yields a tight DOF and axial imaging range below 3 mm in air.

B.4. HIGHER-DIMENSIONAL IMAGING

Imaging of a single depth line, known as an A-line, was introduced in the previous subsections. Higher-dimensional imaging using OCT is possible by scanning the sample beam across the desired line or area. Raster scanning can be accomplished by moving the sample itself, or, alternatively, scanning the laser beam. Fast scanning of the laser beam using galvanometer-

mounted mirrors is the most common technique because of the speed advantage, and the convenience it introduces for *in situ* imaging. Figure B.2 shows the sample laser beam raster-scanned on the sample by means of a galvanometer-scanned mirror. Two-dimensional (2D) imaging is accomplished using this setup. The figure also shows the lateral resolution and an appropriate example of the DOF.

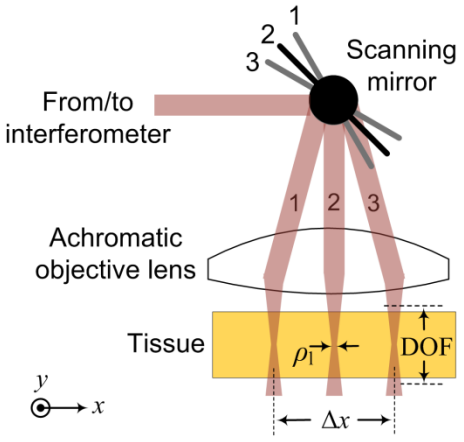

Figure B.2 Common setup for the sample arm of an OCT with the ρ_l and DOF annotated. The mirror positions 1, 2, and 3 and the corresponding laser beams are shown.

The number of A-lines acquired for each 2D frame (B-line) is called the B-line length, N_B. To guarantee that lateral resolution is not compromised, the B-line length should be at least equal to laterally scanned distance Δx divided by ρ_l.

$$N_B = \frac{\Delta x}{\rho_l} \qquad \textbf{B.4}$$

For 3D imaging, another scanning mirror is added to scan across the y dimension. The frame across the y dimension is called the C-line, and the number of B-lines in each C-line is known as the C-line length, N_C.

$$N_C = \frac{\Delta y}{\rho_l} \qquad \textbf{B.5}$$

It is shown in Figure B.2 that an achormatic lens is used as the sample objective. OCT systems are illuminated with Achromatic light sources to improve the axial resolution (see Equation B.1). Therefore, in contrast to monochromatic imaging technique, the chromatic aberration is the major concern, especially in high-resolution OCT. It is therefore common to use achromatic lenses in an OCT setup.

Appendix C
TIME DOMAIN OCT

Depth-resolved mapping in TD OCT is realized by changing the time delay, τ. This can be accomplished by a linearly-scanned mirror in the reference arm. The characteristic frequency of the cosine term in Equation A.27 is equal to the central frequency of the light source, which is faster than any available electronic detector. This means that the modulating frequency of the envelope $|\gamma(\tau)|$ cannot be directly detected. Also, it is important to remember that the interference pattern I_i is measured by filtering the DC component in the intensity I_d recorded by the photodetector (see Equations A.17 and A.18). Therefore, it is not practical to attempt to directly record the coherence function, which exhibit a very low frequency that may interfere with the DC filter. Therefore, the optical signal needs to be modulated in TD interferometry.

C.1. FRINGE MODULATION

Due to the movement of the reference mirror, the reference beam is Doppler-shifted by frequency $f = 2v/\lambda$ [3], were v is the velocity of the reference mirror. In this case, the coherence function, $|\gamma(\tau)|$, is modulated at f. I_i is practically measured by applying a band-pass filter centered at f. To create more accurate modulation a more precise modulation scheme, typically an Electro-Optics Modulator (EOM), is typically employed (As in CHAPTER 3). EOMs are stable devices that are usually placed in the reference arm of the TD interferometer, and driven by an electrical signal. The precise and stable modulation using EMO enables accurate phase-sensitive

measurements with sub-wavelength accuracy (As in CHAPTER 4 and CHAPTER 5). In practice, I_i is actually measured by band-pass filtering I_d around f.

C.2. SAMPLING FREQUENCY

Sampling frequency in TDOCT is tied to the modulation frequency and the demodulating scheme. Hilbert transform is commonly applied to the digitized data to calculate the envelope of the A-line and the phase of the modulation fringe. The digitizer sampling frequency limit emanates from the numerical precision of the Hilbert transform. We have noticed that five points per fringe (full cosinusoid) are sufficient to describe each fringe for intensity imaging purposes. However, we always chose to use ten to fifty points for phase measurements.

Appendix D
FOURIER DOMAIN OCT

To understand the FD OCT approach, let us represent the coherence function of the single reflector in the sample arm by a Dirac function. Figure D.1 depicts the coherence function at different sample depths in the top row, and the spectrum of each coherence function calculated using Fourier transform in the bottom row. The spectrum of the Dirac is a cosine function with a frequency proportional to the displacement between the Dirac and the origin. This means that higher frequencies of the spectral fringe correspond to deeper reflectors in the sample, see Figure D.1 (a), (b) and (c). Figure D.1 (d) shows the interference pattern due to the three reflectors in (a), (b), and (c) together. The corresponding spectrum is in fact a superposition of the three cosines in (a), (b), and (c). The concept of FD OCT is based on recording the spectral fringe pattern (the top row in Figure D.1), and calculating the interference pattern (the bottom row). It is important to stress that the modulation fringes detected in FD OCT are different than those in TD OCT.

One can note that, because the coherence functions in Figure D.1 are dirac functions, $\Delta\nu$ is infinite. This agrees with axial resolution expression in Equation B.1. A finite axial resolution is equivalent to convolving the coherence functions in the top row of Figure D.1 with a Gaussian shape expressed by the FWHM coherence function ρ_a, see in Figure D.2. It is known that convolution in one domain is equivalent to multiplication in its Fourier pair domain. A Gaussian

coherence function is therefore equivalent to multiplying the spectra in the right column of Figure D.1 by the Fourier transform of the Gaussian shape convolved with the coherence functions.

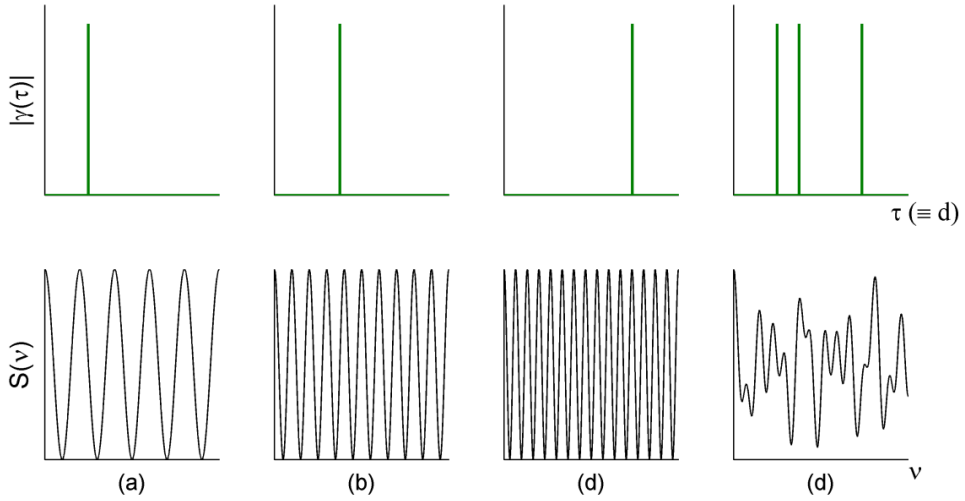

Figure D.1 The concept of FDOCT. The coherence function measured at different sample depths (top), and the corresponding spectral distributions (bottom). (a) (b) and (c) show that as the sample move backwards, the frequency of the corresponding spectra increases. When more than one reflector is placed in the sample arm, (d), the power spectral distribution is a superposition of the spectrum of each reflector.

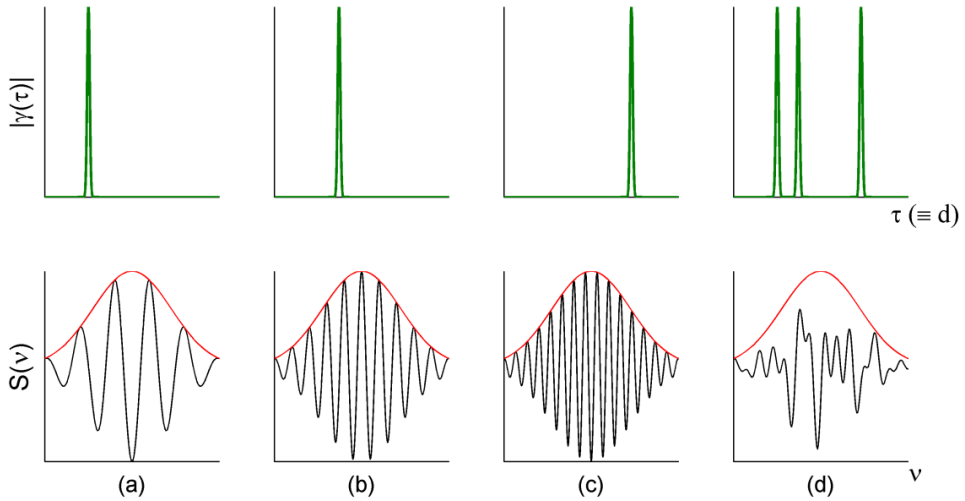

Figure D.2 When the interference pattern (top) is convolved with a Gaussian coherence function, the spectral fringes (bottom) are multiplied by the Fourier transform of the coherence function centered at origin.

D.1. Quantization Effect – Depth Degeneracy

The power spectral density function $\hat{S}(\nu)$, recorded in FD OCT is quantized, and the spectrum is recorded over discrete ν intervals, $\delta\nu$. This is a normal consequence of the limited resolution of the Spectral Domain OCT detector, and the finite instantaneous width of the Swept Source OCT source. Consequently, the intensity of the interference pattern I_i decays proportional to τ. Figure D.3 (a) shows the spectral fringe pattern; the two dotted lines in the bottom depict two detection schemes with two different intervals, $\delta\nu$. The detector in blue has a higher resolution. In both cases, the Fourier transform of the detector function yields an envelope multiplied by the A-line. The envelope is maximal at $\tau = 0$; signal degeneracy is observed at larger depths in the sample. Figure D.3 (b) shows the decay envelopes that correspond to the two detection schemes. The width of these envelopes is inversely proportional to $\delta\nu$, and the decay is slower when higher-resolution detection schemes are adapted.

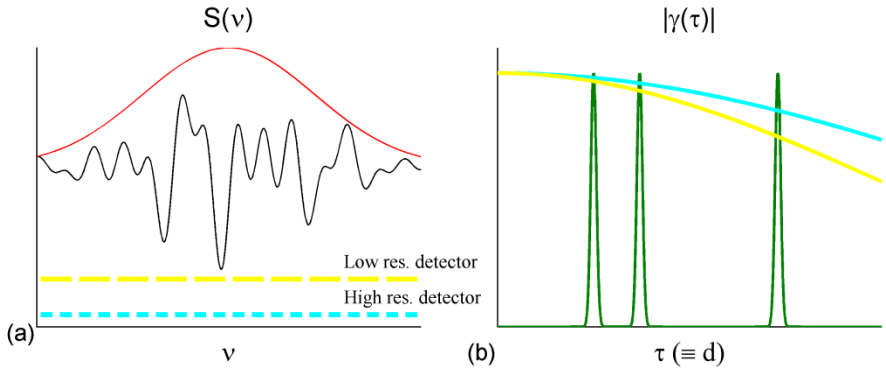

Figure D.3 Signal degeneracy in FDOCT. (a) The spectral interference is measured with discrete intervals $\delta\nu$. The detection scheme depicted in blue has a higher resolution than that in yellow. (b) shows the A-line in case of TD systems, overlaid with the decay envelopes corresponding to the detection schemes in (a). Higher resolution in FD OCT detection reduces the severity of the quantization effect.

Sampling as described here is performed in the analog domain, it does not affect the number of samples per A-line. However, digital sampling determines the number of points per A-line, and therefore the maximum imaging range.

D.2. DIGITIZATION EFFECT – IMAGING RANGE

The spectral interference pattern is digitized for data processing and the A-line is calculated using the Discrete Fourier Transform (DFT). Because the frequency of the spectral interference is proportional to the depth in the sample, the maximum depth, known as the imaging range, is limited by Nyquist sampling theorem. The imaging range can expressed as [6, 11, 91]

$$d_{max} = \frac{1}{4n}\frac{\lambda_o^2}{\delta\lambda} \qquad \textbf{D.1}$$

where $\delta\lambda$ is the bandwidth of each measurement of the spectrum. Given the A-line length N_A, $\delta\lambda$ is written as

$$\delta\lambda = \frac{\Delta\lambda}{N_A} \qquad \textbf{D.2}$$

D.3. MIRROR IMAGE

Optical detectors can only record real values; the Fourier transform of the spectral interference pattern is therefore symmetric. This means that $|\gamma(\tau)| = |\gamma(-\tau)|$, and that mirror images of the sample are calculated using FD OCT. The modulation frequency of the spectral fringe is zero when $\tau = 0$. At this point, FD OCT systems do not distinguish between positive and negative shifts in τ, and the part of the image where τ is negative is inverted and overlaid on the positive τ image. Mirror images are avoided by shifting the sample surface away from $d = 0$, or employing one of the full-range imaging techniques [119-123].